3-5 November 2025 • Royal Orchid Sheraton Riverside Hotel Bangkok
Bangkok, Thailand

NANO
THAILAND 2025

NanoThailand 2025

"Revolutionizing the Future"

The 9th Thailand International Nanotechnology Conference

e-Proceedings

V 1.2

e-Proceeding

The 9th Thailand International Nanotechnology Conference
NANOTHAILAND 2025 (Volume 2)

"Revolutionizing the Future"
November 3-5, 2025
Royal Orchid Sheraton Riverside Hotel Bangkok Bangkok, Thailand

Published by:
Nanotechnology Association of Thailand

Available online at: https://nano-thailand.com/2025/

NANO THAILAND 2025

TABLE OF CONTENTS

TABLE OF CONTENTS

NANO
THAILAND 2025

Welcome Message

Assoc. Prof. Surin Laosooksathit
President of Nanotechnology Association of Thailand

On behalf of the Nanotechnology Association of Thailand and NANOTEC, it is with great pleasure and privilege to extend a warm invitation to you for participating in the 9th Thailand International Nanotechnology Conference (NanoThailand 2025), which will be held between 3-5 November 2025 at Royal Orchid Sheraton Riverside Hotel Bangkok, Thailand.

The theme of the conference is “Revolutionizing the Future”. The objectives are to apply nanotechnology in various fields for a better life, to create a platform for knowledge exchange to further advance technological areas, and to exhibit the latest innovations of the industries. In order to realize the objectives of the conference, outstanding keynote speakers, guest speakers and renowned researchers are invited to present significant progress in the areas of their expertise.

The conference will provide a platform for experienced researchers in nanotechnology and practitioners from both academia and industry to meet and share cutting-edge development in the field.

On behalf of the organizing committee, we would like to express our strong belief the participating in the NanoThailand 2025 will be a memorable experience, and we look forward to welcoming you to Thailand.

NANO
THAILAND 2025

Welcome Message

Dr. Uracha Ruktanonchai
Executive Director of the National Nanotechnology Center (NANOTEC)
and Chairperson of NanoThailand 2025 Organizing Committee

On behalf of the National Nanotechnology Center, it is my great pleasure and privilege to extend a warm invitation to you all for participating the 9th Thailand International Nanotechnology Conference (NanoThailand 2025). The conference will be held during 3-5 November 2025 at Royal Orchid Sheraton Riverside Hotel Bangkok, Thailand. I would like to take this opportunity to express my sincere appreciation to the Nanotechnology Association of Thailand to co-host this conference.

The theme of the conference is “Revolutionizing the Future”. The objectives are to apply nanoscience and nanotechnology for a better life and well-being to create a platform for knowledge exchange and to exhibit the latest innovations to the industries. At present, we are collaborating in areas such as e-science, renewable energy and the development of novel drugs to combat a range of infectious diseases. Therefore, Science, Technology, Innovation and technology know-how cooperation among peers are very important. NanoThailand 2025 will provide a platform for experienced researchers in nanotechnology and practitioners from both academics, as well as industry to meet and share cutting-edge development in the field. In order to meet the objectives of the conference, the world renowned speakers, and researchers are invited to present the advancement of nanoscience and to update trend of the World’s nanotechnology of their expertise.

I would like to welcome all participants, and to our overseas friends, please enjoy the breath and depth of Science and Technology at the upcoming NanoThailand 2025 (3-5 November 2025) in the vibrant chao phraya river of Bangkok, Thailand where you could also take times to absorb many attractive sites there is to offer in Bangkok, Thailand.

NanoThailand 2025
Organizing Committee

International Advisory Committee

Asst. Prof. Safakath Karuthedath	Tsinghua University, China
Dr. Jer-lai Kuo	Academia Sinica, Taiwan
Asst. Prof. Yen-Hung Lin	The Hong Kong University of Science and Technology,Hong Kong
Prof. Alejandro Montoya	The University of Sydney, Australia
Prof. Akira Nakayama	The University of Tokyo, Japan
Prof. Günther Rupprechter	Vienna University of Technology, Austria
Asst. Prof. Makhsud Saidaminov	University of Victoria, Canada
Prof. Ming-Kang Tsai	National Taiwan Normal University, Taiwan
Prof. Chuanyi Wang	Shaanxi University of Science & Technology, China
Prof. Jen-Shiang K. Yu	National Yang Ming Chiao Tung University, Taiwan
Prof. Ruiqin Zhang	City University of Hong Kong, Hong Kong
Assoc. Prof. Erica J. Marti	University of Nevada, USA

Organizing Committee

Assoc. Prof. Surin Laosooksathit	Advisory	Nanotechnology Association of Thailand
Mr. Por Punyaratabandhu	Advisory	Nanotechnology Association of Thailand
Mr. Phoosak Hiranyatrakul	Advisory	Nanotechnology Association of Thailand
Dr. Uracha Ruktanonchai	Chairperson	National Nanotechnology Center
Dr. Wiyong Kangwansupamonkon	Vice Chair	National Nanotechnology Center
Prof. Siwaporn Meejoo Smith	Committee	National Nanotechnology Center
Mrs. Sansanee Huabsomboon	Committee	National Nanotechnology Center
Dr. Supbhawong Vichaphund	Committee	National Nanotechnology Center
Prof. Sanong Ekgasit	Committee	Chulalongkorn University
Assoc. Prof. Khemarath Osathaphan	Committee	Chulalongkorn University
Prof. Paitoon Rashatasakhon	Committee	Chulalongkorn University
Asst. Prof. Nuankanya Sathirapongsasuti	Committee	Mahidol University
Prof. Tararaj Dharakul	Committee	Mahidol University
Prof. Santi Maensiri	Committee	Suranaree University of Technology
Assoc. Prof. Werasak Surareungchai	Committee	King Mongkut's University of Technology Thonburi
Prof. Supree Pinitsoontorn	Committee	Khon Kaen University
Prof. Metta Chareonpanich	Committee	Kasetsart University
Prof. Vinich Promarak	Committee	Vidyasirimedhi Institute of Science and Technology
Mr. Pongsit Rattanakonvit	Committee	National Nanotechnology Center
Dr. Sanchai Kuboon	Secretary	National Nanotechnology Center

NanoThailand 2025
Organizing Committee

Scientific Committee

Prof. Siwaporn Meejoo Smith	National Nanotechnology Center
Prof. Metta Chareonpanich	Kasetsart University
Prof. Vinich Promarak	Vidyasirimedhi Institute of Science and Technology
Asst. Prof. Pichaya Pattanasattayavong	Vidyasirimedhi Institute of Science and Technology
Prof. Nisanart Traiphol	Chulalongkorn University
Prof. Tararaj Dharakul	Mahidol University
Asst. Prof. Primana Punnakitikashem	Mahidol University
Assoc. Prof. Satit Puttipipatkhachorn	Mahidol University
Prof. Supree Pinitsoontorn	Khon Kaen University
Assoc. Prof. Theeranun Siritanon	Suranaree University of Technology
Assoc. Prof. Prayoon Songsiriritthigul	Synchrotron Light Research Institute
Dr. Narong Chanlek	Synchrotron Light Research Institute
Prof. Siriporn Jungsuttiwong	Ubon Ratchathani University
Assoc. Prof. Khemarath Osathaphan	Chulalongkorn University
Dr. Pongkarn Chakthranont	National Nanotechnology Center
Dr. Sanchai Kuboon	National Nanotechnology Center
Dr. Waluree Thongkam	National Nanotechnology Center
Dr. Chalita Ratanatawanate	National Nanotechnology Center
Dr. Wittaya Pimtong	National Nanotechnology Center
Dr. Thitikorn Boonkoom	National Nanotechnology Center
Dr. Nakarin Subjalearndee	National Nanotechnology Center
Dr. Nattika Saengkrit	National Nanotechnology Center
Dr. Khomson Suttisintong	National Nanotechnology Center
Dr. Itthi Chatnuntawech	National Nanotechnology Center
Dr. Mattaka Khongkow	National Nanotechnology Center
Dr. Chutima Vanichvattanadecha	National Nanotechnology Center
Dr. Kanokporn Tangthana-umrung	National Nanotechnology Center
Dr. Saowaluk Chaleawlert-Umpon	National Nanotechnology Center
Dr. Supone Manakasettharn	National Nanotechnology Center
Dr. Pisist Kumnorkaew	National Nanotechnology Center
Dr. Weerakanya Maneeprakorn	National Nanotechnology Center
Dr. Suwussa Bamrungsap	National Nanotechnology Center
Dr. Deanpen Japrung	National Nanotechnology Center
Dr. Kajornsak Faungnawakij	National Nanotechnology Center
Dr. Pongtanawat Khemthong	National Nanotechnology Center
Dr. Supawadee Namuangruk	National Nanotechnology Center
Miss. Jirapat Santatiwongchai	National Nanotechnology Center

NanoThailand 2025
Organizing Committee

Technical Committee

Prof. Siwaporn Meejoo Smith	National Nanotechnology Center
Dr. Saowaluk Chaleawlert-Umpon	National Nanotechnology Center
Dr. Annop Klamchuen	National Nanotechnology Center
Dr. Nuttaporn Pimpha	National Nanotechnology Center
Dr. Kittiwut Kasemwong	National Nanotechnology Center
Dr. Udom Asawapirom	National Nanotechnology Center
Dr. Vorranutch Itthibenchapong	National Nanotechnology Center
Dr. Aniwat Pengsawang	National Nanotechnology Center
Dr. Sirapassorn Kiatphuengporn	National Nanotechnology Center
Dr. Pongtanawat Khemthong	National Nanotechnology Center
Dr. Kajornsak Faungnawakij	National Nanotechnology Center
Dr. Supawadee Namuangruk	National Nanotechnology Center
Dr. Itthi Chatnuntawech	National Nanotechnology Center
Dr. Waluree Thongkam	National Nanotechnology Center
Dr. Wittaya Pimtong	National Nanotechnology Center
Dr. Deanpen Japrung	National Nanotechnology Center
Dr. Thitikorn Boonkoom	National Nanotechnology Center
Dr. Pongkarn Chakthranont	National Nanotechnology Center
Dr. Sanchai Kuboon	National Nanotechnology Center
Prof. Metta Chareonpanich	Kasetsart University
Assoc. Prof. Waleeporn Donphai	Kasetsart University
Dr. Thidarat Imyen	Kasetsart University
Prof. Nanthiya Hansupalak	Kasetsart University
Dr. Kulpavee Jitapunkul	Kasetsart University
Asst. Prof. Patraporn Luksirikul	Kasetsart University
Dr. Suthasinee Watmanee	Kasetsart University
Prof. Thongthai Witoon	Kasetsart University
Assoc. Prof. Anusorn Seubsai	Kasetsart University
Assoc. Prof. Manop Charoenchaitrakool	Kasetsart University
Assoc. Prof. Kandis Sudsakorn	Kasetsart University
Assoc. Prof. Apirat Laobuthee	Kasetsart University
Asst. Prof. Supacharee Roddecha	Kasetsart University
Asst. Prof. Viganda Varabuntoonvit	Kasetsart University
Assoc. Prof. Atthapon Srifa	Kasetsart University
Dr. Khemmathin Lueangwattanapong	Kasetsart University
Assoc. Prof. Chalida Niamnuy	Kasetsart University
Prof. Siriporn Jungsuttiwong	Kasetsart University
Assoc. Prof. Paweena Prapainainar	Kasetsart University
Prof. Paisan Kongkachuichay	Kasetsart University

NanoThailand 2025
Organizing Committee

Technical Committee

Prof. Suttichai Assabumrungrat	Chulalongkorn University
Dr. Bhumin Than-ardna	Chulalongkorn University
Prof. Boonyarach Kitiyanan	Chulalongkorn University
Dr. Chitiphon Chuaicham	Chulalongkorn University
Prof. Nisanart Traiphol	Chulalongkorn University
Assoc. Prof. Pornapa Sujaridworakun	Chulalongkorn University
Assoc. Prof. Dujreutai Pongkao Kashima	Chulalongkorn University
Asst. Prof. Karn Serivalsatit	Chulalongkorn University
Asst. Prof. Prasit Pattananuwat	Chulalongkorn University
Dr. Wuttichai Reainthippayasakul	Chulalongkorn University
Assoc. Prof. Khemarath Osathaphan	Chulalongkorn University
Assoc. Prof. Jenyuk Lohwacharin	Chulalongkorn University
Assoc. Prof. Patiparn Punyapalakul	Chulalongkorn University
Dr. Noppakhate Jiraborvornpongsa	Chulalongkorn University
Assoc. Prof. Supareak Praserthdam	Chulalongkorn University
Asst. Prof. Nopporn Rujisamphan	King Mongkut's University of Technology Thonburi
Dr. Mithran Somasundrum	King Mongkut's University of Technology Thonburi
Dr. Patsamon Rijiravanich	King Mongkut's University of Technology Thonburi
Asst. Prof. Muralikrishna Sreeramareddygari	King Mongkut's University of Technology Thonburi
Asst. Prof. Surachate Kalasin	King Mongkut's University of Technology Thonburi
Prof. Navadol Laosiripojana	King Mongkut's University of Technology Thonburi
Assoc. Prayoon Songsiriritthigul	Synchrotron Light Research Institute
Dr. Narong Chanlek	Synchrotron Light Research Institute
Dr. Pinit Kidkhunthod	Synchrotron Light Research Institute
Dr. Wanwisa Limphirat	Synchrrotron Light Research Institute
Assoc. Prof. Theeranun Siritanon	Suranaree University of Technology
Assoc. Prof. Wittawat Saenrung	Suranaree University of Technology
Assoc. Prof. Chularat Wattanakit	Vidyasirimedhi Institute of Science and Technology
Prof. Vinich Promarak	Vidyasirimedhi Institute of Science and Technology
Asst. Prof. Pichaya Pattanasattayavong	Vidyasirimedhi Institute of Science and Technology
Assoc. Prof. Khanin Nueangnoraj	Thammasat University
Assoc. Prof. Chanatip Samart	Thammasat University
Assoc. Prof. Piyarat Nimmanpipug	Chiang Mai University
Assoc. Prof. Burapat Inceesungvorn	Chiang Mai University
Assoc. Prof. Apinpus Rujiwatra	Chiang Mai University
Prof.Supree Pinitsoontorn	Khon Kaen University
Dr. Jirawat Trakulmututa	Thailand Institute of Nuclear Technology
Assoc. Prof. Christopher Smit	Kamnoetvidya Science Academy

NANO THAILAND 2025

Session Chairs and Co-chairs

Session 1 : Green Catalysis for Sustainable Consumption and Production	**Chair :** Prof. Metta Chareonpanich **Co-Chair :** Dr. Kajornsak Faungnawakij Prof. Thongthai Witoon Assoc. Prof. Chularat Wattanakit
Session 2 : Nanomaterials, Nanocoating and Nanotechnology for Electronic/Optoelectronic Devices and Sensors	**Chair :** Prof. Vinich Promarak **Co-Chair :** Asst. Prof. Pichaya Pattanasattayavong Dr. Pisist Kumnorkaew Dr. Supone Manakasettharn
Session 3 : Smart Nanomaterials and Nanocomposites	**Chair :** Prof. Nisanart Traiphol **Co-Chair :** Dr. Chutima Vanichvattanadecha Dr. Kanokporn Tangthana-umrung
Session 4 : Nanotechnology in Healthcare: Diagnostics, Therapeutics, and Beyond	**Chair :** Prof. Tararaj Dharakul **Co-Chair :** Dr. Weerakanya Maneeprakorn Dr. Mattaka Khongkow Asst. Prof. Primana Punnakitikashem Dr. Suwussa Bamrungsap
Session 5 : Next-Gen Nanoencapsulation Across Food, Cosmetic, and Agricultural Frontiers	**Chair :** Assoc. Prof. Satit Puttipipatkhachorn **Co-Chair :** Dr. Nattika Saengkrit Dr. Khomson Suttisintong
Session 6 : Nanotechnology for Energy Storage and Management	**Chair :** Prof. Supree Pinitsoontorn Assoc. Prof. Theeranun Siritanon **Co-Chair :** Dr. Nakarin Subjalearndee
Session 7 : Advanced Nanomaterial Characterization and Modern Instrumentation	**Chair :** Prof. Prayoon Songsiriritthigul **Co-Chair :** Dr. Pongtanawat Khemthong Dr. Narong Chanlek
Session 8 : Computational Nanotechnology & AI/Data Science	**Chair :** Prof. Siriporn Jungsuttiwong **Co-Chair :** Dr. Supawadee Namuangruk Dr. Itthi Chatnuntawech
Session 9 : Nanosafety and Standards	**Chair :** Dr. Waluree Thongkam **Co-Chair :** Dr. Wittaya Pimtong
Session 10 : Nanopore Technology	**Chair :** Dr. Deanpen Japrung **Co-Chair :** Dr. Thitikorn Boonkoom
Session 11 : Nanotechnology for Environmental Sustainability	**Chair :** Assoc. Prof. Khemarath Osathaphan **Co-Chair :** Dr. Chalita Ratanatawanate
Session 12 : [Special Session] Capture the Future with CCUS Technology	**Chair :** Dr. Kajornsak Faungnawakij **Co-Chair :** Dr. Pongkarn Chakthranont Dr. Sanchai Kuboon

Chelating-Solvothermal Synthesis of High-Performance Bimetallic Fe-Co Nanoparticles for Enhanced Oxygen Evolution Reaction in Alkaline Media

Prawploy Phimnean[1,2], Laksamee Payattikul[1,2], Konlayutt Punyawudho[1,2 *]
[1]*Energy Harvesting and Storage Laboratory, Chiang Mai University, 50200, Thailand*
[2]*Department of Mechanical Engineering, Faculty of Engineering, Chiang Mai University, 50200, Thailand*
[*]*E-mail: konlayutt.p@cmu.ac.th*

Abstract:

Efficient and cost-effective electrocatalysts for the Oxygen Evolution Reaction (OER) are paramount for sustainable hydrogen production *via* water electrolysis. This study reports a facile synthesis of bimetallic Fe-Co nanoparticles on Ketjen black carbon (FeCo/K) through a chelating-agent-assisted solvothermal method followed by pyrolysis at varied conditions (400–600 °C, 0.5–2 h). Structural characterization using TEM and XRD confirmed the formation of well-dispersed, body-centered cubic (BCC) Fe-Co alloy nanoparticles. Among the synthesized materials, the catalyst pyrolyzed at 500 °C for 2 hours (FeCo/K500-2h) demonstrated superior OER activity in 1 M KOH. It required a low overpotential of only 318.5 mV to achieve a current density of 10 mA cm^{-2}, which surpasses the benchmark RuO_2 catalyst (331 mV). Furthermore, its small Tafel slope of 52.8 mV dec^{-1} signifies highly favorable reaction kinetics. This enhanced performance is attributed to an optimal synergy between the Fe-Co alloy, well-controlled crystallinity, and the abundance of metal-nitrogen-carbon (M-N-C) active sites derived from the chelating agent. Our work therefore provides a promising strategy for the rational design of earth-abundant electrocatalysts for practical water electrolysis applications.

1. Introduction

The escalating global energy demand and pressing environmental concerns have catalyzed a paradigm shift from fossil fuels towards sustainable energy sources. In this context, green hydrogen produced *via* water electrolysis powered by renewable electricity is recognized as a cornerstone of a future carbon-neutral energy economy. The overall efficiency of water electrolysis, which consists of the hydrogen evolution reaction (HER) and the oxygen evolution reaction (OER), is predominantly hindered by the sluggish kinetics of the OER due to its complex four-electron transfer process. While state-of-the-art OER electrocatalysts are based on precious metal oxides like IrO_2 and RuO_2, their widespread application is severely limited by their high cost, scarcity, and limited long-term stability in alkaline media. This necessitates the urgent development of efficient, durable, and cost-effective OER catalysts from earth-abundant elements.

Among various alternatives, transition metals such as iron (Fe), cobalt (Co), and nickel (Ni) have emerged as highly promising candidates due to their intrinsic catalytic activity and low cost. Bimetallic alloys, particularly Fe-Co systems, often exhibit enhanced electrocatalytic performance compared to their monometallic counterparts. This enhancement stems from a synergistic electronic effect, where the presence of Fe can modulate the d-band center of Co, thereby optimizing the adsorption energies of OER intermediates (e.g., *OH, *O, *OOH) and lowering the overall activation energy barrier.[1] To maximize their potential, these nanoparticles are typically anchored on highly conductive carbon supports, which not only prevent nanoparticle agglomeration but also ensure efficient electron transport pathways throughout the electrode. Furthermore, a highly effective strategy to boost performance is the incorporation of nitrogen (N) heteroatoms into the carbon matrix. N-doping modifies the electronic structure of carbon and, critically, facilitates the formation of metal-nitrogen-carbon (M-N-C) coordination sites, which are believed to be exceptionally active centers for OER catalysis. [2]

While these individual strategies–alloying, carbon support, and N-doping–are well-documented, the novelty of this work lies in our specific synthesis methodology and the systematic investigation of its processing parameters. We employ a chelating-agent-assisted solvothermal method where 1,10-phenanthroline serves a critical dual function. Initially, it acts as a chelating agent to promote the controlled, homogeneous nucleation of Fe and Co precursors on the carbon support. Subsequently, during pyrolysis, this same molecule decomposes to serve as an in-situ source for nitrogen, directly facilitating the creation of the desired FeCo@N-C structures. However, the influence of the final pyrolysis conditions (temperature and duration) on the structural and electrochemical properties of catalysts prepared via this integrated approach remains inadequately

understood. A critical trade-off exists between achieving high alloy crystallinity at elevated temperatures and the concurrent risks of particle sintering and degradation of thermally sensitive M-N-C active sites. Therefore, this study undertakes a systematic investigation of pyrolysis parameters to elucidate structure-activity relationships. By correlating the physical and electrochemical properties, we aim to identify the optimal synthesis window that balances these competing factors to produce a highly efficient and robust Fe-Co OER electrocatalyst.

temperature for durations of 0.5 hours, 1 hour, and 2 hours, respectively shown in Figure 1.

2.3 Characterization

The structural characteristics of the bimetallic Fe-Co nanoparticles were examined through the application of transmission electron microscopy (TEM). TEM images were obtained utilizing a JEOL-2100 Plus, functioning at an accelerating voltage of 200 kV. Moreover, the X-ray diffraction (XRD, Rigaku SmartLab) utilizing Cu-Kα radiation was conducted to assess the crystallinity structure of the synthesized

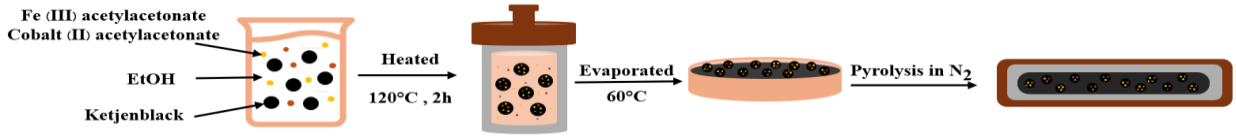

Figure 1. Synthesis of bimetallic Fe-Co nanoparticles by using solvothermal method.

2. Materials and Methods

2.1 Materials

Material used for the synthesis electrocatalyst nanoparticles were cobalt (II) acetylacetonate (Sigma-Aldrich) and iron (III) acetylacetonate (Sigma-Aldrich) as metal precursors. Ethanol (RCl Labscan) served as the solvent for solution preparation. The 1,10-phenanthroline monohydrate (Kemaus, analytical reagent) served as a chelating agent, while Ketjen black (EC-600JD) functioned as the supported carbon.

2.2 Synthesis

The synthesis began by accurately weighing out 0.0197 g of cobalt (II) acetylacetonate and 0.0256 g of iron (III) acetylacetonate. These metal precursors, along with 0.1953 g of 1,10-phenanthroline monohydrate, were then dissolved in ethanol (6:1 molar ratio 1,10-phenanthroline monohydrate to metal). The solution was sonicated for 10 minutes to ensure complete dissolution and uniform mixing. Following this, 0.0698 g of Ketjen black carbon was added, and the mixture underwent an additional 20 minutes of sonication to achieve a well - dispersed suspension. The resulting mixture was placed into a Teflon-lined stainless-steel autoclave and underwent solvothermal treatment at 120°C for a duration of 2 hours. Following the solvothermal process, ethanol was evaporated from the ensuing dispersion, yielding a black solid. This solid was then pulverized using a mortar and pestle and transferred to a ceramic crucible. Finally, the material underwent pyrolysis in a nitrogen (N_2) gas atmosphere. The samples were heated to 400°C, 500°C, and 600°C at a ramp rate of 10°C min^{-1}, maintaining each sample and the element composition in the FeCo on Ketjenblack carbon catalyst was using HRTEM with Energy Dispersive Spectroscopy (EDS).

The electrochemical properties of our synthesized Fe-Co/K electrocatalysts were evaluated. The catalyst inks were prepared by dispersing 2 mg of the electrocatalyst in a solution containing 0.114 mL of deionized water and ethanol, along with 0.030 mL of a 5 wt% PFSA solution. This mixture was then sonicated for 20 minutes to ensure homogeneity. A 0.25 cm^2 section of Ni foam (1 mm thickness) was used as the working electrode substrate, and the catalyst ink was applied to achieve a consistent catalyst loading of 0.7 µg catalyst/cm^2. Oxygen Evolution Reaction (OER) activities were assessed using a Pine Instrument Co. bi-potentiostat in a standard three-electrode configuration. A platinum wire served as the counter electrode, an Ag/AgCl electrode in 3M KCl solution was used as the reference electrode, and the Ni foam with electrocatalysts acted as the working electrode. All OER tests were performed at room temperature in a 0.5 M potassium hydroxide (KOH) solution under a nitrogen atmosphere. The overpotentials and Tafel 5 sweep voltammograms (LSV) at a scan rate of 5 mV s^{-1}.

3. Results

3.1 Bimetallic Fe-Co nanoparticles on carbon support.

The morphology and dispersion of the synthesized bimetallic nanoparticles were investigated using Transmission Electron Microscopy (TEM). As depicted in Figure 2, the TEM images confirm the successful decoration of Fe-Co nanoparticles onto the surface of the Ketjen black (K) carbon support across all pyrolysis conditions. The nanoparticles generally

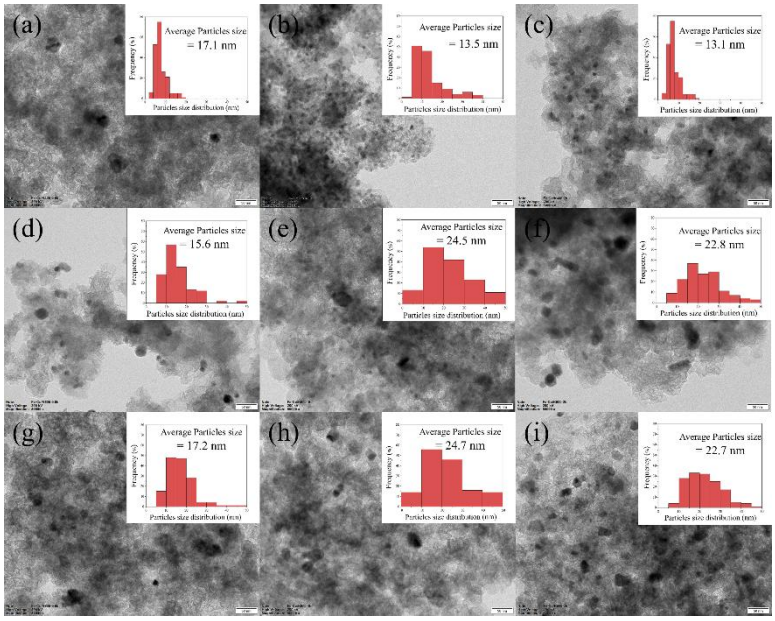

Figure 2. TEM images of Fe-Co nanoparticles (a) FeCo/K400-0.5h (b) FeCo/K500-0.5h (c) FeCo/K600-0.5h (d) FeCo/K400-1h (e) FeCo/K500-1h (f) FeCo/K600-1h (g) FeCo/K400-2h (h) FeCo/K500-2h, and (i) FeCo/K600-2h.

exhibit a quasi-spherical shape and are well-distributed, which is crucial for maximizing the exposure of active sites and facilitating efficient mass transport. A detailed analysis of the particle size, summarized in Table 1, reveals a strong dependence on the pyrolysis temperature and duration. At a short pyrolysis time of 0.5 hours, the average particle sizes are relatively consistent, ranging from 15.6 nm to 17.2 nm. However, as the pyrolysis duration and temperature increases, a clear trend of particle growth due to sintering is observed. For instance, when pyrolyzed for 1 hour, the average particle size increased from 13.5 nm at 400°C to 24.7 nm at 600°C. This phenomenon is expected, as higher thermal energy promotes atomic diffusion and agglomeration, leading to the formation of larger, more thermodynamically stable nanoparticles. The sample FeCo/K500-2h, which later shows the highest electrocatalytic activity, possesses an average particle size of 22.8 nm. The synthesis strategy, employing 1,10-phenanthroline as a chelating agent, plays a dual role that is critical to the material final structure. During the initial solvothermal step, it coordinates with Fe and Co ions, preventing premature precipitation and promoting the formation of uniformly sized precursor complexes on the carbon support.[3] Subsequently, during high-temperature pyrolysis under a nitrogen atmosphere, the 1,10-phenanthroline decomposes. This process not only facilitates the reduction of metal ions to their metallic state, forming the Fe-Co alloy, but it also serves as a source for in-situ nitrogen doping of the carbon matrix.[4] HRTEM/EDS analysis of the optimal FeCo/K500-2h catalyst (Figure 3) quantifies the elemental composition as 1.40 wt% N, 2.00 wt% Fe, and 2.29 wt% Co. The elemental mapping confirms the spatial co-location and overlaps of Fe and Co, providing strong evidence for the successful formation of a bimetallic alloy.

Table 1. Average particle size of Fe-Co nanoparticles and %wt ratio of Fe and Co at different times and temperatures.

Catalyst	Average Particle Size (nm)	%wt	
		Fe	Co
FeCo/K400-0.5h	17.1	1.62	1.79
FeCo/K500-0.5h	15.6	3.37	5.25
FeCo/K600-0.5h	17.2	1.09	2.25
FeCo/K400-1h	13.5	1.20	2.66
FeCo/K500-1h	24.5	1.69	1.96
FeCo/K600-1h	24.7	2.00	2.29
FeCo/K400-2h	13.1	1.39	1.48
FeCo/K500-2h	22.8	1.80	1.93
FeCo/K600-2h	22.7	2.62	1.22

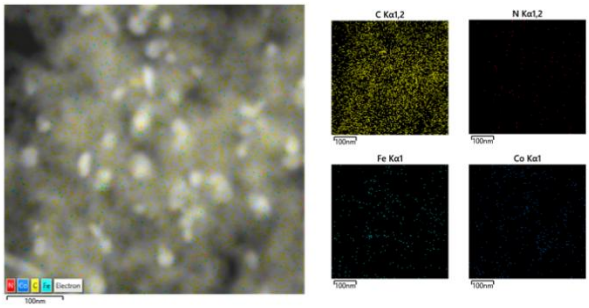

Figure 3. HRTEM image of FeCo/K500-2h catalysts with EDS elemental mapping.

To investigate the crystal structure and phase composition, X-ray Diffraction (XRD) analysis was performed on all synthesized samples, with the results presented in Figure 4. XRD patterns for all catalysts are dominated by two broad diffraction peaks centered at 2θ ≈ 25.5° and 45° which corresponds to the (002) and (100) corresponding to the (002) and (100) planes of the Ketjen black graphitic support.[5] Due to the very low metal loading (3–5 wt%), the diffraction signals originating from the FeCo nanoparticles are too weak to be clearly distinguished from the intense, broad background signal of the abundant carbon support.

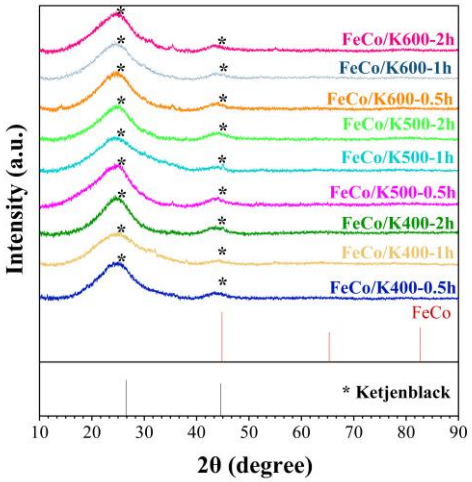

Figure 4. XRD results for all samples alongside standard references of Fe, Co, FeCo, and Carbon.

3.2 Electrochemical OER performance

The OER activity of the synthesized Fe-Co/K electrocatalysts was rigorously evaluated in an alkaline medium (1 M KOH) using a standard three-electrode setup. The linear sweep voltammetry (LSV) polarization curves are presented in Figure 5 (a-c).

A key metric for catalyst performance is the overpotential (η) required to achieve a current density of 10 mA cm^{-2}, a benchmark relevant to solar fuel production systems.[6] The electrochemical data, summarized in Table 2, demonstrates the remarkable performance of the synthesized catalysts, with several formulations outperforming the commercial RuO_2 benchmark (η = 331 mV). The catalyst performance is highly sensitive to the pyrolysis conditions. The most active catalyst identified is FeCo/K500-2h, which performs a minimal overpotential of just 318 mV to reach 10 mA cm^{-2}. This superior activity highlights the efficacy of the synthesis protocol. Notably, this catalyst surpasses not only the other prepared samples, such as FeCo/K400-1h (η = 320 mV), but also the expensive, noble-metal-based RuO_2.

To explore the reaction kinetics further, Tafel slopes were derived from the LSV curves (Figure 5d-f). The Tafel slope provides insight into the rate-determining step of the OER mechanism, with lower values indicating more favorable kinetics.[7] The FeCo/K500-2h catalyst exhibits the lowest Tafel slope of 52.8 mV dec^{-1}. This value is significantly smaller than that of many reported non-precious metal catalysts and suggests highly favorable reaction kinetics.[8] A lower Tafel slope indicates that a smaller increase in overpotential is needed to achieve a substantial increase in reaction rate, signifying rapid charge-transfer processes at the catalyst-electrolyte interface.[7]

Table 2. Electrocatalytic performance (Oxygen Evolution Reaction, OER) of FeCo nanoparticles.

Catalyst	Overpotential (10 mA.cm^2)	Tafel slope
FeCo/K400-0.5h	331.5	64.8
FeCo/K500-0.5h	334.4	61.2
FeCo/K600-0.5h	332.5	60.1
FeCo/K400-1h	320.2	67.2
FeCo/K500-1h	327.8	60.8
FeCo/K600-1h	340.5	67.0
FeCo/K400-2h	323.8	52.5
FeCo/K500-2h	318.5	52.8
FeCo/K600-2h	318.2	99.3

The superior performance of FeCo/K500-2h, despite its relatively large particle size (22.8 nm), suggests that catalytic activity in this system is not solely dictated by the available surface area. Instead, the intrinsic activity of the catalytic sites is paramount.[9] The pyrolysis condition of 500°C for 2 hours appears to strike an optimal balance. It is sufficiently high to ensure good crystallinity of the Fe-Co alloy and the formation of a highly conductive. The synergy between Fe and Co is optimized under these conditions, leading to an ideal electronic structure that lowers the energy barrier for the adsorption and conversion of OER intermediates (e.g., OH^-, OOH^-).[10] The combination of bimetallic synergy, high conductivity, and the abundance of highly active M-N-C active sites created under these specific pyrolysis conditions culminates in the outstanding OER performance observed.

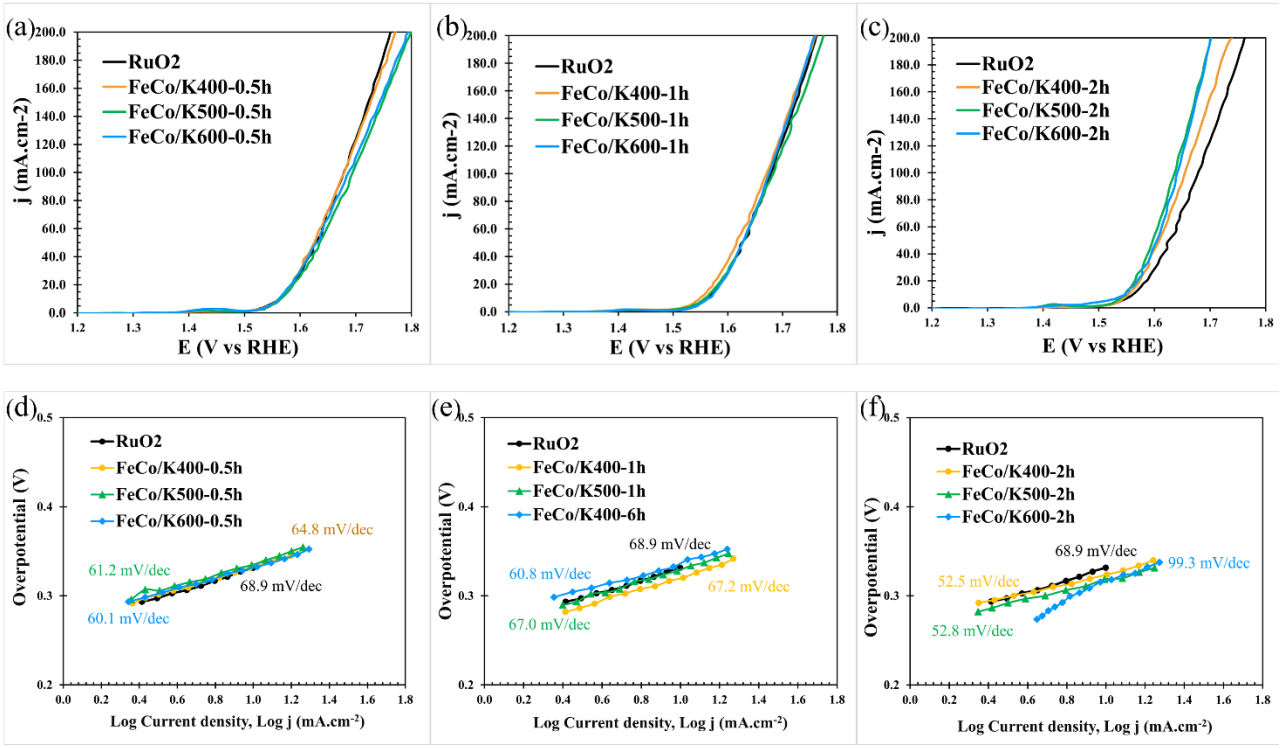

Figure 5. (a) 0.5 hours, (b) 1 hour, and (c) 2 hours shows the OER polarization curve and (d) 0.5 hours (e) 1 hours (f) 2 hours shows the Tafel slope of pyrolysis Fe-Co nanoparticles at three different time intervals.

Conclusion

In this study, bimetallic Fe-Co nanoparticles supported on Ketjen black carbon were successfully synthesized via a facile chelating-agent-assisted solvothermal method followed by a systematic pyrolysis process. Structural characterizations confirmed the formation of well-dispersed Fe-Co alloy nanoparticles, with crystalline and particle size increasing at higher pyrolysis temperatures. Electrochemical evaluations for the OER revealed that the pyrolysis conditions critically dictate the catalytic performance. The optimal catalyst, FeCo/K500-2h, prepared at 500 °C for 2 hours, exhibited superior activity with a low overpotential of 318.5 mV at 10 mA cm^{-2}, outperforming the benchmark RuO_2 catalyst

This was complemented by a small Tafel slope of 52.8 mV dec^{-1}, indicating favorable reaction kinetics. The enhanced performance is attributed to an optimal balance achieved under these specific conditions: the formation of a highly crystalline, synergistic Fe-Co alloy phase without inducing excessive particle sintering. Critically, the use of 1,10-phenanthroline as a dual-function chelating agent and in-situ nitrogen source was instrumental in creating abundant metal-nitrogen-carbon (M-N-C) active sites.

In conclusion, this work not only presents a high-performance, cost-effective OER electrocatalyst but also provides valuable insights into the rational design of advanced catalysts, highlighting the importance of tuning pyrolysis parameters to optimize the interplay between crystallinity, morphology, and surface-active sites for energy conversion applications.

Acknowledgements

The authors wish to express their deepest gratitude to Chiang Mai University and the Department of Mechanical Engineering, Faculty of Engineering for providing outstanding research environment, including access to state-of-the-art instrumentation and facilities that were essential for conducting our experiments. Finally, our sincere thanks go to our home, the Energy Harvesting and Storage Laboratory (EHAS).

References

1. Friebel, D.; Louie, M. W.; Bajdich, M.; Sanwald, K. E.; Cai, Y.; Wise, A. M.; Cheng, M. J.; Sokaras, D.; Weng, T. C.; Alonso-Mori, R.; Davis, R. C.; Bargar, J. R.; Nørskov, J. K.; Nilsson, A.; Bell, A. T., Identification of Highly Active Fe Sites in (Ni,Fe)OOH for Electrocatalytic Water Splitting. *J. Am. Chem. Soc.* **2015**, *137*, 1305–1313.
2. Zhang, H.; Liu, Y.; Chen, T.; Zhang, J.; Zhang, J.; Lou, X. W. D., Unveiling the Activity Origin of Electrocatalytic Oxygen Evolution over Isolated Ni Atoms Supported on a N-Doped Carbon Matrix. *Adv. Mater.* **2019**, *31*, 1904423.

3. Xia, B. Y.; Yan, Y.; Li, N.; Wu, H. B.; Lou, X. W. D.; Wang, X., A metal-organic framework-derived bifunctional oxygen electrocatalyst. *Nat. Energy* **2016**, *1*, 15006.
4. Liang, J.; Jiao, Y.; Jaroniec, M.; Qiao, S. Z., Sulfur and Nitrogen Dual-Doped Mesoporous Graphene Electrocatalyst for Oxygen Reduction with Synergistically Enhanced Performance. *Angew. Chem., Int. Ed.* **2012**, *51*, 11496–11500.
5. Jiang, S.; Huang, P.; Lu, J.; Liu, Z., The electrochemical performance of fluorinated ketjenblack as a cathode for lithium/fluorinated carbon batteries. *RSC Adv.* **2021**, *11*, 25461–25470.
6. Guo, D.; Shibuya, R.; Akiba, C.; Saji, S.; Kondo, T.; Nakamura, J., Active sites of nitrogen-doped carbon materials for oxygen reduction reaction clarified using model catalysts. *Science*. **2016**, *351*, 361–365.
7. Seh, Z. W.; Kibsgaard, J.; Dickens, C. F.; Chorkendorff, I.; Nørskov, J. K.; Jaramillo, T. F., Combining theory and experiment in electrocatalysis: Insights into materials design. *Science.* **2017***, 355*, eaad4998.
8. Canales, C.; Olea, A. F.; Gidi, L.; Arce, R.; Ramírez, G., Enhanced Light-Induced Hydrogen Evolution Reaction by Supramolecular Systems of Cobalt (II) and Copper (II) Octaethylporphyrins on Glassy Carbon Electrodes. *Electrochim. Acta* **2017**, *258*, 850–857.
9. McCrory, C. C. L.; Jung, S.; Ferrer, I. M.; Chatman, S. M.; Peters, J. C.; Jaramillo, T. F., Benchmarking Hydrogen Evolving Reaction and Oxygen Evolving Reaction Electrocatalysts for Solar Water Splitting Devices. *J. Am. Chem. Soc.* **2015**, *137*, 4347–4357.
10. Suen, N.-T.; Hung, S.-F.; Quan, Q.; Zhang, N.; Xu, Y.-J.; Chen, H. M., Electrocatalysis for the oxygen evolution reaction: recent development and future perspectives. *Chem. Soc. Rev.* **2017**, *46*, 337–361.

Molecularly Imprinted Polymers Using Eco-friendly Materials in Nanocapsules for Enhancing Delivery of Cannabidiol, Monoclonal Antibodies, and Insulin

Kanok-on Jaisawan, Jittiya Rodruksa, Pistawus Khomintr, Roongnapa Suedee*, Watchara Pholthien
Department of Pharmaceutical Chemistry, Faculty of Pharmaceutical Sciences, Prince of Songkla University, Hatyai, Songkhla 90112, Thailand
**E-mail: roongnapa.s@psu.ac.th*

Abstract:

This study introduces eco-friendly biocomposite nanolayers and nanocapsules tailored for 3D-printed injectable drug delivery systems. By using molecularly imprinted polymers (MIPs) based on polycaprolactone-triol (PCL-T), we improve the delivery of therapeutic agents, including cannabidiol (CBD), monoclonal antibodies, and insulin. Our analysis of surface interactions and material composition shows positive effects on protein integrity and charge stability. We found that poorly soluble CBD and proteins can enhance solubility through salt interactions, while enzyme-exposed dried nanocapsules create optimal structures for capturing and imaging. Our findings highlight strong interparticle interactions in customized CBD formulations and reveal new recycling methods for MIP nanocapsules. Our findings show that high-CBD formulations yield isolated charged particles, with ligands that are crucial for achieving higher CBD diastereomer concentrations in biocomposite nanocapsules. The modified MIPs targeting CBD diastereomers enhance human serum albumin (HSA) capture, the conformation and topology of the protein at the interfacial solvent structure, leading to uniform cluster formation. Combining MIP with PCL-T, rather than using the oily gel from the filtrate, improves enzyme immobilization and protein uptake. Process Analysis Technologies (PAT) suggests that crystalline drugs may hinder diffusion during biodegradation. X-ray Fluorescence (XRF) microscopy indicates that phosphorus-calcium interactions enhance protein uptake and facilitate the conversion of assemblies into MIP nanocapsules, ultimately improving drug delivery, supporting sustainable drug discovery, and enhancing patient care.

1. Introduction

Nanomedicine is transforming drug delivery systems by enhancing the penetration and bioavailability of hydrophobic drugs and improving the proteolytic resistance of antimicrobial peptides through nanoscale materials.[1] This approach effectively addresses traditional limitations, facilitating efficient transport and targeted release via self-assembled DNA/peptide-based nanoparticles.[2] These systems show considerable potential for delivering biomaterials and biologic drugs across barriers, including disease sites, tissues, organs, and the blood-brain barrier. Research underscores the significance of long-acting injectables, biopharmaceuticals, and nanotheranostic carriers based on serum albumin and polysaccharides.[3,4] Teixeira et al. highlighted the importance of protein interactions, enzyme kinetics, and amino acid functions in preparing epitope-imprinted polymers from synthetic binding partners for biomacromolecules.[5] Nanocapsule molecularly imprinted polymers (MIPs), known as Nanocap MIPs, are created through an innovative co-assembly of peptides, proteins, and small molecules embedded within drug payloads. This method improves targeted drug delivery by leveraging the specificity inherent in molecular imprinting techniques, creating specific binding sites within Human Serum Albumin (HSA) for combining biotherapeutic agents with cannabidiol (CBD).

Adenosine's neuroprotective effects through A1 receptors target excitotoxicity, a key focus in neuromedicine. Our research examines how ATP modulates CBD to reduce oxidative stress and excitotoxicity, which are crucial in neurological disorders. This work supports the development of next-generation antidepressants involving CBD, which has gained recognition for its medical uses, including pediatric dosage forms, cannabidiol suspensions, orodispersible films, and 3D printing.[6] Additionally, peptide fragments and complementary-determining regions (CDRs) enhance the stability and bioavailability of monoclonal antibodies (mAbs) across various therapies.

In this study, we created a premix microgel for 3D printing, suitable for either oral or topical administration, by combining a premade PCL-T oily gel with MIPs at various ratios. The integration of HSA-MIPs, excipients, and PCL-T gels improves rebinding and chiral separation,

which are vital for protein research and biomolecule targeting, especially considering CBD's low water solubility. The structure of PCL-T facilitates interactions between lipophilic proteins and CBD, both of which are amphiphilic. Using a biocomposite nanolayering technique with eco-friendly materials, we create nanoscale layers of MIPs and nanocapsules. We choose eco-friendly MIPs for their slow degradation and susceptibility to enzymatic breakdown, which minimizes allergic reactions and improves bonding in our composites.

We analyze self-association phenomena to assess the storage capacity and biological responses of nanocapsules in phosphate buffer, as well as their behavior during bionanofiltration using a model biomembrane. Machine learning offers insights into protein interactions within nanocapsules, considering factors such as electrolytes, pH, and biodegradability in enzyme-rich environments, which is essential for applications in 3D printing and protein pharmaceutical control.[7] Complementary techniques such as X-ray Fluorescence (XRF), Raman spectroscopy-Atomic-Force Microscopy (AFM), and Liquid Chromatography (LC) with a Quadrupole Time-of-Flight Mass Spectrometer (LC-QTOF-MS) have significantly advanced our efforts in material characterization and optimization. XRF imaging and fluorescence laser emission were used to monitor chemical changes, degradation, and shape transformation, and the Fluorescence Laser Technique (FLT) was used to measure the size of protein nanocapsules. Focusing on self-association during storage and processing is crucial for improving localized drug delivery and immunoassays for complex samples.

2. Materials and Methods

2.1 Materials

Methacryloyl chloride (MAA), ethylene glycol dimethacrylate (EGDMA), HSA, wheat germ agglutinin, human insulin, anti-IgE antibody (specific chain), fusion protein (peroxidase), and PCL-T were obtained from Aldrich (Milwaukee, WI, USA). Lysozyme from hen egg white was purchased from Fluka Chemie (Buchs, Switzerland). Potassium peroxidisulfate, sodium phosphate dibasic anhydrous, and sodium chloride were sourced from Fluka Chemie, while potassium chloride was obtained from Univar (NSW2147, Australia), and sodium monophosphate monohydrate from Sigma-Aldrich.

2.2 Synthesis of HSA MIPs in nanocapsules

MIPs were prepared using cholate-derivatized MAA, EGDMA, and potassium peroxydisulfate, with precipitation polymerization at 80 °C after template removal by a suitable procedure and selection of solvent[5]. Next, the MIP powder, formulation ingredients, lysozyme, and other additives were combined with 1 mL of the CBD ethanol solution and incubated at room temperature for 24 hours to facilitate CBD binding. A drug mixture containing CBD, insulin, mAb, and excipients was formulated into a PCL-T gel.
The in vitro release and protein recovery of CBD from the premixed MIP in the PCL-T oily gel were examined using Franz diffusion cells with various concentrations and mixing ratios, employing PBS at pH 7.4. Samples were periodically taken from the receiving chamber. A total of 500 mg of MIP powder was combined with 1 ml of CBD ethanol solution and incubated at room temperature for 24 hours to facilitate CBD binding. Samples were systematically collected, and 200 µl of supernatant was filtered through a 0.45 µm VentPure™ Nylon filter. The donor chamber contained different concentrations of CBD in nanosuspension. The samples were transferred to 96-well plates and analyzed with a MicroMax 384 reader, measuring fluorescence intensity at 280 nm excitation and 307 nm emission via a Fluoromax 4P Spectrometer.

2.3 Characterization

Fluorescence image analysis

The FLT based on Fluorescence microscopy was performed with a Fluorescence Stereo Microsystem (Leica M205 FCA, Switzerland) using two probes (Ebq 100-04). We examined bright-field images and used the fluorescence laser microscope to verify sample quality. This imaging combined transmitted light with fluorescence at 375 nm and auto-fluorescence at 477 nm, both of which matched the dye. Morphological analysis showed precipitation of the nanocap MIP at various stages of testing (filtrates from premixed, recycled, and freeze-dried nanocaps).

Raman spectroscopy and Fluorescence laser techniques

Real-time Fluorescence confocal imaging of the bionanocomposite in dissolution media was performed using a Confocal Laser Scanning Microscope (CLSM) (Zeiss, LSM 70) with Scan 2

and a 20x objective, in Airy scan and live sample mode. The samples at a depth of 80 nm were excited and scanned with a continuous laser. Images were captured utilizing a custom Zeiss microscope.

For our analysis, we used Raman microscopy with a Raman Microscope to visualize chemical properties and examine morphological changes in MIP nanocapsules during assembly—mapping the xy plane using a 514 nm laser and collecting spectra. We employed Franz's diffusion cell to measure the migration of substances in PBS solution within two compartments, collecting samples at predetermined intervals and filtering 200 µL of supernatant.

A nanoprobe analysis of *MIP nanocapsule-based 3D printing*

The topography of the filtrate nanosuspension of MIP nanocapsules was analyzed after casting onto glass or gold electrodes and air-drying. The remaining biocomposite was then scanned in non-contact mode at 1 Hz using a Flex AFM from Nanosurf, revealing details of the nanocapsules for 3D printable injectable drug delivery. The analysis of the samples included Infrared Spectroscopy (FT-IR) using FT-IR spectra (Perkin, USA) of the formulated MIP nanocapsules obtained by blending at low, medium, and high CBD concentrations (data not present). X-ray and SEM imaging of enzyme-treated nanocapsules with biocomposites suggest the potential for controlled assembly within cellulose pores, as shown in X-ray mapping images (Thermo Fisher Scientific, MA, USA).

We attained atomic-scale resolution with X-ray line-scan mapping, analyzing excipients and MIP nanocapsules using an X-ray microscope (XGT-5200WR, Scientific, Tokyo, Japan). Bonding energy was measured on nanocapsules and a pre-mixed MIP solid before and after hydration at 60 °C. Amino acid analysis of a donor-premixed nanocapsule remaining in the donor compartment after 7 days of diffusion was performed and compared with a sample from the receiving phase of the pooled filtrate.

3. Results

3.1. Characterization of MIP in Naocapsules

The self-assembled microstructure of the nanocap MIP on the membrane showcases the fabrication of biocomposite nanolayering with eco-friendly materials by creating nanoscale layers, and nanocapsules. Using CLSM, Figure 1 shows four-dimensional images depicting the real-time assembly of biocomposite particles and the distribution of nanocapsule channels, along with

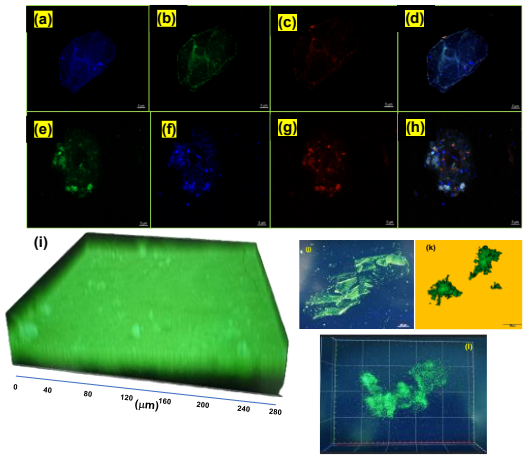

Figure 1. (a-c, e-g) 4D images of biocomposite particles across different fluorescence channels and (d, h) merged images of individual MIPs in nanocapsules. (i) The nanocap MIP's self-assembled microstructure, on a nanolayer, and (j-l) CLSM and image capture analysis.

fluorescence emission images of individualized nanocapsules at target objects and 488 nm fluorescence channels at 400-450 nm, 500-550 nm, and 470-720 nm.

3.2 In vitro drug release of the MIP in nanocapsules

In our controlled-release experiments, we observed greater controlled release of CBD from in-situ-loaded CBD. In Figure 2, the in vitro release of CBD from the MIP system in nanocapsules with different CBD concentrations was assessed across the model membrane. It aims to determine the diffusion coefficient (D_m) of CBD, particularly at high loadings (see Figure 2c and 2d). The enhanced permeability of CBD is attributed to the polymer matrix and the antibody/insulin complex, which facilitates effective membrane diffusion.

Higher D_m indicates a loosened water-bound nanolayer. After 24 hours, consistent drug release patterns suggest a partition mechanism. Increased CBD concentrations enhance binding in the polymer matrix, reducing release rates. Reproducibility in drug release was achieved, with insignificant D_m ($p>0.05$), supporting a strong partitioning mechanism for the antibody-insulin complex.

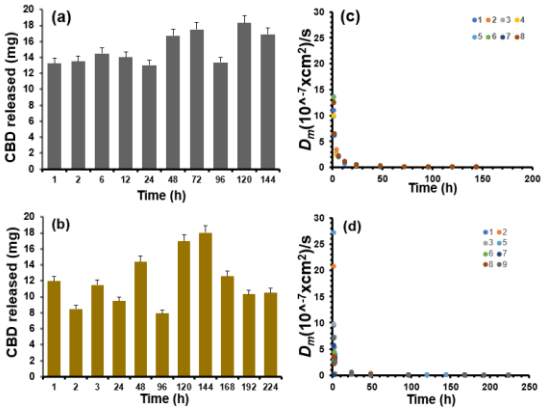

Figure 2. The reproducibility of in vitro CBD release from MIPs in nanocapsules: 1:1 (a) and 1:3 (b) of MIP in nanocapsules in the PCL-T oily gel. (c) and (d) the diffusion coefficient (D_m) of CBD in the high-loading biocomposite MIP. Eight replications were conducted (two independent runs).

Raman peaks corresponding to CBD concentrations of 20 mg and 200 mg were observed at 354, 512, 1037, 1288 cm^{-1}, and 1862 cm^{-1} (see Figure 3a-d) with the broad peaks observed when PCL-T was excluded (Figure 3e-f). The slight variations in these peaks indicate hydrogen-bonding interactions between the functional monomer and CBD in the biocomposite during the uptake.

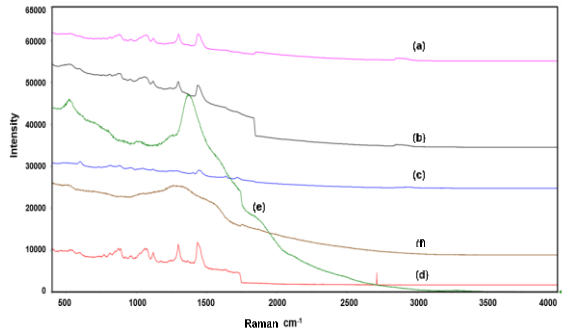

Figure 3. The residual biocomposite nanocapsule overlay on the natural cellulose fibrous membrane after 7 days, from various processing steps. (a) and (b) the customized CBD formulation across different batches; (c) low CBD concentration loaded in the premixed MIP; (d) higher CBD concentration loaded in the premixed MIP; (e) a pre-mixed MIP without PCL-T on the cellulose; and (f) suspension filtrates in buffer solution.

3.3 AFM and X-Ray Fluorescence mapping spectra

AFM imaging and XRF reveal the recycling of MIP nanocapsules and the selective removal of proteins during membrane exchange. The hydrated gel layer increases material thickness, affecting atomic dispersion on the nanocapsule surfaces. Unlike customized formulations, AFM images show distinct interparticle interactions rather than isolated charged particles (see Figure 4a and 4c, top panel). This process excludes dopamine (DA) and ligand interactions; in the absence of mono- and divalent ions, the electrolyte is mainly monovalent. Adding DA enhances the interaction between divalent ions and charged particles, as shown in the bottom panel of Figure 4c. Wang et al.[8] highlighted the significance of electrostatic solvation forces arising from molecular interactions near charged surfaces in the electrolyte. Our HSA-MIP carrier membranes play a vital role in substance transport, leading to atomic distribution on nanocapsule surfaces, with strong interactions observed in high-CBD formulations.

Nanocapsules demonstrate stability across a broad pH range and maintain consistent atomic arrangements. Interactions between calcium and chloride suggest that crystalline drugs may impede biodegradation. Interfacial ions optimize the interactions within biocomposite nanolayers. XRF microscopy indicates that phosphorus-calcium interactions enhance the stability of the antibody's fusion protein. Additionally, high-CBD formulations yield isolated charged particles, while modified MIPs facilitate improved enzyme immobilization. Combining MIP with PCL-T, rather than using the oily gel of the filtrate, shows that soluble materials and additives enhance water activity and interparticulate interactions in both the dried and hydrated forms by incorporating PCL-T, and that these interactions are further enhanced in the presence of electrolytes, as explained by the interfacial solvent structure.

Precise mass measurements confirmed target mass and proton exchange at m/z 315+H+ during storage, recycling, and freeze-drying, with ESI detecting m/z 315+H^+, $C_{21}H_{30}O_2(M+2H)^+$, and $C_{21}H_{30}O_2(M+3H)^+$. The ratios for main components and dimerized peptides remained steady, indicating consistent CBD-to-antibody ratios. Fluctuations in CBD diastereomers during recycling suggested potential destabilization at lower CBD levels, especially during ligand-modifier incubation. CBD likely interacts with a 33 Å pore during capsule formation, with minimal effect on protein concentration. This monomer's self-association improves the drug's solubility and the protein's stability, with the resulting complex remaining stable for 6 months at room temperature.

3.4 The evaluation of surface interaction

Raman mapping spectroscopy was used to track payloads in MIP nanocapsules during membrane passage (Figure 5a). The dissociation of the cholyl-methacrylated ester within the imprints of the protein template improved protein diffusion and lysozyme release, as evidenced by specific Raman peaks. FLT analysis indicated that CBD loading affects nanoparticle behavior and protein mobility (Figure 5b). Imaging (Figure 5c) revealed drug release changes influenced by various factors. Drug-protein interactions were more soluble at lower PCL-T gel concentrations, highlighting the effect of material composition on protein integrity under fluctuations in fluid flow and osmotic pressure within the interfacial solvent structure.[9] Increased imprint-binding sites enhanced material assembly and permeability, while smaller aggregates created transport barriers, facilitating the controlled uptake of the mAb-fusion protein and peptide drug. High-CBD nanocapsules, measuring less than 150 micrometers, showed efficient drug release and were suitable for injection through a 20-gauge needle.

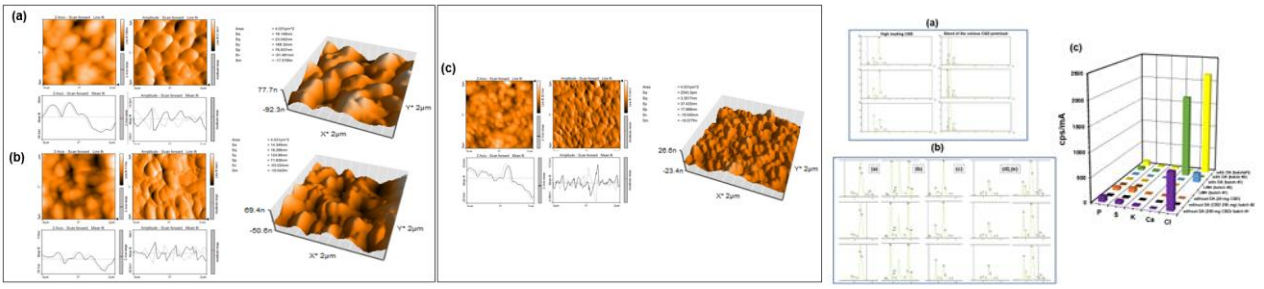

Figure 4. (Top) AFM images of air-dried (a) and hydrated (b) samples on a cellulose membrane demonstrate that nanocapsules contract more than they expand along the y and z axes, with (c) showing filtrate from the blend of CBD premixes (or LMH). (Bottom) (a) The X-ray spectrum; (b) The nanocapsules are presented as dried solids (a), liquids from the feed system (b), and recycling filtrate (d) and (e) during hydration and dehydration at 60 °C, respectively, and (c)—the plot of the atomic binding energies of elements on the MIP biocomposite nanolayer at different stages.

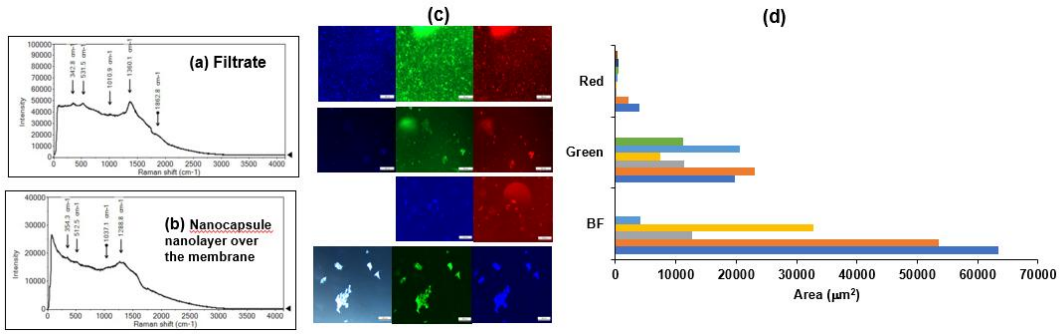

Figure 5. (a),(b) Raman mapping spectra of the premixed MIP within PCL-T oily gel across different fractions, (c) The FLT images of the residual protein phase and the nanocapsule suspension containing 200 mg of CBD. (d) An area plot of particles in Bright Field.

3.5 Relationship between surface-to-volume ratios and charge integrity, protein integrity, and payload encapsulation

Advanced imaging provided critical insights into drug dissolution and protein stability, influencing size parameters (Figure 6(i)). Variations in surface-to-volume ratios (SVRs) led to adjustments in mean population confidence intervals to 23.13% (±1.08%), 64.82% (±8.61%), and 45.19% (±12.36%). Differences in recycling methods underscore the importance of charge stability and payload encapsulation. During the recycling process, the amino acid content decreased, with nanocap MIPs showing elevated glycine levels and a complete absence of phenylalanine. The prominence of glycine and tyrosine is essential for optimal metabolic processes. Lyophilization significantly enhanced protein stability and solubility. We effectively employed a machine learning model to analyze the dynamics of CBD loading. At the same time, the PAT decisively revealed differences in amino acid content during bionanofiltration in enzyme-rich environments, as supported by previous work.[10]

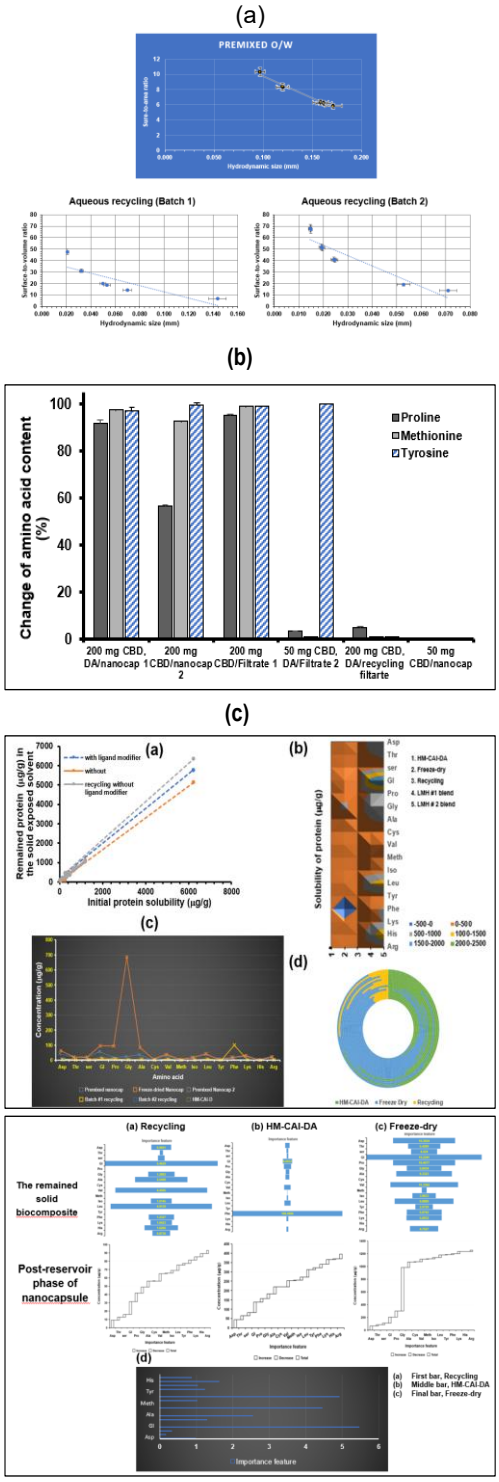

Figure 6. (a) The effect of surface area-to-volume ratio across different batches during aqueous recycling. (b) (a-d) Changes in amino acid contents extracted from filtrates of recycled nanocapsules, with and without modified ligands and freeze-dried variants for two types of CBD premix (50 mg & 200 mg). (c) The critical feature analysis predicts differentiation at both the residual solid biocomposite and the post-reservoir phase of the nanocapsules. (d) The critical feature analysis identifies the target clusters.

Enzyme-incubated dried nanocapsules remarkably improved particle capture and imaging, facilitating the successful immobilization of biomacromolecules. Furthermore, lyophilization increased the concentration of zwitterionic glycine ions, thereby contributing to robust protein stabilization, precise pH regulation, and enhanced solubility and release kinetics (see Figure 6).

Tyrosine's hydrophilicity increased with higher CBD loading, resulting in enhanced solubility. Recycled samples without ligands demonstrated greater amino acid adsorption ($p=0.048$) and a consistent decline in amino acid content throughout the recycling process, with a higher amino acid adsorption rate ($p>0.05$).

Conclusion

We prepared a biocomposite that integrates nanoscale molecularly imprinted polymers (MIPs) with eco-friendly nanocapsules, enabling 3D-printable, injectable drug delivery. The nanocapsules demonstrate stability across ions, electrolytes, and salts at a range of pH levels and enhance the activity of fusion proteins. High-CBD formulations generate charged particles, while modified MIPs improve enzyme immobilization. The combination of MIP with PCL-T enhances water activity and interparticulate interactions. This research aims to advance sustainable biopharmaceuticals and nanotheranostic systems.

Acknowledgements

We thank the Department of Pharmaceutical Chemistry, Prince of Songkla University, for their financial support for the FF on “Polymyxin B formulation” (PHA6801059S). We also acknowledge Mr. Naruedom Tangthong, Dr. Kishna Mahesh, Miss Apinya Sukulrut for their AFM work, and Miss Pojchanad Putburee at OSIT, PSU, and Zeiss Technologies, Thailand.

References

1. Trömstedt, A.A.; Pasupuleti, M.; Schmidtchen, A.; Malmsten, M., Evaluation of Strategies for Improving Proteolytic Resistance of Antimicrobial Peptides by Using Variants of EFK17, an Internal Segment of LL-37. *Antimicrob. Agents Chemother.* **2008** *24*;53(2), 593-602.
2. Lui, Q.; Wang, H.; Shi, X.; Wang, Z.-G.; Ding, B., Self-Assembled DNA/peptide-based Nanoparticle exhibiting Synergistic

Enzymatic Activity, ACS Nano **2017**, *11*, 7251-7258.
3. Do Carmo, J.P.; Phyo, Y.Z.; Palmeira, A.; Tiritan, M.E.; Afonso, C.; Kijjoa, A., Enantioseparation, Recognition Mechanisms and Binding of Xanthones on Human Serum Albumin by Liquid Chromatography. *Bioanalysis* **2019**, *11*, 1255-1274.
4. Esmaeilzadeh, S.; Valizadeh, H.; Zakeri-Milani, P., The effects of pH, Temperature, and Protein Concentration on the In Vitro Binding of Flutamide to Human Serum Albumin. *Pharm. Dev. Technol.* **2017**, *22*, 982-991.
5. Teixeira, S.P.B.; Reis, R.L.; Peppas, N.A.; Gomes, M.A.; Domingues, R.M.A., Epitope-Imprinted Polymers: Design Principles of Synthetic Binding Partners for Natural Biomacromolecule. *Sci. Adv.* **2021**, 29;*7(44)*, eabi9884.
6. Vlad, R.-A.; Pintea, A.; Antonoaea, P.; Redai, E.-M.; Bîrsan, M.; Hancu G.; Farczádi, L.; et. al., Exploring the Interconnected Properties of Cannabidiol Suspensions and Orodisperible Films. *Sci. Rep.***2025**, *15*, 201564 (1-21).
7. Shibata, H.; Harazono, A.; Kiyoshi, M.; Ishii-Watabe, A., Quantitative Evaluation of Insoluble Particulate Matters in Therapeutic Protein Injections Using Light Obscuration and Flow Imaging Methods. *J. Pharm. Sci.* **2022**, *111*:, 648-654.
8. Wang, S.; Walker-Gibbons, R.; Watkin, B.; Lin, B.; Krishnan, M., Chemical Control of Colloid Self-assembly Driven by the Electrosolvation Force. *Nature Comm.* **2025** *16*, *2872*, 1-16.
9. Cui Y.; Chung T.-S., Pharmaceutical Concentration using Organic Solvent forward Osmosis for Solvent Recovery. *Nature Comm.* **2018***, 9,* 1-9.
10. Klontzas, M.E.; Veernardis, S. I.; Batsali, A.; Papadogiannis, F.; Panoskaltsis, N.; Mantalaris. A., Machine Learning and Metabolomics Predict Mesenchymal Stem Cell Osteogenic Differentiation in 2D and 3D Cultures. *J. Func. Biomaterial* **2024**, *15*, 367 (1-10).

Upcycling of Filter Cake to Biochar for Improving the Mechanical Properties of Cement Mortar

Muhammad Shahab[1], Kantipok Hamcumpai[2], Pitcha Jongvivatsakul[2], Jariyaporn Sangkaworn[1], Assadawoot Srikhaow[1], Chitiphon Chuaicham[1*]
[1]*Department of Environmental and Sustainable Engineering, Faculty of Engineering, Chulalongkorn University, Bangkok 10330, Thailand*
[2]*Department of Civil Engineering, Faculty of Engineering, Chulalongkorn University, Bangkok 10330, Thailand*
**E-mail: chitiphon.c@chula.ac.th*

Abstract:

Sugarcane filter cake is a high-volume byproduct of sugar processing that presents challenges for effective management, yet offers potential for advanced value-added applications. This work investigated the conversion of sugarcane filter cake into biochar for application as a cement additive, aiming to exploit its high silica content to improve mechanical performance. Cement mortar samples were cast with and without the addition of filter cake biochar (FCB) at 0, 2.5, 5, 7.5, and 10% by weight of cement and tested for compressive strength. Compared with mortar without biochar, the addition of 7.5% w/w FCB to cement yields the highest compressive strength (45.3 MPa), representing a 58% improvement over the control mix (28.7 MPa) at 28 days of curing. These improvements can be attributed to the micro-filler effect of biochar, which refines pores, densifies the matrix, and potentially enhances hydration and internal curing. The XRD and TGA results of cement and biochar pastes revealed enhanced C-S-H formation when FCB was added to mortar. It was observed that biochar might enhance the pozzolonic reaction, potentially improving compressive strength. Thus, this work demonstrates that sugarcane filter-cake biochar could be a promising solution for managing sugarcane filter-cake waste, thereby enhancing both the mechanical performance and sustainability of cement-based materials.

1. Introduction

Thailand, a leading agricultural hub in Southeast Asia, generates around 34 million tons of agricultural waste annually, presenting both environmental challenges and opportunities for sustainable reuse.[1] The sugarcane industry, central to Thailand's economy, generates large volumes of by-products such as bagasse ash (SBA) and filter cake. SBA, rich in silica, has been studied as a supplementary cementitious material that enhances concrete performance while reducing CO_2 emissions.[2] Filter cake, however, is a nutrient-rich sludge produced in massive quantities (3-5 tons per 100 tons of cane processed) that often ends up in landfills due to limited reuse capacity, causing leachate contamination and greenhouse gas emissions.[3] Addressing these waste management issues is vital for Thailand's climate-smart agriculture strategy, which emphasises lowering emissions, enhancing resilience, and driving sustainable growth.[1]

A promising pathway for managing agro-industrial residues is the conversion of such wastes into biochar. Filter cake biochar, produced through controlled pyrolysis, transforms wet and odorous sugarcane filter cake into a porous, carbon-rich material suitable for cementitious applications. This biochar can enhance mortar hydration, refine microstructure, reduce permeability, and act as a long-term carbon sink, contributing to more sustainable construction practices.[4]

Sugarcane filter cake biochar (FCB) exhibits distinct compositional and performance advantages compared to other biomass-derived biochars. Unlike rice husk biochar (RHB), which is primarily silica-rich (70-80 wt% SiO_2), filter cake contains a more balanced composition with significant quantities of both silica (57.5 wt% SiO_2) and alumina (11.5 wt% Al_2O_3), combined with moderate calcium oxide content (11.3 wt% CaO). This multi-oxide composition provides additional cementitious potential compared to single-phase biochars.[5] Filter cake biochar retains valuable macropores (>1 μm) that enhance water retention and internal curing capacity more effectively than rice husk biochar, which produces predominantly micropores (<2 nm).[6] Sugarcane bagasse biochar, while comparable in carbon content, exhibits higher silica reactivity in filter cake biochar due to the nutrient-rich sludge composition, which provides additional catalytic species for enhanced pozzolanic activity.[5] The combination of high reactive silica, alumina, and macroporous structure makes filter cake biochar

uniquely suited for cement applications, offering both mechanical enhancement and superior waste valorization compared to other agricultural waste-derived biochars.[4] By valorizing sugarcane filter cake into biochar, it is possible to reduce environmental burdens, promote circular economy practices, and support the UN Sustainable Development Goals. This study investigates the effects of incorporating different percentages of filter cake biochar as a cement additive, focusing on workability, setting time, strength development, and microstructural properties compared with a conventional control mix.

2. Materials and Methods

2.1 Materials and biochar production

Filter cake (press mud) was collected from Chonburi Sugar Cooperative Company Limited (Chonburi) and was oven-dried at 105°C for 24 hours. The dried filter cake was converted to biochar by slow pyrolysis in a tube furnace (Chavachote, Tube50/1009P). Typically, 8 g of dried filter cake was placed in a crucible, transferred into the tube furnace, and thermally treated at a temperature of 500°C with a rate of 10 °C/min for 1.25 hours under a continuous nitrogen flow. The char was cooled under nitrogen to prevent oxidation, ground, sieved (mesh size < 75 µm) for uniformity, and stored in airtight containers for further use.

Hydraulic Cement (SCG, Type GU) was used as a binder in all mixes. The fine aggregates used for all mixtures were natural river sand with a fineness modulus of 2.85 and specific gravity of 2.66, which were prepared in the Standard Surface-Dry (SSD) condition. Tap water was used for mixing mortar ingredients.

2.2 Mortar Mix design and preparation

To prepare the mortar specimens, a standard Hobart mixer was used following ASTM C305-12.[19] The control mortar mix and biochar-added mixes were prepared in accordance with ASTM C109[16], as illustrated in Table 1 (W/C = Water-to-cement ratio and S/C = Sand-to-cement ratio). First, cement, sand, and filter cake biochar (FCB) were dry-mixed for 5 minutes. Then, water was gradually added, and the mixture was blended for another 5 minutes to obtain a uniform consistency. Filter cake biochar was incorporated at 0% (CM), 2.5% (FCB2.5), 5% (FCB5), 7.5% (FCB7.5), and 10% (FCB10) by weight of cement, as suggested by previous studies.[9,10] After mixing, the mortar was cast into moulds (50 × 50 × 50 mm³), covered with plastic sheets to prevent evaporation, and cured at 20 ± 4 °C until testing.

Table 1. Mix design

Mix ID	Cement (kg)	Water (kg)	Sand (kg)	FCB (g)	W/C	S/C
CM	0.8	0.4	2.2	0	0.55	2.75
FCB2.5	0.8	0.4	2.2	20	0.55	2.75
FCB5	0.8	0.4	2.2	40	0.55	2.75
FCB7.5	0.8	0.4	2.2	60	0.55	2.75
FCB10	0.8	0.4	2.2	80	0.55	2.75

2.3 Testing program

In this study, the effect of filter cake biochar (FCB) addition on the mechanical performance of cement mortar was investigated through tests on fresh and hardened properties. The workability of fresh mortar was evaluated following ASTM C1437 (2020),[17] and the compressive strength was tested according to ASTM C109 (2020)[16] at 28 days.

2.4 Characterization

The crystalline phases of cured control and biochar cement pastes were determined using X-ray diffraction (XRD, BRUKER, D2 PHASER). The 7, 14, and 28-day cured cement paste samples were dried in an oven for 1 hour at 105°C and then ground in a hammer mill to a fine powder form for analysis. The patterns were collected at a 2θ angle of 0.5°-80°.

Similarly, elemental analysis of raw filter cake and filter cake biochar was determined using wavelength dispersive X-ray fluorescence (WDXRF) spectrometry (BRUKER, S8 TIGER).

3. Results

3.1 Chemical properties of samples

Figure 1 illustrates the XRD patterns of FCB. Dominant peaks at 2θ = 21.2° and 26.6° are indexed to α-quartz (SiO_2, JCPDS 46-1045), while minor peaks at 36.9° and 42.7° correspond to CaO (JCPDS 37-1497), and peaks at 29.8°, 39.9°, and 60.2° match calcite, $CaCO_3$ (JCPDS 05-0586). Peak assignments follow prior literature using ICDD/JCPDS[20] standards. Similarly, the XRF results of raw filter cake and filter cake biochar are in agreement with the XRD results, showing a high amount of SiO_2, followed by Al_2O_3 and CaO, which are the main constituents of filter cake as shown in Table 2. The increase in SiO_2 from 51.1% to 57.5% and Al_2O_3 from 9.23% to 11.5% in filter cake biochar after pyrolysis is primarily due to the

loss of moisture and volatile organics, which concentrates the non-volatile minerals.[11] In contrast, the CaO content decreases from 18% to 11.3% because calcium carbonates decompose, releasing CO_2 during pyrolysis.[11]

The results from XRD and XRF suggested that the presence of Silica in FCB can potentially enhance cement hydration and can potentially act as a pozzolan that enhances C-S-H formation, refining pores, and improving early and long-term strength.[4,21]

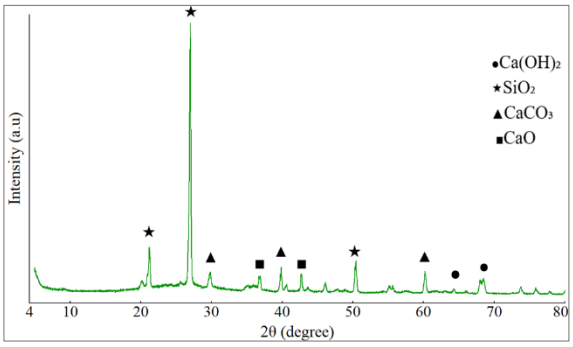

Figure 1. XRD patterns of filter cake biochar.

Table 2. Elemental composition of raw filter cake and filter cake biochar by XRF analysis.

Oxide	Raw filter cake	Filter cake biochar
SiO_2	51.1 %	57.5 %
Al_2O_3	9.23 %	11.5 %
CaO	18.0 %	11.3 %
Fe_2O_3	9.43 %	8.32 %
P_2O_5	4.22 %	4.06 %
K_2O	2.81 %	2.46 %

3.2 Workability of mortar

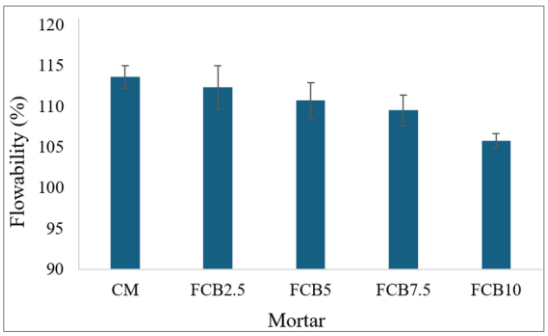

Figure 2. Workability of all mortars.

As illustrated in Figure 2, the workability of CM was 113.6%. Noticeably, the workability slightly decreased after the incorporation of filter cake biochar (FCB) in the mortar, with decreases of approximately 1.2%, 2.5%, 3.7%, and 7.6% for FCB2.5, FCB5, FCB7.5, and FCB10, respectively, compared to the control mix. The reduced workability of biochar-modified mixes was in the normal range (105%-115%)[17] for mortar, except for the FCB10 sample. This reduction resulted from the porous and high-surface-area nature of FCB, which can absorb mixing water and contribute to a stiffer fresh mortar.[4]

3.3 Mechanical properties

Figure 3 shows that compressive strength increased with biochar addition up to 7.5% but declined at higher levels. Compared to the control mix with a compressive strength of 28.7 MPa, the addition of 2.5%, 5%, 7.5%, and 10% biochar to the mortar improved the compressive strength by 32%, 64%, 58%, and 45%, respectively. The strength improvement in biochar-modified mortars is mainly due to the micro-filler and internal curing effects of biochar.[12] Fine particles enhance matrix packing and stress transfer, while biochar's porous structure absorbs and later releases water, promoting C-S-H and CH formation and densifying the matrix.[2] However, at higher dosages, excessive cement dilution reduces hydration products, leading to decreased strength.[13]

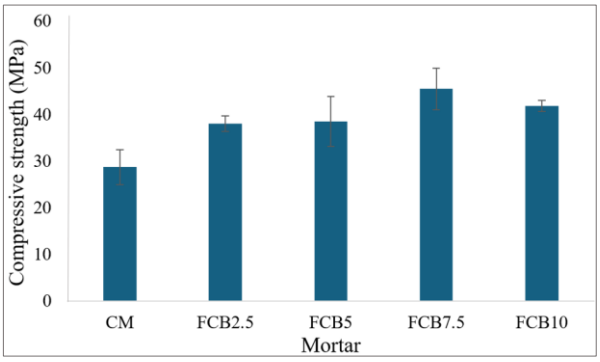

Figure 3. Compressive strength of all mortars.

3.4 XRD analysis of control and 7.5% biochar pastes at different ages

The consumption of $Ca(OH)_2$ (present in cement) influences the formation of C-S-H. The ratios of XRD peak intensities of portlandite (2θ=18.13)/Alite (2θ=29.55) (I_P/I_A) at different ageing times (7, 14 and 28 days) of the control mix and FCB7.5 sample were calculated to elucidate the C-S-H formation due to pozzolonic reaction during curing. The XRD results showed a clear decrease in I_P/I_A ratios in biochar-incorporated cement pastes compared to the control at 7, 14, and 28 days, as shown in Figures 4 and 5. The

reduction in I_P/I_A ratio indicated enhanced reaction of $Ca(OH)_2$ with the amorphous silica present in the biochar, promoting more C-S-H formation in the biochar sample.[9]

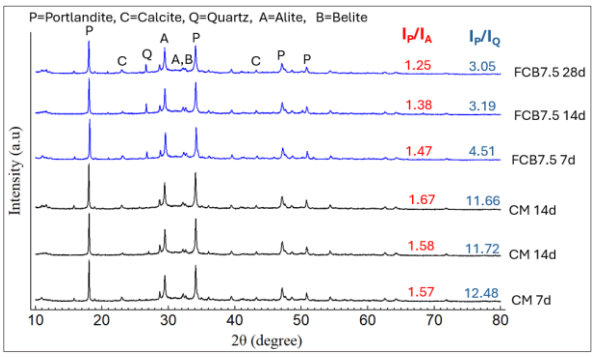

Figure 4. XRD patterns of CM and FCB7.5 pastes at different ages (7, 14 and 28 days).

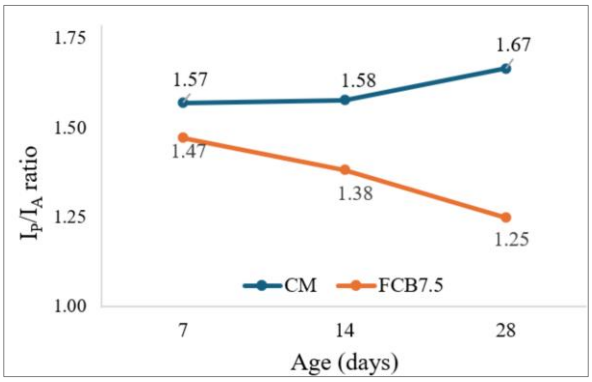

Figure 5. XRD peak intensity ratio of portlandite /Alite (I_P/I_A) of CM and FCB7.5 at different ages (7, 14 and 28 days).

3.5. TGA Analysis

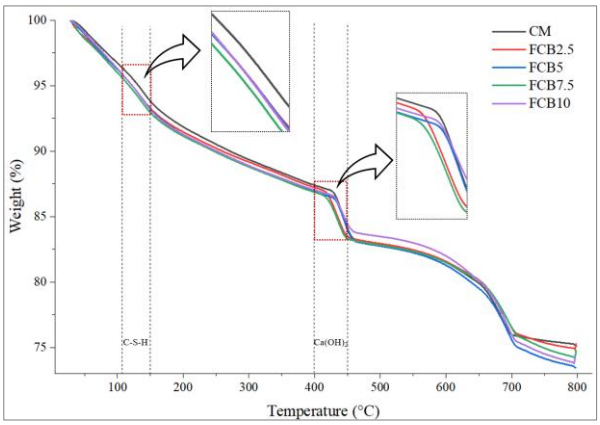

Figure 3. Thermogravimetry analysis of biochar cement and control cement pastes.

Thermogravimetric analysis provided quantitative confirmation of enhanced hydration product formation after 56 days of curing of the samples, illustrated in Figure 7. Analysis of mass loss in the 110-150°C range (C-S-H dehydration) revealed that FCB7.5 samples exhibited the highest mass loss in chemically bound water content (7.97%) compared to the CM (6.83%). Furthermore, the decreased portlandite decomposition in the 400-500°C range for all biochar samples (mass loss of 16.2% for FCB7.5 compared to the CM) confirmed consumption of $Ca(OH)_2$, indicating more C-S-H formation through the biochar's pozzolanic reaction.

Conclusion

The filter cake biochar (FCB) was successfully applied as a cement additive to enhance the compressive strength of mortar by 58% compared to the control mix at an optimal level of 7.5% by weight. The XRD and XRF results indicated that FCB was rich in SiO_2 (57.5 wt%) and Al_2O_3 (11.5 wt%), suggesting that it can potentially enhance hydration reactions and exhibit pozzolanic activity. The physical property test of cement mortar showed that workability decreased with increasing FCB content due to its high surface area and water absorption capacity. Furthermore, XRD analysis of cement pastes at different ageing times confirmed that SiO_2 in FCB enhanced cement hydration and promoted C-S-H formation. Thermogravimetric analysis quantitatively confirmed increased C-S-H formation (a mass loss of 7.97% for FCB7.5 vs. 6.83% for the control in the 110-150°C range) and high portlandite consumption (in the range of 400-500°C), validating the pozzolanic reactivity of silica. This work demonstrates that converting raw filter cake to biochar is important for its effective use in cementitious materials, contributing not only to enhanced mortar performance but also to sustainable waste management, circular economy practices, and reduction of environmental burdens. Further analyses of microstructure, chemical functional groups, porosity, and thermal resistance are currently being conducted to determine the physico-chemical, surface, and thermal properties of the cement paste. Future work will focus on durability-related tests, including water absorption, chloride penetration, carbonation resistance, and sulfate resistance, to assess long-term performance.

Acknowledgement

The authors gratefully acknowledge the support of Chulalongkorn Engineering's promoting research grant for funding this research.

References

1. Rodriguez Espinosa, P. F.; Chidthaisong, A.; Cha-un, N.; Towprayoon, S., Thailand's climate-smart agriculture strategy: Pathways to sustainable development. *Sustainability* **2023,** *15*, 5042.
2. Xu, W.; Lo, T. Y.; Memon, S. A., Microstructure and reactivity of sugarcane bagasse ash in cementitious system. *Construction and Building Materials* **2018,** *187*, 974-983.
3. Gbadeyan, T. A.; Adewuyi, B. O.; Sulaiman, K. A.; Ibrahim, A. O., Environmental implications of sugarcane press mud disposal and valorisation potential. *Journal of Materials and Minerals Management* **2024,** *14* (2), 117-126.
4. Gupta, S.; Kua, H. W.; Dai Pang, S., Biochar as a partial cement replacement material for developing sustainable concrete: Strength, hydration and pore structure studies. *Construction and Building Materials* **2020,** *243*, 118223.
5. Choudhury, R.; Swain, S.; Panda, B. B.; Pradhan, C., Change in nutrient composition of biochar from rice husk and sugarcane bagasse at varying pyrolysis temperatures. *Journal of Agricultural Engineering* **2022,** *53* (4), 1-12.
6. Muzyka, R.; Misztal, E.; Hrabak, J.; Banks, S. W.; Sajdak, M., Various biomass pyrolysis conditions influence the porosity and pore size distribution of biochar. *Energy* **2023,** *263* (Part E).
7. Silva, S. H. G.; Ribeiro, B. T.; Guerra, M. B. B.; Carvalho, H. W. P.; Lopes, G.; et al., pXRF in tropical soils: Methodology, applications, achievements and challenges. *Advances in Agronomy* **2021,** *167*, 1-62.
8. Rydberg, J., Wavelength dispersive X-ray fluorescence spectroscopy as a fast, non-destructive and cost-effective analytical method for determining the geochemical composition of small loose-powder sediment samples. *Journal of Paleolimnology* **2014,** *52*, 265-276.
9. Jiang, X.; Li, B.; Guo, J., Study on the properties of different biochar to cement paste. *IOP Conference Series: Earth and Environmental Science* **2020,** *526* (1).
10. Dixit, A.; Gupta, S.; Pang, S. D.; Kua, H. W., Waste valorisation using biochar for cement replacement and internal curing in ultra-high performance concrete. *Journal of Cleaner Production* **2019,** *238*, 117876.
11. Ofori-Boadu, A. N.; Bryant, D.; Bock-Hyeng, C.; Assefa, Z.; Aryeetey, F.; Munkaila, S.; Fini, E., Physiochemical characterization of agricultural waste biochars for partial cement replacement. *International Journal of Building Pathology and Adaptation* **2022,** *40* (4), 569-586.
12. Ainomugisha, S.; Matovu, M. J.; Manga, M., Influence mechanisms of silica nanoparticles' property enhancement in cementitious materials and their green synthesis: A critical review. *Case Studies in Construction Materials* **2024,** *20*, e03372.
13. Gupta, S.; Kua, H. W.; Low, C. Y., Use of biochar as carbon sequestering additive in cement mortar. *Cement and Concrete Composites* **2018,** *87*, 110-129.
14. ASTM International. *Standard Specification for Portland Cement*; ASTM C150/C150M; ASTM International: West Conshohocken, PA, **2023.**
15. ASTM International. *Standard Specification for Concrete Aggregates*; ASTM C33/C33M; ASTM International: West Conshohocken, PA, **2023.**
16. ASTM International. *Standard Test Method for Compressive Strength of Hydraulic Cement Mortars (Using 50-mm Cube Specimens)*; ASTM C109/C109M; ASTM International: West Conshohocken, PA, **2016.**
17. ASTM International. *Standard Test Method for Flow of Hydraulic Cement Mortar*; ASTM C1437; ASTM International: West Conshohocken, PA, **2007.**
18. ASTM International. *Standard Test Method for Density, Absorption, and Voids in Hardened Concrete*; ASTM C642; ASTM International: West Conshohocken, PA, **2013.**
19. ASTM International. *Standard Practice for Mixing of Hydraulic Cement Pastes and Mortars*; ASTM C305-12; ASTM International: West Conshohocken, PA, **2012.**
20. (ICDD). *Powder Diffraction File*; PDF-2 Release 2026; ICDD: Newtown Square, PA, **2026.**
21. Malaiškienė, J.; Vaičienė, M., The influence of silica fly ash and wood bottom ash on cement hydration and durability of concrete. *Materials* **2024,** *17* (16), 4031.

Enhancing the Processability of Biomass-Based Polyester by Polymer Blending

Tassakarn Nantinee[1], Masayuki Yamaguchi[1*]
[1]*Japan Advanced Institute of Science and Technology, Japan*
[*]*E-mail: m_yama@jaist.ac.jp*

Abstract:

The transition to a low-carbon economy requires not only the capture and storage of CO_2 but also the development of carbon-efficient materials and processing technologies that minimize life-cycle emissions. Poly(3-hydroxybutyrate-co-3-hydroxyhexanoate) (PHBHHx), a biodegradable polyester derived from renewable feedstocks, offers considerable environmental advantages. However, poor processability due to its high melt viscosity should be modified to widen the applications. In this study, the flowability of PHBHHx was improved through melt blending with polycaprolactone (PCL), another biodegradable polyester, and triethyl citrate (TEC) as a bio-based compound. Rheological analysis demonstrated a significant reduction in melt viscosity, particularly under high shear conditions, upon the addition of PCL. This effect was attributed to interfacial slippage between phases. It was also found that TEC showed good miscibility with PHBHHx and acted as a plasticizer.

1. Introduction

Poly(3-hydroxybutyrate-co-3-hydroxyhexanoate) (PHBHHx) is a biodegradable plastic produced from bio-mass resources. Since it shows thermal degradation at high temperature, processing must be performed at relatively low temperature.[1,2] Therefore, viscosity is usually high, which may lead to difficulties at injection molding. Therefore, improving the flowability is often required. Adding a plasticizer is a well-known method to reduce the viscosity. Furthermore, the addition of an immiscible low-viscosity polymer is also an effective method.[3-12] However, appropriate plasticizers and immiscible polymers with low viscosity were not revealed for PHBHHx.

In this study, therefore, triethyl citrate (TEC) and polycaprolactone (PCL), both known as biodegradable materials, were employed to modify the rheological properties of PHBHHx. TEC is known to act as a plasticizer for poly(vinyl chloride) that is miscible with poly(3-hydroxybutyrate).[13,14] Furthermore, PCL is a commercially available bio-polyester having relatively low molecular weight.

2. Experimentals

2.1 Materials

The PHBHHx (Kaneka, Tokyo, Japan) contained 5.3 mol.% of 3-hydroxyhexanoate. The weight average molecular weight of PHBHHx was 600,000 (Da). The PCL (Daicel, Tokyo, Japan) used in this study had a weight-average molecular weight of 10,000 (Da). TEC (CITROFOL AI regular, Jungbunzlauer, Basel, Switzerland) was used after drying by molecular sieve.

2.2 Sample preparations

Mixing was performed using a 30 cc internal mixer (Labo-Plastmill; Toyo Seiki Seisaku-sho, Tokyo, Japan) at 160°C for 3 min. The weight contents of PCL or TEC were 0%, 5%, and 15%. After mixing, the samples were compression-molded into flat films using a compression-molding machine at 160°C for 3 min.

The films with a thickness of 1 mm were then cooled at 25°C using another compression-molding machine for 5 min.

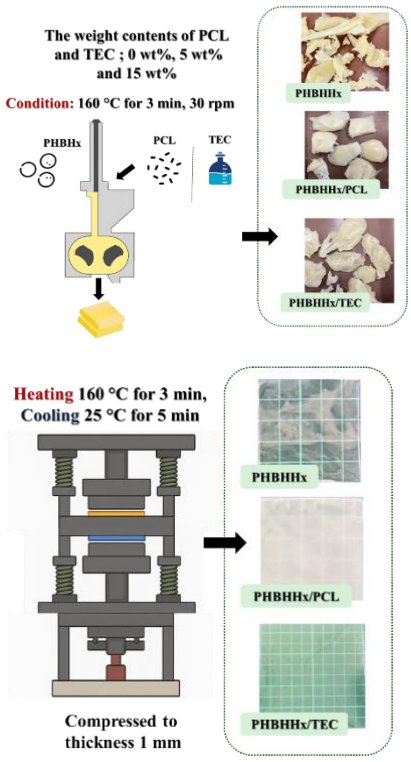

Figure 1. Preparation of the sample films; (top) mixing and (bottom) compression molding.

2.3 Measurements

Angular frequency dependence of oscillatory shear moduli in the molten state was evaluated by a

cone-and-plate rheometer (MCR 301; Anton Paar, Graz, Austria) with N_2 flow at 160°C. The cone angle was 2° and its diameter was 25 mm. The angular frequency ranged from 0.1 to 628.3 s^{-1}.

Blend morphology was observed using a scanning electron microscope (SEM, TM3030; Hitachi, Tokyo, Japan). The accelerating voltage was 15kV. After cutting, the sample was dipped in toluene to remove PCL dispersions. Before the observation, dried surface was sputter-coated with Pt–Pd.

A capillary rheometer (140SAS; Yasuda Seiki Seisakusyo, Nishinomiya, Japan) was employed to measure the shear viscosity at 160°C. A circular die with a diameter of 1 mm and a length of 10 mm was used.

3. Results & Discussion

3.1 Morphology of a blend

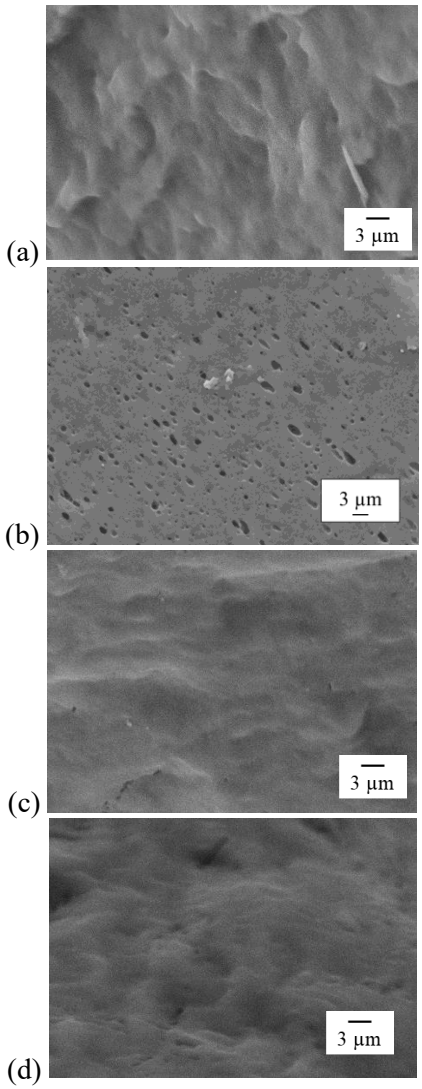

Figure 2. SEM image of (a) PHBHHx/PCL before removal of PCL, (b) PHBHHx/PCL after removal of PCL, (c) PHBHHx/TEC before removal of TEC and (d) PHBHHx/TEC after removal of TEC.

Morphology of PHBHHx/PCL was analyzed using SEM as shown in Figure 2. Since PCL was removed by solvent, the holes represent the PCL dispersions. It was found that PCL showed uniform distribution with an average diameter of 1.1 µm. Such structure was not detected in the blend with TEC.

3.2 Linear viscoelastic properties

Shear storage modulus G′ and loss modulus G″ at 160°C for all blends are plotted against the angular frequency ω in Figure 3. The contents of PCL and TEC were 0 and 15 wt%. Both G′ and G″ values of PHBHHx were higher than those of PHBHHx/PCL and PHBHHx/TEC. However, the G′ values in the low frequency region of PHBHHx/PCL were higher than those of pure PHBHHx. This was ascribed to the interfacial tension between PHBHHx and PCL phases. The G″ values of the blend with PCL were slightly higher than those of the blend with TEC in the wide frequency range. Furthermore, G′ values of PHBHHx/TEC monotonically decreased with decreasing frequency. It was suggested that TEC is miscible with PHBHHx, i.e., acts as a plasticizer.

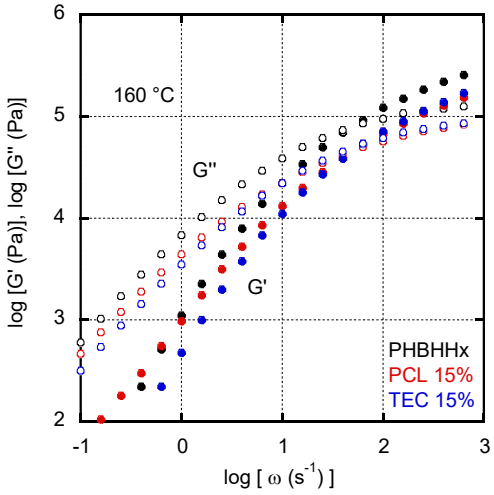

Figure 3. Angular frequency ω dependence of (closed symbols) shear storage modulus G′ and (open symbols) loss modulus G″ at 160ºC for PHBHHx, PHBHHx/PCL, and PHBHHx/TEC.

3.3 Steady-state shear viscosity

The shear viscosities of PHBHHx, PHBHHx/PCL, and PHBHHx/TEC were evaluated using the capillary rheometer at 160°C. The result is presented in Figure 4. It was found that both TEC and PCL reduced the shear viscosity of PHBHHx with an intense fraction of PCL. This must be interesting because G″ values of PHBHHx/TEC were lower than those of PHBHHx/PCL. In the case of PHBHHx/TEC, moreover, the shear viscosity in Figure 4 corresponded with the complex shear viscosity calculated from G′ and G″ in Figure 3.

This pronounced reduction in viscosity by the PCL addition must be attributed to the interfacial slippage. During flow, PCL dispersions must be deformed to the flow direction greatly because the shear viscosity was much lower than that of PHBHHx. Then the interfacial slippage occurs due to a thin thickness of interfacial area as illustrated in Figure 5, with an enlarged interfacial area.

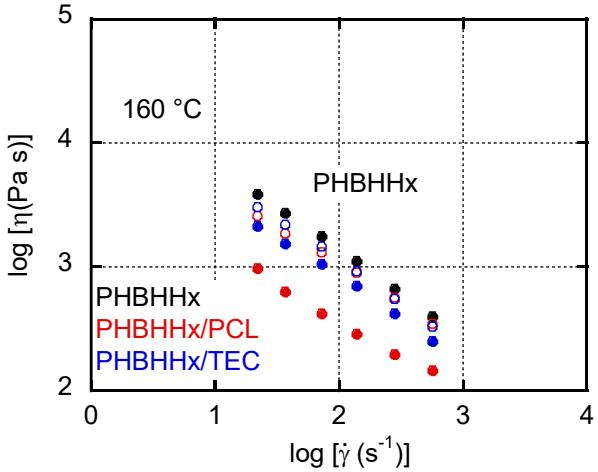

Figure 4. Flow curves at capillary extrusion for (black) PHBHHx, (red open circles) PHBHHx/PCL 5%, (red closed circles) PHBHHx/PCL 15%, (blue open circles) PHBHHx/TEC 5%, and (blue closed circles) PHBHHx/TEC 15%.

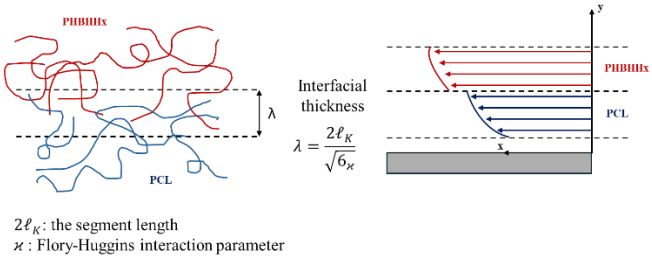

Figure 5. Schematic illustration of interfacial slippage mechanism in immiscible PHBHHx/PCL.

This mechanism was ordinally proposed by Zhao and Macosko[15-17] using multi-layered films. They showed significant slippage at polymer-polymer interfaces when the interfacial thickness is thin.

Because of the viscosity reduction, i.e., the decrease in shear stress, the melt fracture was mitigated. As shown in Figure 6, pure PHBHHx showed typical gross volumetric melt fracture originated from high elongational stress at die entrance.[18,19] After the addition of TEC or PCL, the surface of strands became smooth. This result indicates that the processability is improved by the blend technique.

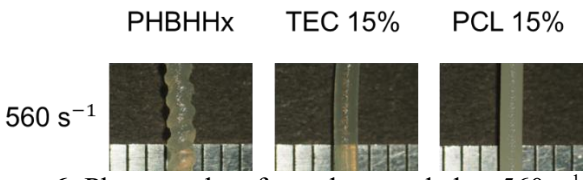

Figure 6. Photographs of stands extruded at 560 s^{-1} at 160°C.

Conclusion

This study shows that both miscible (TEC) and immiscible (PCL) blending effectively reduce the melt viscosity of PHBHHx, which improves its processability. These findings offer a scalable and energy-efficient method for processing of biodegradable polymers, supporting low-carbon material design and carbon capture, utilization, and storage (CCUS) objectives.

References

1. Lee, J.; Moriyama, K.; Hikima, Y.; Ohshima, M. J., Poly(3-hydroxybutyrate-co-3-hydroxyhexanoate) microcellular foams using a melt memory effect as bubble nucleation sites. *Appl. Polym. Sci.* **2023,** *140,* e54386.
2. Yu, L.; Xie, W.; Zhang, D.; Jin, X.; Wang, Y.; Liu, H.; Deng, L. ACS Omega 2021, 6, 2135–2146.
3. Farrag, Y.; Barral, L.; Gualillo, O.; Moncada, D.; Montero, B.; Rico, M.; Bouza, R., Effect of Different Plasticizers on Thermal, Crystalline, and Permeability Properties of Poly(3–hydroxybutyrate–co−3–hydroxyhexanoate) Films. *Polymers* **2022,** *14,* 3503.
4. Muratov, D. S.; Sakhabutdinova, I. M.; Kildeeva, N. R.; Khutoryanskiy, V. V. Polym. Sci., Ser. B 1999, 35, 357–364.
5. Watanabe, T.; Inoue, M.; Suzuki, T.; Yamamoto, H. J. Appl. Polym. Sci. 2020, 137, 49516.
6. Suzuki, T.; Yamamoto, H.; Inoue, M. Polymer 2019, 170, 135–141.
7. Wang, W.; Huang, Q.; Zhao, C.; Li, Y.; Jiang, X. Polym. Eng. Sci. 2021, 61, 1096–1103.
8. Kumar, P.; Zhang, X.; Zhao, Y.; Wang, D. Polymer 2024, 307, 127260.
9. Wang, W.; Huang, Q.; Zhao, C.; Li, Y.; Jiang, X. Polym. Eng. Sci. 2021, 61, 1096–1103.
10. Sako, T.; Date, J.; Hagi, M.; Hiraoka, T.; Matsuoka, S.; Yamaguchi, M., Anomalous viscosity decrease of polycarbonate by addition of polystyrene. *Polymer* **2019,** *170,* 135–141.
11. Moonprasith, N.; Nasri, M. S.; Saari, R. A.; Phulkerd, P.; Yamaguchi, M., Viscosity decrease by interfacial slippage between immiscible polymers. *Polym. Eng. Sci.* **2021,** *61,* 1096–1103.
12. Tanaka, Y.; Sako, T.; Hiraoka, T.; Yamaguchi, M.; Yamaguchi, M., Effect of morphology on shear

viscosity for binary blends of polycarbonate and polystyrene. *J. Appl. Polym. Sci.* **2020,** *137,* 49516.
13. Choe, S.; Cho, Y.; Lee, H.; Yoon, J. S.; Choi, H. J., Miscibility of poly(3-hydroxybutyrate-co-3-hydroxyvalerate) and poly(vinyl chloride) blends. *Polymer* **1995,** *36,* 4977-4982.
14. Liu, J.; Yuan, R.; Sang, Q.; Dang, L.; Gao, L.; Xu, B.; Xu, S., Effect of acetylated citrate plasticizer on mechanical properties of poly(vinyl chloride). *Mater. Chem. Phys.* **2023,** *295,* 127068.
15. Zhao, R.; Macosko, C. W., Slip at polymer–polymer interfaces: Rheological measurements on coextruded multilayers. *J. Rheol.* **2002,** *46,* 145–167.
16. Lee, J.; La, Y.-H.; Macosko, C. W. J. Rheol. 2009, 53, 893–905.
17. Lee, P. C.; Park, H. E., Morse, D. C.; Macosko, C. W., Polymer-polymer interfacial slip in multilayered films. *J. Rheol.* **2009,** *53,* 893-915.
18. Meller, M.; Luciani, A.; Sarioglu, A.; Manson, J. E., Flow through a convergence. Part 1: Critical conditions for unstable flow. *Polym. Eng. Sci.* **2002,** *42,* 611-633.
19. Yamaguchi, M.; Todd, D. B.; Gogos C. G., Rheological properties of LDPE processed by conventional processing machines. *Adv. Polym. Technol.* **2003,** *22,* 179-187.

Effect of ZnO/Chitosan/PVA Nanocomposite on the Surface Performance and Hydrophobicity of Golden Leaf

Supaporn Srifa[1], Ratchaneewan Siri[2], Pachara Pholnak[3]*
[1]*Department of Adult and Gerontological Nursing, Faculty of Nursing, Siam University, Bangkok, Thailand*
[2]*Division of Physical Science, Faculty of Science, Prince of Songkla University, Songkhla, Thailand*
[3]*Faculty of Science and Digital Innovation, Thaksin University, Phatthalung Campus, Phatthalung, Thailand*
**E-mail: pachara@tsu.ac.th*

Abstract:

The study aims to evaluate the effects of ZnO/chitosan/PVA nanocomposites on the appearance, hydrophobicity, and surface performance of golden leaf via spray and brushing techniques. Golden-phase leaves of the golden leaf vine were procured from two distinct locations within Narathiwat Province, Thailand, as well as from the Ban Bai Mai Group in Raman District, Yala Province. The accelerated ageing process of the coated gold leaf was systematically evaluated utilizing a QUV/spray weathering tester, thereby confirming an exceptional degree of preservation of the leaf's original appearance. UV-Vis spectrometry verified the UV absorption capabilities of the nanocomposite. Contact angle measurements indicated the intrinsic hydrophilicity of the uncoated gold leaf, with the spray-applied nano-ZnO/Chiosan/PVA composite demonstrating superior hydrophilic performance among the variants tested, characterized by low surface energy (2.39 mN/m). These findings suggest a substantial potential in the enhancement of local products utilizing these coatings, improving durability and functionality and promoting economic development in Thailand's southern border provinces.

1. Introduction

Bauhinia aureifolia, commonly referred to as the golden leaf vine, is a substantial woody climber found predominantly in the southern border provinces of Thailand, specifically Narathiwat, Pattani, and Yala.[1] It flourishes in rainforest habitats, such as those found in the Hala-Bala Wildlife Sanctuary and Bacho Waterfall National Park. This species is distinguished by its velvety, heart-shaped foliage, which undergoes a transformation in color over time, transitioning from copper in its initial stages to brown, then gold, and finally silver before senescence.[2] The leaf in its golden phase is garnering increasing interest for applications in decorative and sustainable materials. Zinc oxide (ZnO) is a multifunctional compound utilized in myriad applications, including as a coating.[3-5] When amalgamated with chitosan, ZnO engenders a versatile nanocomposite coating with promising applications in various domains.[6] Metal nanoparticles have also been incorporated into chitosan to enhance surface modifications across diverse materials, such as textiles.[7] For instance, polyethylene films coated with ZnO–chitosan nanocomposites have been shown to completely inactivate food pathogens, while chitosan-coated films only achieved a tenfold reduction in viable cell counts.[8] The water contact angle is also increased, signifying enhanced hydrophobic properties, a characteristic desired for non-wettable surfaces including plastics, fabrics, and paper.[9-11] Additionally, ZnO–chitosan coatings demonstrate commendable barrier properties, diminishing permeability and augmenting protective effects against environmental factors.[12]

This research endeavor seeks to preserve the intrinsic hydrophobicity, color, and texture of golden-phase leaves while enhancing their resistance to UV radiation and moisture through ZnO-based nanocomposite coatings. By maintaining the natural surface morphology and aesthetic characteristics, the study aims to extend the functional lifespan of these leaves for use in decorative and cultural applications. Various formulations and methods (i.e., brushing and spraying) of ZnO-based coatings were assessed using contact angle measurement to evaluate hydrophobicity and surface performance, providing a comprehensive understanding of how coating composition and application technique affect the preservation of leaf aesthetics and natural hydrophobic properties.

2. Materials and Methods

2.1 Materials

Golden-phase leaves of the golden leaf vine were procured from two distinct locations within Narathiwat Province—specifically, the Golden Leaf Group in Mueang and Ra-Ngae Districts—as well as from the Ban Bai Mai Group

in Raman District, Yala Province. The freshly harvested leaves exhibited a weight range between 0.72 and 2.53 grams. For the purpose of drying, the leaves were positioned within a plant press panel at ambient temperature (30–32°C) for the duration of one month. Subsequent to drying, the golden-phase leaves were systematically photographed and weighed. The resultant dry weights fluctuated between 0.61 and 1.89 grams, indicative of a moisture content spanning 10.26% to 30.09%. The desiccated leaf samples were subsequently subjected to coating using four distinct formulations and methodologies, as detailed in Table 1. Specifically, Sample Z1 was left uncoated as a control, Sample Z2 received a ZnO–chitosan coating via brush painting, Sample Z3 was treated with a ZnO–PVA coating through spraying, and Sample Z4 was coated with ZnO–PVA–chitosan also using the spraying method. For Samples Z2, Z3, and Z4, coating was applied solely to the right half of each leaf, thereby allowing the left half to remain uncoated for direct comparative analysis. In the preparation of composite coating solutions to augment the durability of golden-phase leaves, primary materials included commercially available food-grade chitosan (L.B. Science, Mw~4000), PVA (Chem-Suply, Mw~100,000), and ZnO nanopowder (MBK Chemical, 10-20 nm in diameter of partcle size).

2.2 Synthesis

The synthesis of the ternary ZnO–PVA–chitosan composite was conducted using a procedure reminiscent of established methodologies, with 1% acetic acid serving as the solvent medium. A 1:100 (w/v) solution of PVA was prepared by stirring at a temperature of 75°C until complete dissolution was achieved. ZnO nanopowder in various specified quantities (0.125 g, 0.25 g, and 0.50 g), was initially dispersed in 100 mL of the 1% acetic acid solution and subsequently combined with 100 mL of a pre-prepared chitosan solution and the PVA solution. The composite mixture underwent gentle stirring at 75°C for a duration of 30 minutes utilizing a hotplate stirrer, followed by sonication in an ultrasonic bath at ambient temperature for an additional 30 minutes. The resultant ZnO/PVA/chitosan composite solutions were sealed and preserved in labeled bottles for future application.

2.3 Characterization

The contact angle was ascertained utilizing a contact angle goniometer (Dataphysics OCA-15EC, Germany). The apparatus consisted of a light source for generating the droplet shadow profile, a high-resolution side-view camera, a precision liquid dispensing unit for the regulation of droplet volume, and image analysis software. To further investigate this characteristic, contact angle measurements and surface energy analysis were executed using a contact angle meter (Dataphysics OCA-15EC, Germany) equipped with the SCA20_U software in sessile drop mode. Water droplets (2 µL each) were meticulously deposited onto film specimens (1 × 3 cm) affixed to the sample stage. Three droplets were applied to each surface, and the corresponding images were documented. The mean contact angle was derived from the three independent measurements.

The accelerated ageing process of the coated golden-phase leaves was systematically evaluated utilizing a QUV/spray weathering tester, designed to replicate the effects of ultraviolet (UV) radiation, moisture, and condensation over abbreviated exposure intervals. In accordance with ASTM D4799/D4799M-17 standards, the samples underwent a series of 12-hour cycles, each comprising 4 hours of UV-A irradiation at a wavelength of 340 nm and a temperature of 50°C, followed by a 15 minute water spray, and concluding with 8 hours of controlled condensation at 50°C. Degradative changes were meticulously assessed post 1, 2, 4, 10, 14, and 18 cycles via surface colorimetric measurements and thorough visual inspections. Upon completion of 18 cycles, further investigation into the microscopic morphology and elemental composition was conducted through Scanning Electron Microscopy coupled with Energy Dispersive X-ray Spectroscopy (SEM–EDS) analysis. The colorimetric characterization of the accelerated golden-phase leaves was conducted using a CM-5 spectrophotometer (Konica Minolta), adhering to standardized colorimetry techniques. Following precise calibration of the instrument, leaf samples were strategically placed in the top-port measurement area for analysis in reflectance mode. The spectrophotometer yielded quantitative colorimetric data, encompassing RGB indices, spectral reflectance curves, and color-difference metrics, facilitating an accurate assessment of the color variations attributed to accelerated ageing.

3. Results

3.1 Color and appearance of coating gold leaf

The chromatic attributes and surface finish of gold leaf subsequent to nano-coating and spray application are analyzed. Referencing Figure 1, a comparative evaluation is made between the surface coloration of uncoated gold leaves and those treated with ZnO/chitosan nanocomposites via brushing (Figure 1a) or spraying (Figure 1b). The spray-coated samples exhibited the most favorable results, as the hue and surface features of the gold leaf closely matched those of the untreated variant, thereby confirming an exceptional degree of preservation of the leaf's original appearance. Empirical evidence suggests that the spray application method facilitates a more uniform and thinner layer distribution of the ZnO/chitosan nanocomposite on the gold leaf compared to the brushing technique. This uniform application effectively minimizes alterations to the intrinsic surface morphology and optical attributes of the leaf, thereby better conserving its inherent color and texture. Conversely, the brushing method generally results in a thicker, less uniform deposition, which can obscure or alter the surface characteristics. Consequently, spray coating is deemed the more efficacious strategy for maintaining the visual aesthetics of gold leaves while simultaneously enhancing their functional properties.

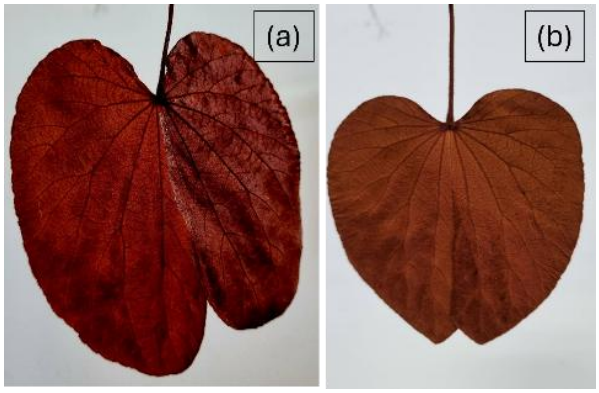

Figure 1. Surface appearance of golden leaves coated with (a) ZnO/chitosan nanocomposite by brushing and (b) ZnO/chitosan/PVA nanocomposite by spraying.

The results indicate that the spraying method provides a more uniform and thinner distribution of the ZnO/chitosan/PVA nanocomposite on the golden leaf surface compared to the brushing technique. This uniform coverage minimizes alteration of the natural surface morphology and optical properties of the leaf, thereby better preserving its original color and texture. In contrast, the brushing method tends to deposit a thicker and less homogeneous layer, which can obscure or modify the surface appearance. Hence, spray coating is considered the more effective technique for maintaining the aesthetic qualities of golden leaves while enhancing their functional properties.

3.2 SEM spectroscopy

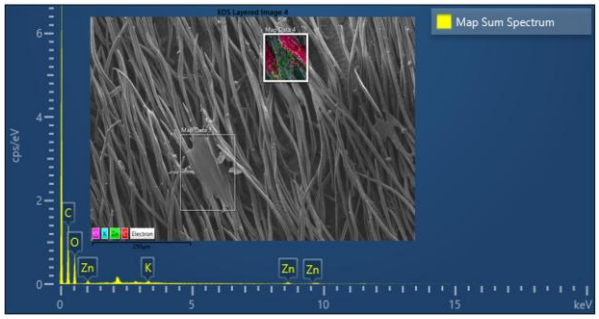

Figure 2. SEM micrograph and EDS spectrum of a gold leaf coated ZnO at 16,000x magnification.

Figure 2 presents the Energy Dispersive X-ray Spectroscopy (EDS) spectrum for the Z4 sample, indicating that the zones where the coating is adhered are primarily composed of zinc (Zn) and oxygen (O). Notably, prior research has elucidated the uptake of Zn by plants facilitated through ZnO nanoparticle coatings. The scanning electron microscope (SEM) micrograph elucidates the intrinsic microstructure of the golden leaf surface, marked by densely packed, elongated, and fibril-like formations. This hierarchical organization substantially contributes to the surface roughness, which is pivotal in augmenting hydrophobic characteristics by promoting a lotus-leaf-like water-repellent effect. These structural attributes corroborate the elevated contact angle measurements observed, emphasizing the significance of surface morphology in influencing wetting properties.

3.3 UV-Vis spectrometry

The ultraviolet to visible light (UV-vis) absorption spectrum is depicted in Figure 3. Figures 3(a)-(b) highlight the UV absorption peaks for the ZnO/chitosan composite solutions (Z2 and Z4), which manifest within the wavelength range of approximately 220 to 380 nm. This observation suggests that the synthesized samples possess effective UV absorption characteristics, rendering them appropriate for surface coating applications

aimed at shielding materials from environmental UV radiation.

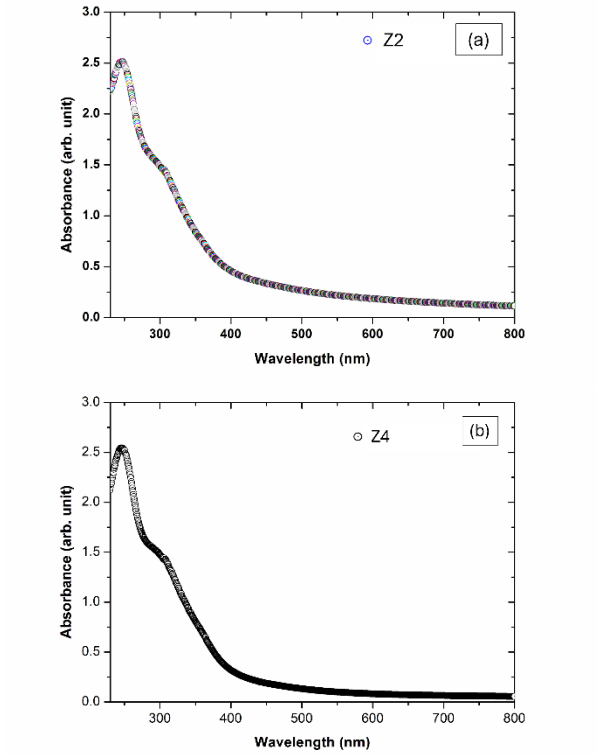

Figure 3. UV-vis absorption spectra of ZnO/chitosan and ZnO chitosan /PVA compounds associated with sample Z2 (a) and sample Z4 (b), respectively.

3.4 Contact angle measurements

Figure 4. Hydrophobicity on a coating surface of golden leaf vine.

Figure 4 illustrates the water droplets, which were observed to roll off the surface of the golden leaf in a manner akin to lotus leaves, thereby reflecting its intrinsic hydrophobic properties. For each sample, three droplets of deionized (DI) water were placed, imaged, and analyzed to ascertain the contact angles, with mean values being computed. For the purpose of surface energy analysis, three probe liquids with distinct polar and dispersive characteristics were utilized, namely DI water, ethylene glycol, and formamide. Three droplets of each liquid were deposited on the surfaces of the golden leaf, imaged, and analyzed to acquire contact angle values. The average surface energy was subsequently determined through the SE calculation method. The resultant contact angles and calculated surface energies of the golden leaf are encapsulated in Table 1.

Table 1. Average contact angle values measured with different probe liquids (DI water, ethylene glycol, and formamide) and the corresponding surface energy (SE) of golden leaf samples subjected to various nanocomposite coatings.

Sample	Surface treatment	Average contact angle (°)			Average SE (mN/m)
		DI water	Ethylene glycol	Formamide	
Z1	Uncoated (Control)	150.52 ± 2.59	136.52 ± 1.25	131.58 ± 2.14	4.79 ± 0.76
Z2	ZnO/Chitosan (paint)	72.05 ± 1.75	44.24 ± 2.05	49.57 ± 2.74	38.64 ± 0.71
Z3	ZnO/PVA (spray)	87.32 ± 1.29	84.80 ± 1.83	85.38 ± 2.15	20.61±0.78
Z4	ZnO/Chitosan/PVA (spray)	136.63 ± 2.92	129.78 ± 2.21	126.47 ± 2.04	2.39 ± 0.48

As illustrated in Table 1, the uncoated golden leaf (Z1) exhibited a notably high water contact angle of 150.52°, along with an exceptionally low surface energy measured at 4.79 mN/m, thereby affirming its intrinsic hydrophobic characteristic comparable to lotus leaves. Following the application of a ZnO/chitosan coating (Z2), a significant reduction in contact angle was observed across all probe liquids, accompanied by an increment in surface energy to 38.64 mN/m. This enhancement in wettability can be attributed to the hydrophilic properties of chitosan. Conversely, the ZnO/PVA spray coating (Z3) demonstrated moderate hydrophilicity, with contact angles approximating 85° and a surface energy of 20.61 mN/m, indicating a compromise between the hydrophilic and film-forming attributes of PVA. Notably, the ZnO/chitosan/PVA spray coating (Z4) maintained a relatively elevated contact angle of 136.63° with water and achieved the lowest surface energy, recorded at 2.39 mN/m, which signifies a partial restoration of hydrophobicity. This phenomenon may be

attributed to synergistic interactions between the chitosan–PVA matrix and ZnO nanoparticles, resulting in surface reorganization and diminished wettability.

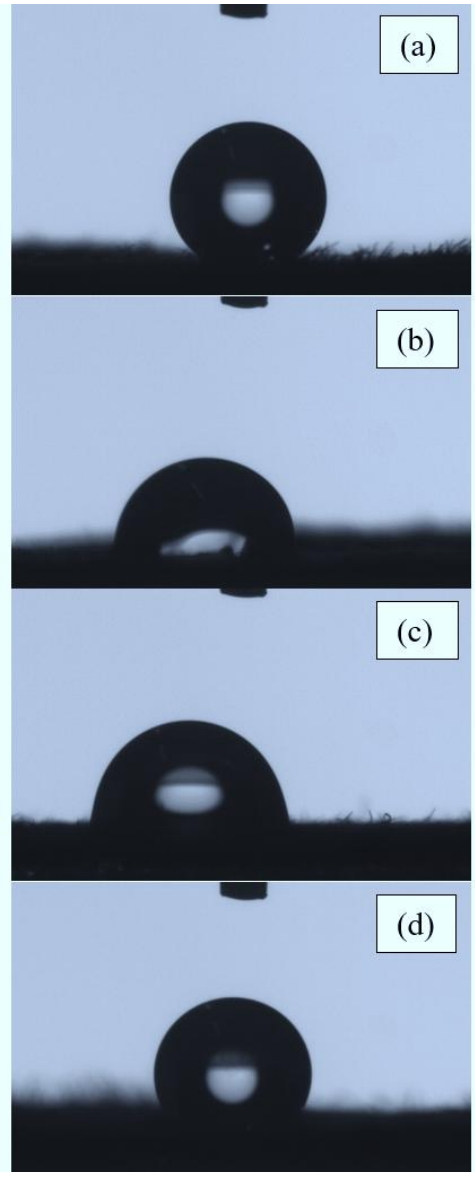

Figure 5. Representative images of water droplets deposited on golden leaf surfaces measured by the contact angle technique: (a) uncoated control, (b) ZnO/Chitosan (paint), (c) ZnO/PVA (spray), and (d) ZnO/Chitosan/PVA (spray).

Conversely, Sample Z4, which was coated with a ZnO/Chitosan/PVA nanocomposites via spray deposition, exhibited an average contact angle of 136.63° along with the lowest surface energy of 2.39 mN/m, thus implying minimal droplet adhesion and thereby enhanced hydrophobic performance. In contrast, Samples Z2 and Z3 displayed markedly lower average contact angles of 72.05° and 87.32°, respectively, which were accompanied by elevated surface energy values, fostering increased droplet adhesion to the leaf surface. Consequently, Sample Z4 demonstrated superior hydrophobicity, rendering it more efficacious in resisting interaction with humid air and water droplets.

The uncoated golden leaf (Sample Z1) demonstrated the highest average contact angle values, surpassing 150.52° with DI water, indicative of substantial intrinsic hydrophobicity. Conversely, Samples Z2 and Z3, which were coated with ZnO/Chitosan (paint) and ZnO/PVA (spray), respectively, revealed notably lower contact angles (72.05° and 87.32° with DI water) along with higher surface energies, thereby implying diminished hydrophobicity and increased wettability. Significantly, Sample Z4, coated with a ZnO/Chitosan/PVA composite (spray), sustained a relatively elevated average contact angle of 136.63° with DI water and exhibited the lowest surface energy (2.39 mN/m), thereby confirming its superior hydrophobic performance among the coated samples.

3.5 Accelerated ageing test and color changes

Figure 6 illustrates that the samples coated with the ZnO–PVA–chitosan composite exhibited the minimal alterations in colorimetric values, specifically in the RGB spectra of gold-colored foliage subjected to QUV accelerated aging cycles, which ranged from 0 to 18. This empirical evidence denotes a robust resistance to color degradation, thereby suggesting that the ZnO–PVA–chitosan encapsulation provides the most efficacious protection in maintaining the pristine visual characteristics of golden-phase leaves. This formulation surpasses both alternative coating methodologies and the untreated control in terms of preservation efficacy.

The development of golden leaf-based products and the improvement of their hydrophobic properties using nano-ZnO-PVA-chitosann composite colliods offer a promising approach to upgrading community products in Thailand's southern border provinces. By coating golden leaves and residues with natural rubber latex, durability, flexibility, and longevity are enhanced. Through creative design, these enhanced materials can be transformed into practical and decorative items such as wallets, garments, and home accessories. This process not only adds value to previously discarded materials

but also generates sustainable income for local communities.

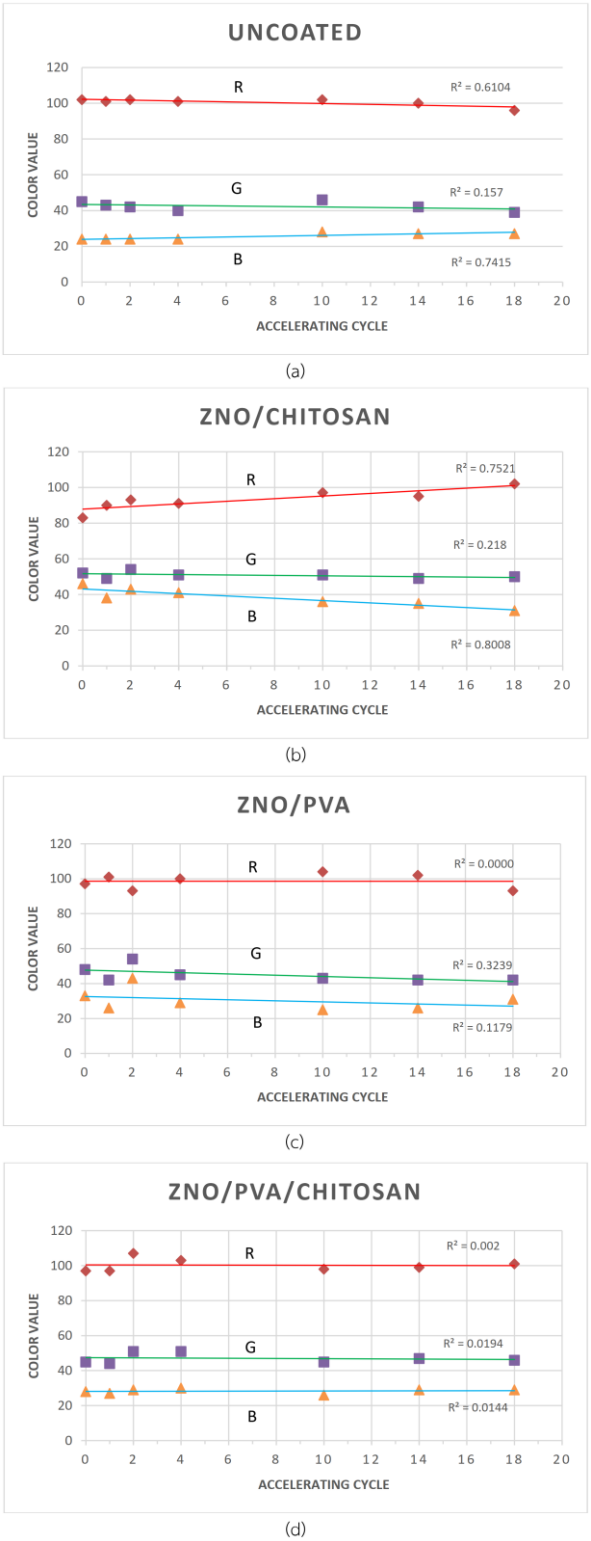

Figure 6. The graph illustrates a comparative analysis of the color index (RGB) values of the gold-colored leaves under QUV accelerated aging cycles, specifically: (a) Z1, (b) Z2, (c) Z3, and (d) Z4.

Figure 7. The design of the product prototype is made from coating gold leaf and is shaped like a souvenir in the form of a women's bag.

Conclusion

The investigation assesses the application of ZnO/chitosan and ZnO/chitosan/PVA nanocomposites on gold leaf via spray and brushing techniques, examining their effects on appearance, hydrophobicity, and surface energy. Spray coating yielded a more uniform and thinner layer, thereby preserving the original aesthetics of the gold leaf more effectively compared to brushing. SEM analysis revealed a surface morphology that enhances hydrophobic properties. UV-Vis spectrometry verified the UV absorption capabilities of the nanocomposites. Contact angle measurements indicated the intrinsic hydrophobicity of uncoated gold leaf, with the spray-applied ZnO/chitosan/PVA composite demonstrating superior hydrophobic performance among the variants tested, characterized by low surface energy. Of the three coatings assessed, the ZnO–PVA–chitosan mix applied to golden-phase leaves offered the best protection against moisture and ultraviolet (UV) light. This coating exhibited minimal color fading after 18 cycles of artificial aging while maintaining the original color's chromatic accuracy. The spray application method ensured an even coverage on the leaf surface, significantly boosting the mechanical strength and lifespan of the golden-phase leaves. From a practical standpoint, the ZnO–PVA–chitosan spray holds considerable promise for shielding golden-phase leaves from moisture and UV exposure, aiding in the preservation of their aesthetic appeal and prolonging the functional life of local handicrafts and decorative items made from these leaves.

Acknowledgements
This work was financially supported by Thaksin University for fiscal year 2024.

References

1. Sraphet, S.; Sukawutthiya, P.; Srisawad, N.; Duncan, R. S.; Triwitayakorn, K., Evaluation of the Genetic Diversity of *Bauhinia winitii*, an Endemic Plant of Thailand, Using Microsatellite Markers. *Philipp. J. Sci.* **2021**, *150* (2), 557–569.
2. Larsen, K.; Larsen, S. S., Notes on the Genus *Bauhinia* (Leguminosae-Caesalpinioideae) in SE Asia. *Nord. J. Bot.* **1991**, *11* (6), 629–634.
3. Monika, P.; Hari Krishna, R.; Hussain, Z.; Nandhini, K.; Pandurangi, S. J.; Malek, T.; Kumar, S. G., Antimicrobial Hybrid Coatings: A Review on Applications of Nano ZnO-Based Materials for Biomedical Applications. *Biomater. Adv.* **2025**, *172*, 214246.
4. Wafi, A.; Khan, M. M., Green Synthesized ZnO and ZnO-Based Composites for Wound Healing Applications. *Bioprocess Biosyst. Eng.* **2025**, *48*, 521–542.
5. Zare, A., Application of β-CD to Control the Release of ZnO Nanoparticles on the Silk Fabric Surface along with Citric Acid as Eco-Friendly Cross-Linker. *Prog. Color Color. Coat.* **2023**, *16* (3), 295–307.
6. Chavez-Esquivel, G.; Ángeles-Beltrán, D.; Tellez de la Torre, P. M.; Cortes-Cordova, D. E.; Huerta-Arcos, L.; Estrada de los Santos, P., Antimicrobial and Antifungal Edible Coatings with ZnO Nanoparticles Dispersed in a Chitosan-Guar Gum Matrix for Hass Avocado Preservation. *Int. J. Biol. Macromol.* **2025**, *308* (Part 4), 142467.
7. Sadeghi-Kiakhani, M.; Hashemi, E., Study on the Effect of Pomegranate Peel and Walnut Green Husk Extracts on the Antibacterial and Dyeing Properties of Wool Yarn Treated by Chitosan/Ag, Chitosan/Cu Nanoparticles. *Prog. Color Color. Coat.* **2023**, *16* (3), 221–229.
8. Al-Naamani, L.; Dobretsov, S.; Dutta, J., Chitosan-Zinc Oxide Nanoparticle Composite Coating for Active Food Packaging Applications. *Innov. Food Sci. Emerg. Technol.* **2016**, *38* (A), 231–237.
9. Yu, D.; Basumatary, I. B.; Liu, Y.; Zhang, X.; Kumar, S.; Ye, F.; Dutta, J., Chitosan-Photocatalyst Nanocomposite on Polyethylene Films as Antimicrobial Coating for Food Packaging. *Prog. Org. Coat.* **2024**, *186*, 108069.
10. Evren, G.; Koşak Söz, Ç.; Özomay, Z.; Uzun, M.; Sönmez, S., Effect of the Coating Formulation on the Barrier Properties and Final Appearance of Non-Wettable Hybrid Paper Sheets. *Prog. Color Color. Coat.* **2024**, *17* (3), 239–262.
11. Márton, P.; Nagy, Ö. T.; Kovács, D.; Szolnoki, B.; Madarász, J.; Nagy, N.; Szabó, G. S.; Hórvölgyi, Z., Barrier Behaviour of Partially N-Acetylated Chitosan Layers in Aqueous Media. *Int. J. Biol. Macromol.* **2023**, *232*, 123336.
12. Szőke, Á. F.; Szabó, G.; Simó, Z.; Hórvölgyi, Z.; Albert, E.; Végh, A. G.; Zimányi, L.; Muresan, L. M., Chitosan Coatings Ionically Cross-Linked with Ammonium Paratungstate as Anticorrosive Coatings for Zinc. *Eur. Polym. J.* **2019**, *118*, 205–212.

Adsorption and Hydrolysis of Carbaryl Promoted by Biochar Derived from Byproducts from Pineapple Leaf Fibre Processing

Jutamanee Boonnoon[1], Natthawadi sukkhanit[2], Chaiwat Rattanet[3], Taweechai Amornsakchai[2], Tanongkiat Kiatsiriroat[3], Puangrat Kaewlom[4], Siwaporn M. Smith[2] *
[1]*Postgraduate program in Chemistry, Faculty of Science, Mahidol University, Salaya 73170, Thailand*
[2]*Center of Sustainable Energy and Green Materials and Department of Chemistry, Faculty of Science, Mahidol University, 999 Phuttamonthon Sai 4 Road, Salaya 73170, Thailand*
[3]*Department of Mechanical Engineering, Faculty of Engineering, Chiang Mai University 239, Huay Kaew Road, Muang District, Chiang Mai 50200, Thailand*
**E-mail: Siwaporn.smi@mahidol.ac.th*

Abstract:

Biochar materials have been widely applied to improve soil and water quality. This study reports utilizing non-fibrous materials (NFM) in pineapple leaf to produce a biochar material denoted as NFMBC. The NFMBC was later examined as a sorbent for the removal of carbaryl, an insecticide, from water. NFMBC treatments of carbaryl (aq) solution (50 ppm), with 1 g L^{-1} of NFMBC at 25 ºC, gave removal efficiencies of ca. 94% after 12 h, *via* involves pore-filling, π–π and electrostatic interactions between the insecticide and the biochar. In addition to adsorption, hydrolysis of carbaryl also took place, resulting in 56% µmol of 1-naphthol product. Time-dependent treatments indicated that the concentration of 1-naphthol increases at prolong treatment times. As a result, the biochar acts not only as an adsorbent for carbaryl removal but also as hydrolysis active sites. Possibly, metal or mineral compounds on the biochar surface may play an important role in carbaryl hydrolysis, which were not observed from other biochar treatments in previous reports. Notably, 1-naphthol is less toxic than carbaryl and degrades more easily (half-life 3.6 h), showcasing that NFMBC can be used as an environmental material for the treatment of carbaryl-contaminated wastewater.

1. Introduction

Carbaryl, a carbamate insecticide widely used in agriculture, is of concern due to its mobility in water and potential toxicity to non-target organisms. Conventional removal methods are often inefficient or costly, making it interest in biochar-based adsorption approaches.

Biochar, a carbon-rich material produced by oxygen-limited pyrolysis of biomass, has attracted attention as a sustainable adsorbent because of its porous structure, surface functionality, and environmental benefits. Previous studies have shown its strong affinity for hydrophobic organic chemicals (HOCs) and pesticides, making it promising for water treatment.[1]

In this study, biochar derived from non-fibrous pineapple leaf residue was examined for its ability to remove carbaryl from aqueous solution and/or hydrolyze it into less toxic forms[2]. Adsorption efficiency and interaction mechanisms were evaluated, highlighting the potential of agricultural waste-derived biochar in pesticide remediation.

2. Materials and Methods

2.1 Materials

The byproduct of non-fibrous material (NFM) was obtained from fiber extraction of pineapple leaf waste. The dried material was ground into powder using a high-speed grinder (Model 200A, 1,200 W) with stainless-steel blades, then sieved through an aluminum mesh to collect particles in the 33–47 µm size range, for further use. In addition, commercially available carbaryl (Hebei Enge Biotech, 85%w/w) was purchased from local shops in Thailand. Throughout this work, deionized water was utilized as solvent.

2.2 Synthesis

The non-fibrous material (NFM) was pyrolyzed at 550 °C for 2 h in a closed 300 mL ceramic crucible under a heating rate of 10 °C min^{-1} and a nitrogen flow of 100 mL min^{-1} to obtain the non-fibrous material biochar (NFMBC).[3]

2.3 Characterization

The structure, chemical composition, and physical properties of NFMBC were analyzed using several analytical methods. Elemental compositions were determined with a CHNS/O analyzer (Leco, A 628 series, USA) and an X-ray fluorescence spectrophotometer (XRF, Horiba, XTG-9000, Japan). Proximate analysis for

moisture, volatile matter, and ash content was performed according to ASTM D3173 and ASTM D3174 using a SNOL 3/1100 LHM01 furnace. Fixed carbon content was calculated from the residual components other than moisture, ash, and volatile matter. The microstructure and surface morphology of samples were observed using a scanning electron microscope (FESEM, JEOL, JSM-IT500, Germany) after platinum coating (30 mA, 90 s). Crystalline phases were identified by X-ray diffraction (XRD, Bruker, D2 Phaser, Germany) over a 2θ range of 10-50°. Raman spectra were recorded using a Raman spectrophotometer (HORIBA Scientific, XploRA PLUS, France). Surface chemical compositions were analyzed with X-ray photoelectron spectroscopy (XPS, Kratos, Axis Ultra DLD, UK) and Fourier-transform infrared spectroscopy (FTIR, Nicolet, iS50, USA) in the range of 400–4000 cm^{-1}.

2.4 Batch Adsorption

Only a single parameter was varied at the time, and each batch sorption experiment was performed in triplicate. Screening test was carried out at 25°C to determine the removal efficiency examined by using 20 mL of 50 ppm carbaryl aqueous solution with 1 g L^{-1} NFMBC sorbent dosages. Using a ZHWY 200B model Zhicheng brand temperature-controlled mechanical shaker, the suspensions (NFMBC in pesticide solution) were shaken at 150 rpm. Once the designated contact time was reached, the liquid phase was drawn out by using a 0.45 µm cellulose acetate syringe filters and collected for HPLC analyses. For each HPLC measurement, a 2 mL of treated pesticide solution was injected into an HPLC-ready vial for subsequent analysis without dilution step. The concentrations of pesticide in the treated solutions were monitored on a Waters ACQUITY Arc system, USA, HPLC coupled with a VertiSep UPS C18 column (5 µm, 4.6 x 150 mm). The operating conditions during analysis included a flow rate of 1 mL/min, a column temperature of 30°C, an injection volume of 20 µL, and detection wavelength at 280 nm. The HPLC isocratic elution conditions used in this work was 50% deionized water: 50% acetonitrile. The adsorption capability of each pesticide over NFMBC was evaluated in terms of the pesticide uptake (Eq. 1)

$$q_e = \left(\frac{C_o - C_e}{m}\right) \times V \qquad \text{(Eq. 1)}$$

where q_e represents equilibrium adsorption capacity in mg g^{-1}, V the volume of the adsorbate solution in L, and m the mass of the adsorbent in g.

3. Results

3.1 Bulk Composition

Table 1. Bulk composition (from CHN method and proximate analysis) of NFMBC (maximum error 0.3%).

Elemental Composition (%wt.)							
C	H	N	O	$\frac{H}{C}$	$\frac{O}{C}$	$\frac{N}{C}$	$\frac{O+N}{C}$
79.90	3.63	0.89	15.58	0.54	0.15	0.01	0.16

Composition (%wt.) (Proximate analysis)			
Moisture content	Ash	Volatile matter	Fixed carbon
4.5	7	9	79.5

Through the process of pyrolysis, wherein organic materials are subjected to high temperatures, the resulting biochar exhibits a notable bulk composition comprised mainly of carbon, oxygen, hydrogen, and nitrogen. The H/C and O/C ratios, indicative of aromaticity and polarity, respectively, provide insights into the molecular structure and reactivity of the biochar [4]. Approximately 7% of the composition consists of ash, originating from trace mineral or inorganic deposits during pyrolysis, with calcium and potassium emerging as predominant elements as shown in Figure 1. These elements, reflective of their natural biomass sources, contribute to the distinctive characteristics of the biochar. In essence, the bulk composition of pyrolysis-derived biochar reveals a complex interplay of elements, emphasizing its carbonaceous nature and the influence of its natural origins.[5]

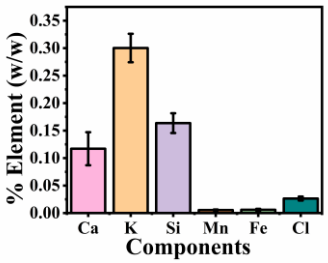

Figure 1. Elemental analysis by XRF (>23 amu.)

3.2 Chemical and Structural

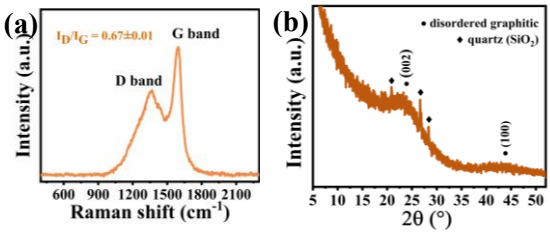

Figure 2. (a) aromatic structure by Raman (b) crystalline structure by XRD.

Raman spectra showcased two distinctive peaks at approximately 1,350 cm^{-1} (D-band) and 1,600 cm^{-1} (G-band). These peaks suggest the development of aromatic structures with defects and well-ordered graphite structures, respectively.[6] The intensity ratio (I_D/I_G) of 0.67±0.01 signifies the prevalence of graphitic carbon in NFMBC, aligning remarkably well with the $\frac{H}{C}$ and $\frac{O}{C}$ ratios derived from CHN data, as discussed in the Table 1. Moreover, Figure 2(b) highlights that X-ray diffraction also affirmed the presence of disorderly graphitic structures, echoing the Raman findings. Additionally, traces of quartz were identified on the NFMBC surface, in concordance with XRF results indicating the observation of silicon in minute amounts.

3.3 Surface Composition

Four elements were observed which were C, O, Ca and K, align with XRF results. The elements deconvolution showed the functional groups on surface. For example, C=C, carbonyl group, or even carbonate group on NFMBC. $CaCO_3$ and KCO_3.[7] The pore structure analysis showed an average pore diameter of 3.63 ± 0.2 nm, indicating the presence of mesopores,[8] a total pore volume of 0.0035 cm^3 g^{-1}, and a low BET surface area of 4.01 m^2 g^{-1}. These surface characteristics, including functional groups and porous structure, suggest that NFMBC has the potential to adsorb pesticide molecules from aqueous solutsions.

3.4 Effect of Time

A carbaryl removal efficiency of 94% was observed after 720 minutes by using NFMBC (Figure 4a). Moreover, the NFMBC catalyzed the hydrolysis of carbaryl, resulting in the production of naphthol at a rate of 56% µmol (Figure 4b).

3.5 Adsorption Mechanism

As shown in Figure 5, the presence of a carbaryl peak in the spent NFMBC confirmed its

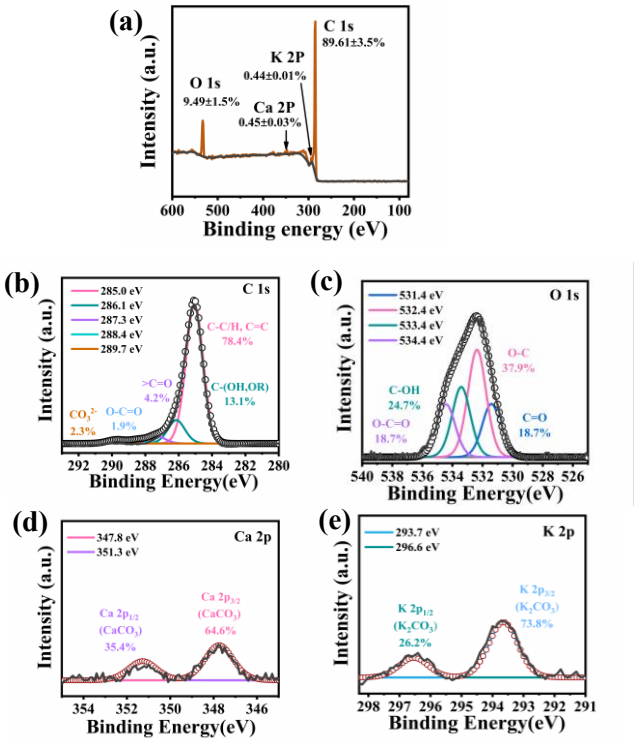

Figure 3. Surface functional group of NFMBC by XPS (a) Survey spectra (b) C1s (c) O1s (d) Ca2p (e) K2p (Black solid line represents experimental profile and red circles indicates the simulated profile).

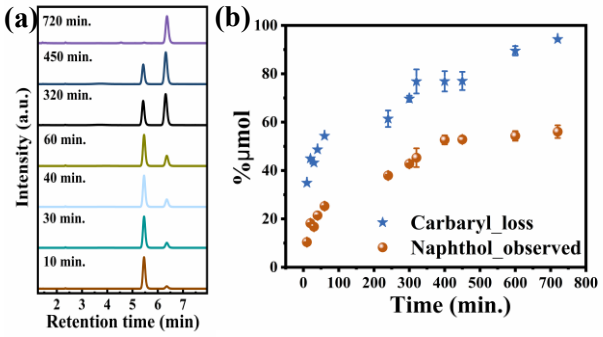

Figure 4. Effect of contact time of NFMBC on (a) Chromatogram and (b) the %µmol of carbaryl loss and naphtol observed.

adsorption onto the biochar surface. Changes in the C1s and O1s percentages after adsorption indicated modifications in surface chemistry.[9,10] The deconvolution of the C1s and O1s spectra revealed peak shifts, highlighting the role of functional groups in governing the adsorption process. The experimental adsorption data fitted well with the intraparticle diffusion (IPD) model, suggesting that carbaryl gradually diffuses into the biochar pores.[11] This slow diffusion process may also

facilitate the gradual release of alkaline ions from the biochar surface, linking adsorption and hydrolysis in the overall removal of carbaryl.

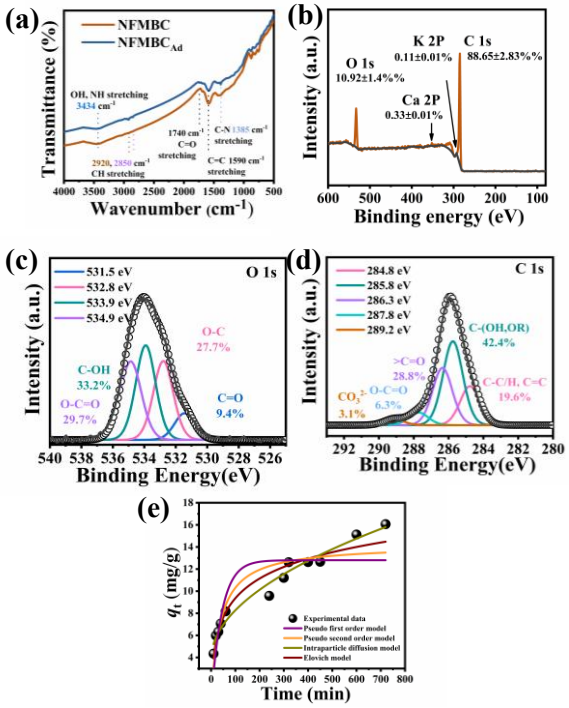

Figure 5. (a) FTIR spectra of spent NFMBC and XPS spectra after adsorption of NFMBC (b) Survey (c) O 1s (d) C 1s (e) adsorption data with kinetic model fits.

3.6 Hydrolysis Mechanism

The percentages of K2p and Ca2p decreased, and their deconvolution peaks shifted to slightly higher binding energies in spent NFMBC, indicating partial involvement of K_2CO_3 and $CaCO_3$ during carbaryl removal. The dissolution of these carbonate minerals caused a small increase in solution pH from 7.1 to 7.4, which may contribute to the alkaline hydrolysis of carbaryl.[10, 12] Notably, NFMBC not only adsorbs carbaryl but also provides conditions that could enhance hydrolysis, whereas previous studies generally reported biochar functioning mainly as an adsorbent.[13] The IPD behavior observed in the adsorption kinetics suggests that carbaryl diffusion into biochar pores and gradual ion release may together support the overall removal process.

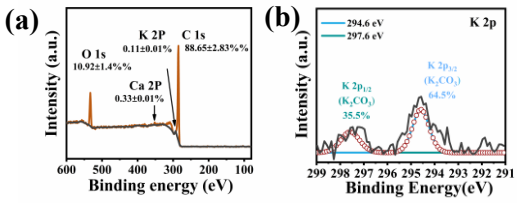

Figure 6. XPS spectra after adsorption of NFMBC (a) Survey (b) K2p.

Conclusion

NFMBC demonstrated excellent potential for carbaryl remediation, achieving 94% removal efficiency within 720 minutes. In addition to adsorption, the material exhibited catalytic activity, attributable in part to trace inorganic carbonates, facilitating hydrolysis and producing 1-naphthol at a yield of 56% µmol. These findings highlight the dual functionality of NFMBC as both an effective adsorbent and a catalyst, underscoring its promise or practical applications in pesticide-contaminated water treatment.

Acknowledgements

The research is financially supported by Mahidol University (Fundamental Fund: fiscal year 2023 by National Science Research and Innovation Fund (NSRF)); Grant No. FF-069/2566. JB received a Mahidol University Scholarship for Young Scientists. The authors are thankful for the instrumentation support from the Mahidol University-Frontier Research Facility (MU-FRF), SMJ lab, Assoc. Prof. Dr. Siwaporn Meejoo Smith and Suwilai Chaveanghong for their assistance and advice.

References

1. Cao, X.; Harris, W., Properties of dairy-manure-derived biochar pertinent to its potential use in remediation. *Bioresource Technology*. **2010**, *101* (14), 5222-5228. DOI:https://doi.org/10.1016/j.biortech.2010.02.052.
2. Beyers, D. W.; Carlson, C. A.; Keefe, T. J., Toxicity of carbaryl and malathion to two federally endangered fishes, as estimated by regression and Anova. *Environ. Toxicol. Chem.* **1994**, *13* (1), 101-107. DOI: 10.1002/etc.5620130114 (acccessed 9/29/2025).
3. Masoumi, S.; Borugadda, V. B.; Nanda, S.; Dalai, A. K. Hydrochar: A Review on Its Production Technologies and Applications. *Catalysts* **2021**, *11* (8), 939.
4. Lau Abdullah, M. S.; Hamid, N. A., Turning Coconut Residue into Hydrochar using Hydrothermal Carbonization. *IOP Conference Series: Materials Science and Engineering.*

2021, *1192* (1), 012033. DOI: 10.1088/1757-899X/1192/1/012033.

5. Zhang, Y.; Jiang, Q.; Xie, W.; Wang, Y.; Kang, J., Effects of temperature, time and acidity of hydrothermal carbonization on the hydrochar properties and nitrogen recovery from corn stover. *Biomass and Bioenergy.* **2019**, *122*, 175-182. DOI: https://doi.org/10.1016/j.biombioe.2019.01.035.
6. Soh, M.; Khaerudini, D. S.; Chew, J. J.; Sunarso, J., Wet torrefaction of empty fruit bunches (EFB) and oil palm trunks (OPT): Effects of process parameters on their physicochemical and structural properties. *South African Journal of Chemical Engineering.* **2021**, *35*, 126-136. DOI: https://doi.org/10.1016/j.sajce.2020.09.004.
7. Zhang, L.; Liu, S.; Wang, B.; Wang, Q.; Yang, G.; Chen, J., Effect of Residence Time on Hydrothermal Carbonization of Corn Cob Residual. *BioResources.* **2015**, *10*. DOI: 10.15376/biores.10.3.3979-3986.
8. Chen, J.; Zhang, L.; Yang, G.; Wang, Q.; Li, R.; Lucia, L., Preparation and Characterization of Activated Carbon from Hydrochar by Phosphoric Acid Activation and its Adsorption Performance in Prehydrolysis Liquor. *BioResources.* **2017**, *12*, 5928-5941. DOI: 10.15376/biores.12.3.5928-5941.
9. Adebisi, A.; Chowdhury, Z.; Abd Hamid, S. B.; Ali, M., Hydrothermally Treated Banana Empty Fruit Bunch Fiber Activated Carbon for Pb(II) and Zn(II) Removal. *BioResources.* **2016**, *11*. DOI: 10.15376/biores.11.4.9686-9709.
10. Maiti, R.; Midya, A.; Narayana, C.; Ray, S. K. Tunable optical properties of graphene oxide by tailoring the oxygen functionalities using infrared irradiation. *Nanotechnology.* **2014**, *25* (49), 495704. DOI: 10.1088/0957-4484/25/49/495704.
11. Yan, X.; Xu, T.; Chen, G.; Yang, S.; Liu, H.; Xue, Q., Preparation and characterization of electrochemically deposited carbon nitride films on silicon substrate. *J. Phys. D: Appl. Phys.* **2004**, *37*, 1-7. DOI: 10.1088/0022-3727/37/6/015.
12. Soffian, M. S.; Abdul Halim, F. Z.; Aziz, F.; A . ,Rahman, M.; Mohamed Amin, M. A.; Awang Chee, D. N. Carbon-based material derived from biomass waste for wastewater treatment. *Environmental Advances.* **2022**, *9*, 100259. DOI: https://doi.org/10.1016/j.envadv.2022.100259.
13. Fang, J.; Gao, B.; Chen, J.; Zimmerman, A. R., Hydrochars derived from plant biomass under various conditions: Characterization and potential applications and impacts. *Chemical Engineering Journal.* **2015**, *267*, 253-259. DOI:https://doi.org/10.1016/j.cej.2015.01.026.
14. Du, H.; Lei, Y.; Chen, W.; Li, F.; Li, H.; Deng, W.; Jiang, G., Multifunctional Magnetic Bio-Nanoporous Carbon Material based on Zero-Valent Iron, Angelicae Dahuricae Radix Slag and Graphene Oxide: An efficient adsorbent of pesticides. *Arabian Journal of Chemistry.* **2021**, *14*, 103267. DOI: 10.1016/j.arabjc.2021.103267.
15. Zhang, P.; Sun, H.; Yu, L.; Sun, T. ,Adsorption and catalytic hydrolysis of carbaryl and atrazine on pig manure-derived biochars: Impact of structural properties of biochars. *Journal of Hazardous Materials.* **2013**, *244-245*, 217-224. DOI: https://doi.org/10.1016/j.jhazmat.2012.11.046.
16. Gao, W.; Shi, Y.; Zhou, Y.; Jia, J.; Chen, S., Biochar with further enhanced properties prepared by acid base combined pretreatment for removal of water pollutants. *Scientific Reports.* **2025**, *15* (1), 19432. DOI: 10.1038/s41598-025-03992-8.
17. Arroyo, L. J.; Li, H.; Teppen, B. J.; Johnston, C. T.; Boyd, S. A., Hydrolysis of carbaryl by carbonate impurities in reference clay SWy-2. *J Agric Food Chem.* **2004**, *52* (26), 8066-8073. DOI: 10.1021/jf048971b From NLM.
18. Srikhaow, A.; Win, E. E.; Amornsakchai, T.; Kiatsiriroat, T.; Kajitvichyanukul, P.; Smith, S. M., Biochar Derived from Pineapple Leaf Non-Fibrous Materials and Its Adsorption Capability for Pesticides. *ACS Omega.* **2023**, *8* (29), 26147-26157. DOI: 10.1021/acsomega.3c02328.

Release Profiling of Bioactives from Silicone-Based Patches

Apatcha Chatikanont[1], Areechun Sotthibundhu[1], Robert Marks[2], Yardnapar Parcharoen[1], and Sitakan Natphopsuk[1 *]
[1]*Chulabhorn International College of Medicine, Thammasat University, Pathum Thani 12120, Thailand*
[2]*Department of Biotechnology Engineering, Avram and Stella GoldsteinGoren, Ben-Gurion University of the Negev, Beer-Sheva 84105, Israel*
**E-mail: sitakan@tu.ac.th*

Abstract:

Silicone-based patches were developed as consumer-informed systems to conceal bruises, aligning with the growing demand in aesthetic procedures. A survey of 136 participants revealed interest, with 75.6% willing to buy bruise-alleviation products, 85.2% preferring concealing treatments, and 83.7% favoring options that both mitigate pain and improve bruise appearance. Guided by these insights, three botanical extracts madecassoside, titrated extract of *Centella asiatica*, and *Aloe vera* were evaluated for cytocompatibility. Among them, *Aloe vera* was chosen due to its demonstrated fibroblast viability of 113.0 ± 5.41% at a concentration of 250 µg/mL. Ultraviolet-visible spectroscopy identified distinct absorbance maxima at 223 and 262 nm, with 262 nm selected to reduce interference from excipients. A power-law calibration at 262 nm was used to convert absorbance to concentration for quantitative release. Patches were fabricated at 500, 1,000, and 2,000 rpm, representing low/medium/high shear to identify shear-dependent effects. Cumulative percent release was highest at 2,000 rpm by 270 min, followed by 1,000 rpm, and negligible at 500 rpm. The results illustrate the viability of combining user feedback with quantitative release profiling, thus creating a systematic foundation for enhancing active-loaded transdermal patches.

1. Introduction

Bruises, medically referred to as ecchymosis, are a form of skin discoloration caused by bleeding veins and capillaries beneath the skin. They are sometimes painful and can take a long time to fully heal. In daily life, bruising is a common occurrence, and both medical conditions and procedures may increase its likelihood.[1, 2] In the cosmetic sector, bruising is a frequent adverse effect that can cause embarrassment for patients concerned about their appearance. This often results in avoidance of social and professional responsibilities for up to two weeks following a procedure.[3] Reports indicate that bruising may represent approximately 25% of nonsurgical cosmetic procedures, with some sources noting incidences as high as 68%.[4]

If a bruise has already occurred, cold packs are recommended within the first 48 hours followed by hot compresses after two days to shorten recovery. Color correction for bruises adheres to the color principle: opposing hues on color wheel visually neutralize each other; thus, correctors are selected according to the bruise's color. In dermatologic camouflage, blue and purple discoloration is counteracted with orange and yellow correctors, applied prior to the skin-tone layer. Conversely, red is counteracted with green correctors. Bruises generally progress from red/blue-purple initially to yellow later as hemoglobin degrades; thus, the selected corrector should correspond with the observed coloration over time. Currently, the cosmetic industry is trending toward the incorporation of natural ingredients in product formulations. A wide range of bruise-alleviation products are available, including gels, creams, and oils.[5-7]

Madecassoside and titrated extract of *Centella asiatica* (TECA), along with *Aloe vera*, are widely used in remedies to reduce bruising. However, the mechanism of their effects in topical applications is not yet fully understood. Consequently, scientific evidence supporting their anti-bruising properties, particularly in relation to bruise and wound healing duration, remains limited. As physical appearance is highly prioritized in modern society, individuals often worry that slow bruise recovery will prolong social discomfort.[8-10]

The mixing speed was established as a design parameter because, in immiscible polymer dispersions, hydrodynamic shear dictates droplet fragmentation versus coalescence, thereby determining the microstructure that subsequently influences transport, in accordance with polymer-dispersion theory.[11, 12] Data from phase-inversion systems demonstrate a pivotal stirring velocity; increased rpm consistently diminishes droplet dimensions and tightens the distribution, with average sizes decreasing from lower to higher rpm,

300-1000 RPM.[13] In silicone systems, mixing glycerol in polydimethylsiloxane (PDMS) from 2,000 to 3,500 rpm is documented, with the elevated setting producing smaller droplets.[14] The shear-driven enhancement of morphology, smaller droplets, and increased interfacial area establishes a mechanistic connection to mass transport, as finer dispersions facilitate more rapid drug release into the external phase at the skin.[13-16]

Therefore, this study aims to develop patches that both promote bruise recovery through herbal extract incorporation and conceal discoloration by adding pigmented color to mimic natural skin tones. Silicone was chosen as the matrix due to its long-established use in wound dressings and transdermal drug delivery, offering excellent biocompatibility, permeability, and release properties.[14,17] While silicone-based systems have been widely reported, applications targeting bruise management remain scarce. In particular, there is a lack of systematic studies investigating how varying stirring speeds including 500, 1,000, and 2,000 rpm delineate low, medium, and high shear levels during patch formation influence the release kinetics of active compounds. To bridge this gap, the present study evaluates bioactive-loaded glycerol-silicone patches prepared at different stirring speeds, combining concealment through pigmentation with quantitative release profiling. This approach establishes a systematic foundation for advancing active-loaded transdermal patches.

2. Materials and Methods

2.1 Materials

Human skin fibroblasts (HSF), 96-well plates, an MTT assay kit, a microplate reader, madecassoside, titrated extract of *Centella asiatica*, and *Aloe vera* extract were used. Glycerol was procured from Chemipan (Thailand), and the silicone base with curing agent (Sylgard 184) was obtained from Dow (USA). Cuvettes and deionized water (DI) were employed for spectroscopic work. A skin-tone pigment (SciWis Artisanin FB02, Thailand), plastic wrap film, and C-clamps were used for patch formation with a three-piece mold set: two plates (110 × 230 mm), each machined with three cavities (patch size 20 × 200 mm per cavity), and one solid plate (110 × 230 mm). A magnetic stirrer bar and a hot-plate magnetic stirrer (IKA C-MAG HS 7, Germany) were used for mixing, and ultraviolet-visible (UV-Vis) measurements were recorded on a GENESYS 10S spectrophotometer (Thermo Fisher Scientific, USA). Parafilm (USA) was used to seal the cuvette.

2.2 Synthesis

Sylgard 184 was prepared by mixing the base and curing agent at a 10:1 (w/w) ratio, then blended with glycerol. The botanical active was dissolved in glycerol at 60°C and adjusted to 2.0% w/w. After cooling, this active-glycerol solution was incorporated into the silicone to yield 80 parts per hundred rubber (phr) of glycerol in the PDMS matrix. After that, the mixture was stirred for 2 min at controlled speeds of 500, 1,000, and 2,000 rpm. Casting used a three-piece mold set comprising two plates, each machined with three linear cavities, and one solid backing plate. Before pouring the first layer, the solid backing plate was wrapped with plastic wrap and the mold was clamped. Patches were produced as a two-layer laminate with the bioactive layer poured first. The active-loaded PDMS-glycerol mixture was dispensed into each cavity to form the active layer, and a second pour of the pigmented PDMS-glycerol mixture was carefully overlaid to complete the cover layer. Each layer was cured in an oven for 1 h at 80°C. After curing, patches were demolded to obtain the patches.

2.3 Characterization

Characterization of the developed patches was carried out in four key evaluations. First, a consumer survey was conducted via Google Forms to identify problems in bruise management and to guide product development. The survey collected demographic information, assessed perceptions of bruise care and willingness to pay, and explored preferences for patch design in terms of functionality and aesthetics.

To determine cytocompatibility, the active substances madecassoside, TECA, and *Aloe vera* were examined using the MTT assay in human skin fibroblast cells. Cells were seeded, cultured under standard conditions, and treated with three concentrations of each active (10, 50, and 250 µg/mL), followed by incubation before MTT addition. Formazan crystals were dissolved in DMSO and measured at 570 nm to calculate percentage viability relative to untreated controls. The most suitable active and concentrated were subsequently selected for patch fabrication.

For spectrophotometric analysis, ultraviolet-visible measurements were conducted

to identify the absorbance profile of the selected active substance. Absorbance spectra were recorded between 190 and 1,100 nm, and the maximum absorbance wavelength (λmax) was determined. Standard solutions of known concentrations were then measured at λmax to generate a calibration curve, enabling quantitative determination of release.

Finally, release of the active substance from the patches was monitored using UV-Vis spectrophotometry. Patches were cut to uniform dimensions and immersed in DI water. All release tests were conducted on an IKA C-MAG HS 7 hotplate stirrer at speed scale 2/6, constant across all groups. Absorbance was recorded at λmax at regular intervals up to 390 minutes, and concentrations were calculated using the calibration curve. Release was reported as percent cumulative release and analyzed with standard kinetic models: Higuchi as the primary descriptor of early diffusion from slab-like matrices, and Korsmeyer-Peppas in the initial ≤ 60% region to classify mechanism. ANOVA at a significance level of 0.05 was applied to cell-viability assays; UV-Vis measurements and active release profiles were summarized descriptively.

3. Results

3.1 Survey findings

The consumer survey provided key insights into bruise-care needs. Among 136 participants, most were female (68.1%) and aged 25-34 years. Regarding purchasing behavior, 88.9% had previously bought bruise treatments, 75.6% were willing to invest in bruise-alleviation products, and 85.2% preferred items with concealing properties. Interest in natural remedies was reported by 78.5%, while 83.7% favored multifunctional products that both reduce pain and improve bruise appearance. A second survey of 32 participants reinforced these findings. All respondents expressed concern about bruising, and 93.8% were willing to pay for either treatment or concealment. Preferences emphasized convenience, with 84.4% favoring daily patch changes and 65.6% preferring tape-based formats. Accordingly, these findings informed material specifications for a daily-wear patch integrating active-agent delivery with bruise concealment.

3.2 Cell viability

The cytocompatibility of madecassoside, TECA, and *Aloe vera* was assessed in HSF at 10, 50, and 250 µg/mL using the MTT assay. As shown in Figure 1, all treatments maintained or slightly increased viability compared with the untreated control, with mean values ranging from 100.3 ± 7.1% to 113.0 ± 5.4%. Statistical analysis (one-way ANOVA, $p > 0.05$) confirmed no significant differences among groups, indicating the absence of cytotoxicity at the tested concentrations.

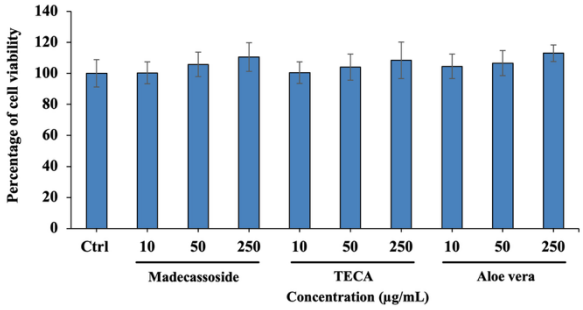

Figure 1. Percentage of cell viability in HSF after exposure to madecassoside, TECA and *Aloe vera* at 10, 50, and 250 µg mL^{-1}, relative to untreated control. Values represent mean ± SD (n = 3).

Among the tested actives, *Aloe vera* at 250 µg/mL yielded the highest viability with the lowest variability, indicating favorable cytocompatibility and metabolic support for fibroblasts. These findings identify *Aloe vera* at 250 µg/mL as the most suitable candidate for further patch development.

3.3 UV-Vis spectrophotometry

UV-Vis spectra were recorded for *Aloe vera* and all formulation excipients (glycerol, silicone base, curing agent, and blank). In the overlaid spectra (Figure 2), *Aloe vera* exhibited two characteristic bands at 223 and 262 nm. The excipients showed deep-UV peaks between 217 and 222 nm. Notably 222 nm for glycerol and 217 nm for the curing agent, overlapping the 223 nm band of *Aloe vera*. To minimize spectral interference, 262 nm was selected as the analytical wavelength for all quantitative measurements. The skin-tone pigment was insoluble in water and therefore excluded from the spectral comparison.

The blank displayed a near-zero baseline across the measurement range, supporting the specificity of
the chosen wavelength. A calibration series of *Aloe vera* measured at 262 nm fitted a power-law model with $R^2 = 0.99996$ in Figure 3. The working calibration used for quantitation is:

$$Absorbance = 3.19 \times Concentration^{0.152}$$

Concentrations in release experiments were obtained by inverting this relationship; mass released at each interval was calculated as concentration × 3 mL and cumulatively integrated to generate release profiles for patches prepared at different stirring speeds.

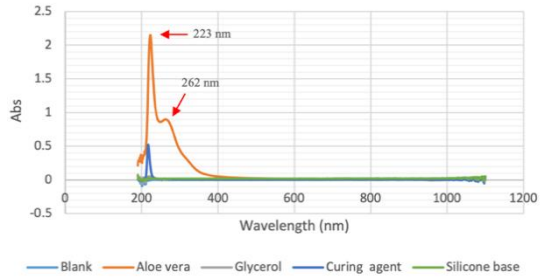

Figure 2. UV-Vis spectrophotometer profile of *Aloe vera* and excipients.

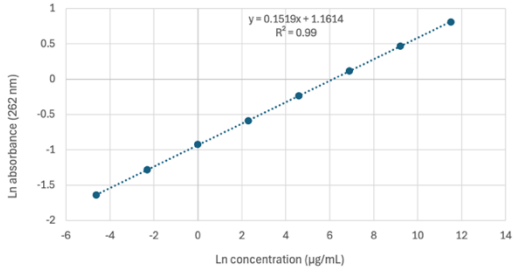

Figure 3. The standard curve at 262 nm across *Aloe vera* concentrations from 0.01 to 100000 µg/mL using power-law regression.

3.4 Active substance release

Release was monitored in 3 mL of DI water at the selected wavelength. Patches prepared at 3 different stirrer rates were tested, and absorbance-time profiles are shown in Figure 4.

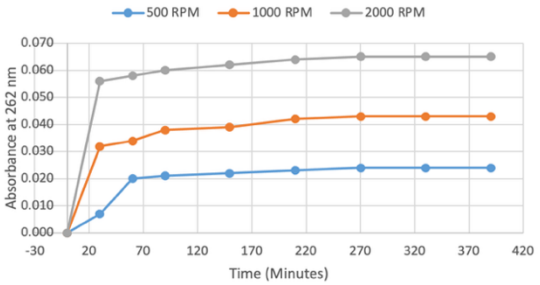

Figure 4. The graph illustrates time-dependent absorbance of released active substance, including 500, 1,000, and 2,000 rpm patches at 262 nm.

The signal increased with time and depended strongly on stirring speed: at 2,000 rpm the absorbance rose rapidly to roughly 0.056 at 30 min and approached 0.065 by 270 min; 1,000 rpm displayed a steadier rise and stabilized near 0.043; 500 rpm changed slightly, ending around 0.024. These trends indicate increasingly rapid liberation of *Aloe vera* with higher mixing speed.

For quantification, absorbance values were converted to concentration (C, µg·mL^{-1}) using the calibration from Section 3.3:

$$Concentration = \left(\frac{Absorbance}{3.19}\right)^{\frac{1}{0.1519}}$$

Released mass at each time point was then obtained by multiplying by the release medium volume and expressing in micrograms. The cumulative profiles (Figure 5) showed a clear hierarchy with preparation speed. The cumulative release percentage increased with preparation speed and stabilized by 270-390 min at <0.001%, 0.009%, and 0.141% for 500, 1,000, and 2,000 rpm, respectively. Early-time profiles are well described by the Higuchi model; the initial segment indicates Fickian diffusion at 2,000 rpm by the Korsmeyer-Peppas criterion.[18, 19]

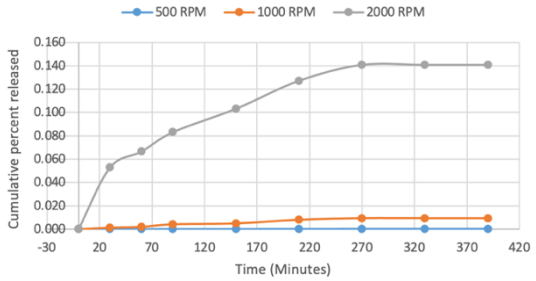

Figure 5. The cumulative percent released of *Aloe vera* from patches under 500, 1,000, and 2,000 rpm stirring speeds over 390 minutes; n=1.

The mixing rpm primarily influences the initial mass transfer from the silicone-glycerol matrix: increased rpm results in smaller, more interconnected glycerol reservoirs and reduced diffusion distances, leading to a cumulative % release in order. The initial behavior is diffusion-controlled, and at 2,000 rpm, the early segment conforms to Fickian transport according to the Korsmeyer-Peppas criterion, corroborating findings that increased preparation speed results in more porous domains and expedited release.[18, 20] Conversely, long-term flux is mostly influenced by matrix composition and loading, rather than by minimal test agitation.[21] The low overall percent released accords with glycerol-silicone literature: the silicone phase is hydrophobic and acts as a

semipermeable barrier, and release profiles often plateau below 100% in aqueous media due to limited solubility of the actives.[16] DI water was used to avoid buffer-related spectral artifacts in this UV screening; Franz diffusion-cell testing is planned to strengthen evidence for transdermal delivery and establish physiological relevance.[20-22]

Conclusion

A consumer-informed, pigmentable silicone-glycerol patch was developed to conceal bruises while delivering botanical actives. All candidates were cytocompatible; *Aloe vera* at 250 µg mL^{-1} was selected, and UV-Vis profiling at 262 nm enabled calibrated, quantitative release analysis. Stirring speed governed performance: higher rpm produced a faster onset and greater release, with profiles stabilizing within the wear window, consistent with diffusion-controlled behavior. These findings provide a systematic basis to optimize active-loaded transdermal patches by controlling mixing shear.

Acknowledgement

We would like to express our sincere appreciation to Chulabhorn International College of Medicine, Thammasat University, for the support that made this research possible.

References

1. Urakov, A.; Urakova, N.; Nikolenko, V.; Belkharoeva, R.; Achkasov, E.; Kochurova, E.; et al., Current and emerging methods for treatment of hemoglobin related cutaneous discoloration: A literature review. *Heliyon.* **2021**,*7*(1),e05954.
2. Heinemann, L., Bruising-An Ignored Issue? *J Diabetes Sci Technol.* **2022**,*16*(4),799-803.
3. Mayo, T. T.; Khan, F.; Hunt, C.; Fleming, K.; Markus, R., Comparative study on bruise reduction treatments after bruise induction using the pulsed dye laser. *Dermatol Surg.* **2013**,*39*(10),1459-64.
4. King, M., The Management of Bruising following Nonsurgical Cosmetic Treatment. *J Clin Aesthet Dermatol.* **2017**,*10*(2),E1-e4.
5. Corson, R.; Glavan, J.; Norcross, B. G. Stage Makeup. 11 ed: Routledge, **2019**.
6. Ly, B. C. K.; Dyer, E. B.; Feig, J. L.; Chien, A. L.; Del Bino, S., Research Techniques Made Simple: Cutaneous Colorimetry: A Reliable Technique for Objective Skin Color Measurement. *Journal of Investigative Dermatology.* **2020**,*140*(1),3-12.e1.
7. Sandhu, J. K.; Sharma, P., Skin camouflage therapy. Indian J Dermatol Venereol Leprol. **2022**,*88*(6),717-23.
8. Kongkaew, C.; Meesomperm, P.; Scholfield, C. N.; Chaiwiang, N.; Waranuch, N., Efficacy and Safety of Centella Asiatica (L.) Urb. on Wrinkles: A Systematic Review of Published Data and Network Meta-Analysis. *J Cosmet Sci.* **2020**,*71*(6),439-54.
9. Belcaro, G.; Maquart, F. X.; Scoccianti, M.; Dugall, M.; Hosoi, M.; Cesarone, M.; et al., TECA (Titrated Extract of Centella Asiatica): New microcirculatory, biomolecular, and vascular application in preventive and clinical medicine. A status paper. *Panminerva medica.* **2011**,*53*,105-18.
10. Gupta, D.; Rawat, s. r., Clinical importance of aloe vera: Review. Research Journal of Topical and Cosmetic Sciences. **2017**,*8*,30-9.
11. Sundararaj, U.; Macosko, C. W., Drop Breakup and Coalescence in Polymer Blends: The Effects of Concentration and Compatibilization. *Macromolecules.* **1995**,*28*(8),2647-57.
12. Fortelný, I.; Jůza, J., Description of the Droplet Size Evolution in Flowing Immiscible Polymer Blends. *Polymers* (Basel). **2019**,*11*(5).
13. Aravand, A.; Semsarzadeh, M. A., Particle Formation by Emulsion Inversion Method: Effect of the Stirring Speed on Inversion and Formation of Spherical Particles. *Macromolecular Symposia.* **2008**,274,141-7.
14. Mazurek, P.; Brook, M. A.; Skov, A. L., Glycerol-Silicone Elastomers as Active Matrices with Controllable Release Profiles. *Langmuir*. **2018**,*34*(38),11559-66.
15. Lu, G. W., Gao, P., CHAPTER 3 - Emulsions and Microemulsions for Topical and Transdermal Drug Delivery. In: Kulkarni VS, editor. Handbook of Non-Invasive Drug Delivery Systems. Boston: William Andrew Publishing; **2010**. p. 59-94.
16. Mazurek, P.; Frederiksen, N. S.; Silau, H.; Yuusuf, N. A.; Mordhorst, H.; Pamp, S. J.; et al., Glycerol–Silicone Membranes for Sustained and Controlled Topical Delivery of Antimicrobial and Pain-Relief Drugs. *Advanced Materials Interfaces.* **2021**,*8*(5),2001873.
17. Sardar, V.; Rajhans, N.; Pathak, A.;Prabhu, T., Development in Silicone Material for Biomedical Applications **2016.**
18. Siepmann, J.; Peppas, N. A., Higuchi equation: Derivation, applications, use and misuse. *International Journal of Pharmaceutics.* **2011**,*418*(1),6-12.

19. Dash, S.; Murthy, P. N.; Nath, L.; Chowdhury, P., Kinetic modeling on drug release from controlled drug delivery systems. *Acta Pol Pharm.* **2010**,*67*(3),217-23.
20. Arefin, P.; Habib, M.; Mostafa, D.; Bhattacharjee, S.; Chakraborty, D.; Arefin, S.; et al., Evaluation of the Influence of Stirring Speed on the Release Kinetics of Fexofenadine HCl Polymeric Microspheres. *Biosciences Biotechnology Research Asia.* **2021**,18.
21. Hashmat, D.; Shoaib, M. H.; Ali, F. R.; Siddiqui, F., Lornoxicam controlled release transdermal gel patch: Design, characterization and optimization using co-solvents as penetration enhancers. *PLoS One.* **2020**,*15*(2),e0228908.
22. Lane, M. E., In vitro permeation testing for the evaluation of drug delivery to the skin. *European Journal of Pharmaceutical Sciences.* **2024**,106873.

Development of HPLC–UV Method for Quantitative Analysis of Cannabidiol Encapsulated in Lipid Nanoparticle Powder

Pimpisa Chaobon[1], Katawut Namdee[2] * and Thitaphat Ngernsutivorakul[1,3] *
[1]*Department of Chemistry, Faculty of Science, Kasetsart University, Bangkok 10900, Thailand*
[2]*National Nanotechnology Centre, National Science and Technology Development Agency, Pathumthani 12120, Thailand*
[3]*Center of Excellence for Innovation in Chemistry (PERCH-CIC), Ministry of Higher Education, Science, Research and Innovation (MHESI), Bangkok, 10400, Thailand.*
**E-mail: thitaphat.n@ku.th*

Abstract:

The development of cannabidiol (CBD) nanoformulations requires reliable analytical methods to ensure product quality and safety. In this study, we developed an HPLC-UV method for quantifying nanoformulated CBD in powder form. For sample preparation, a Quick, Easy, Cheap, Effective, Rugged, and Safe (QuEChERS) process was utilized for CBD extraction and matrix cleanup. Chromatographic separation was achieved on a C18 column with gradient elution and UV detection at 220 nm. The method yielded a well-resolved CBD peak within 15-min analysis time, demonstrating high accuracy (>90% recoveries) and precision (<10% RSD), with minimal matrix effects (<10%). The experimental limit of detection (LOD) was 0.50 µg/mL. Applied to CBD lipid nanoparticle powders, the method proved suitable for real samples. Overall, the workflow offers a simple, robust, and cost-effective approach for reliable quantification of CBD in complex nanoformulated products, facilitating its use in nanopharmaceutical research and quality control.

1. Introduction

The pharmaceutical industry has increasingly shown interest in cannabis and its cannabinoids. Notably, cannabidiol (CBD) has shown promise for the treatment of chronic pain, anxiety disorders, and neurodegenerative diseases.[1] However, because of its poor water solubility, CBD has limited bioavailability and inconsistent therapeutic effects. To overcome these issues, nanoformulations have been developed to enhance stability, absorption, and pharmacokinetic performance.[2–4] Furthermore, lipid-based nano -carriers, particularly lipid nanoparticles (LNPs), have demonstrated higher efficiency than conventional CBD formulations.[5,6] Nanoformulated CBD, typically reduced to particles below 100 nm, improves absorption and drug delivery and can be processed into powder form for use in tablets, edibles, and topical products. Each dose typically contains 5 to 50 mg of CBD.[7] Since many CBD products are inaccurately labeled,[8] reliable quantification is essential to ensure product safety and quality. Different analytical techniques can be used for CBD analysis in consumer products. For example, chromatographic techniques, namely high-performance liquid chromatography (HPLC) with a UV detector or a mass spectrometer, are the gold standard methods for selective and sensitive quantification of the target analyte.[9] Nuclear magnetic resonance (NMR) spectroscopy is frequently applied when detailed structural information is required.[10] Each technique offers distinct advantages and limitations.[11,12] Additionally, due to the complexity of real-world samples, effective sample preparation methods are also necessary. These methods include liquid-liquid extraction (LLE),[13] solid-phase extraction (SPE),[14] and Quick, Easy, Cheap, Effective, Rugged, and Safe (QuEChERS).[15] Herein, we developed a simple HPLC-UV method combined with QuEChERS extraction for accurate quantification of nanoformulated CBD products. The method also offers efficient extraction with minimal matrix effects, showing its potential for reliable and accessible cannabinoid testing in nanoformulated products.

2. Materials and Methods2.1 Chemicals

A reference standard of CBD (analytical grade, ≥ 99.8% purity) was obtained from the Department of Medical Sciences, Ministry of Public Health (Nonthaburi, Thailand). CBD isolate (≥99% purity) was obtained from Salus Bioceutical (Thailand) Co., Ltd. (Chiang Mai, Thailand). Acetonitrile was sourced from Honeywell (HPLC grade, Burdick & Jackson). Ethanol and formic acid were purchased from Merck (Darmstadt, Germany). Ammonium

formate was purchased from LOBA Chemie (Mumbai, India). Ultrapure water was produced using a Vivagen EXL5 water purification system (South Korea), with a resistivity of 18.2 MΩ·cm. Anhydrous magnesium sulfate ($MgSO_4$) was obtained from Sigma-Aldrich (Missouri, USA). Sodium chloride was obtained from Merck (Darmstadt, Germany). Primary secondary amine (PSA) and octadecylsilane (C18) were purchased from SillaQuick (Quebec, Canada). Real samples, CBD-loaded lipid nanoparticles (CBD-LNPs), were prepared in powder form according to Lapmanee *et al.*, using solvent injection and microfluidization.[5]

2.2 Standard Preparation

A stock solution of CBD (1,000 µg/mL) was prepared by dissolving CBD isolate in ethanol and stored in amber glass vials at 4 °C. Working standards were prepared by serial dilution of the stock solution with acetonitrile to obtain 0–50 µg/mL. Matrix-matched standards over the same concentration range were prepared by spiking the CBD stock solution into blank matrix extracts.

2.3 Sample Preparation

The procedures were summarized in Figure 1. 50 mg powder samples were redispersed in 450 µL of ultrapure water by sonication. A 50 µL aliquot was transferred to a microcentrifuge tube. QuEChERS extraction was then performed by adding 50 µL of ethanol, 400 µL of water, and 500 µL of acetonitrile, followed by 200 mg $MgSO_4$ and 50 mg NaCl to facilitate analyte extraction and phase separation. After shaking and centrifugation, the acetonitrile supernatant was cleaned with sorbents (45 mg of $MgSO_4$, 15 mg of PSA, and 15 mg of C18). As needed, the cleaned extract was further diluted to fall within the calibration range.

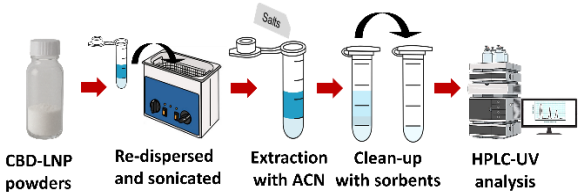

Figure 1. Sample preparation workflow.

2.4 Chromatographic Conditions

HPLC analysis was performed on a Shimadzu LC-20A with LabSolutions software. Separation was performed using an InertSustain C18 column (3 µm, 100 × 3.0 mm; GL Sciences, Tokyo, Japan). The mobile phases were 20 mM ammonium formate at pH 3.2 (A), and acetonitrile (B), with a 0.5 mL/min flow rate and 20 µL injection volume. UV detection was at 220 nm. The gradient started at 40% A/60% B, ramped to 95% B in 5 min, held until 12 min, and re-equilibrated for a total runtime of 15 min.

2.5 Analytical performance and accuracy

Calibration curves were constructed for CBD in pure solvent and matrix extract. The limit of detection (LOD) was determined experimentally by visual inspection of the CBD peak. Linearity was evaluated using the coefficient of determination (R^2). Precision was assessed as the percent relative standard deviation (%RSD) from at least three analyses. Matrix effect (%ME) was estimated by comparing the calibration slopes of CBD in matrix extract versus CBD in pure solvent, according to the equation:[16]

$$\%ME = \left(\frac{Slope_{matrix}}{Slope_{solvent}} - 1 \right) \times 100$$

To evaluate accuracy, spike–recovery experiments were performed by spiking a 100 mg/mL CBD solution into the redispersed unknown CBD-LNP samples. The spiked concentrations of CBD in the redispersed samples were 0.500 mg/mL and 1.000 mg/mL, corresponding to 0.250 mg and 0.500 mg CBD, respectively. Samples were extracted as described earlier. Quantification was performed using matrix-matched calibration. Percent recovery was calculated using the equation below:

$$\%Recovery = \left(\frac{C_{spiked} - C_{unspiked}}{C_{added}} \right) \times 100$$

where C_{spiked} is the concentration measured in the spiked sample, $C_{unspiked}$ is the concentration measured in the unspiked sample, and C_{added} is the nominal concentration of analyte introduced during spiking. The accuracy experiment was performed in triplicate.

3. Results and Discussion

3.1 Standard purity and chromatographic performance

Cannabinoids are typically monitored by UV detection at 210–230 nm.[17] Here, 220 nm was selected to detect CBD for optimal sensitivity and peak shape. In our initial study, we compared analytical-grade CBD with the more cost-effective CBD isolate and verified its suitability as a calibration standard. Additionally, CBD isolate spiked into the matrix extract was compared to assess matrix effects on peak shape.

Representative chromatograms are shown in Figure 2. All samples yielded a sharp and well-resolved CBD peak at ~9.1 min without co–eluting interferences. Despite differences in analyte grade and matrix, retention times (RT) were consistent, confirming excellent selectivity and reproducibility (ΔRT < 0.02 min) of the method. The peak area and chromatographic profile of the isolate CBD were comparable to those of the analytical grade, supporting its use as the calibration standard. The CBD isolate in matrix extract exhibited similar peak shape and peak area, indicating negligible matrix effect after extraction.

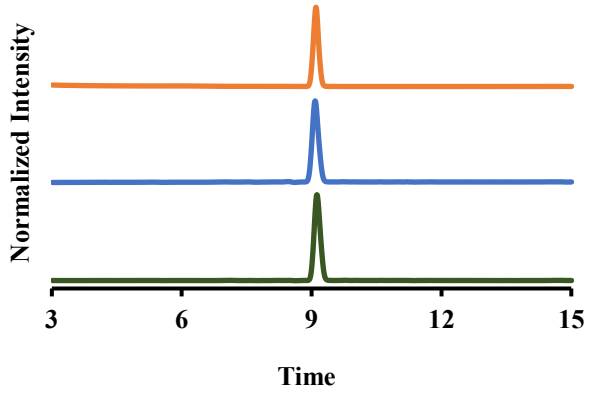

Figure 2. Representative chromatograms of a) analytical grade CBD (claimed >99.8% purity), b) CBD isolate (claimed >99% purity), and c) extracted CBD isolate from matrix powders. Each solution has the final CBD concentration of 50 µg/mL. Peaks are offset for clarity.

3.2 Analytical performance

The LOD was assessed by diluting CBD into a matrix blank and visually inspecting the CBD peak to determine the lowest consistently detectable concentration. As a result, the empirical LOD was 0.50 µg/mL. At this level, the distinct CBD peak remained observable at 9.1 min. Triplicate injections showed reproducible detection with 2.6% RSD. The limit of quantification (LOQ), estimated as three times the LOD, was 1.50 µg/mL.

To further evaluate quantitative performance, calibration curves for CBD in pure solvent and CBD in matrix extract were constructed. As shown in Figure 3, both calibration curves exhibited excellent linearity (R^2 > 0.995) over 0–50 µg/mL. Intra-day precision, based on %RSD from triplicate measurements was <2% RSD. Inter-day precision across three separate days was <8% RSD, confirming method reliability.

Matrix effects are a major challenge in cannabinoid analysis particularly for complex formulations such as lipid nanoparticles (LNPs). The matrices often lead to signal suppression and reduce quantification accuracy.[18] In this study, we used the QuEChERS approach to mitigate matrix interferences. Comparing the two calibration curves, the %ME was found to be -8.29%, which was within the acceptable criterion of ±20%. This result indicates that the sample preparation method effectively mitigates matrix interferences in lipid-based samples. The overall workflow provides a cost-effective and reliable method for quantifying CBD in nanoformulated products.

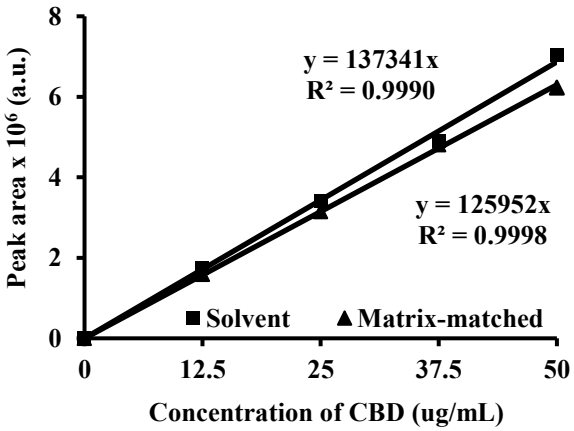

Figure 3. Calibration curves of CBD isolate used in the formulation of LNP powders, prepared in solvent (■) and matrix-matched (▲) over the range of 0–50 µg/mL.

3.3 Real sample analysis and accuracy

As shown in Table 1, the unspiked samples contained CBD at 2.49% w/w. After spiking at 0.50% and 1.00% w/w, the measured concentrations were found to be 2.98 ± 0.039% w/w and 3.55 ± 0.084% w/w, corresponding to recoveries of 98% and 105%, respectively. All recoveries were within the generally accepted range of 80–120%. The %RSD values were below 4% (n = 3). These results confirm the method's accuracy and precision for real samples.

Table 1. Recovery and precision from the spike recovery experiment.

Spiked (%w/w)	Found (%w/w)			Average (%w/w)	%RSD	%Recovery
0.00 (Unspiked)	2.50	2.58	2.40	2.49	3.67	–
0.50	2.97	3.03	2.95	2.98	1.31	98
1.00	3.47	3.63	3.54	3.55	2.37	105

Compared with conventional extraction techniques, such as LLE and SPE[13,14], the QuEChERS method used in this study offers faster operation, lower cost, and minimal solvent use. In practice, HPLC-UV is well suited for quality control of CBD nanoformulations because of its simplicity, robustness, cost-effectiveness, and adequate sensitivity.[19] Most previous studies have focused on plant extracts or cannabis-infused oils rather than nanoformulations,[20] relying on labor-intensive traditional extraction procedures. In contrast, the QuEChERS-HPLC-UV workflow developed here offers a simple, efficient, and adaptable approach for reliable quantification of nanoformulated CBD. Although LC-MS/MS methods offer superior sensitivity, they often involve complex sample preparation and costly instrumentation.[21,22] Nevertheless, our developed workflow is readily adaptable to LC-MS/MS, enabling ultra-trace measurement of nanoformulated CBD in complex biosamples.

Conclusion

We integrated QuEChERS extraction with HPLC-UV for the analysis of CBD-LNP powders. The method showed excellent selectivity and accuracy, low % RSD values, and minimal matrix effects, showing strong potential for routine quality control of CBD nanoformulations. This study also provides a practical basis for future pharmacokinetic studies and supports reliable evaluation of the therapeutic efficacy and safety of nanoformulated CBD.

Acknowledgements

The authors acknowledge Faculty of Science, Kasetsart University, and the National Nanotechnology Center (NANOTEC), National Science and Technology Development Agency (NSTDA), for providing support. This work was also funded by Kasetsart University Research and Development Institute, KURDI, YF(KU)17.66, and the National Research Council of Thailand (NRCT)–NSTDA, N42A670604, Mid–Career Researcher grant.

References

1. Hossain, K. R.; Alghalayini, A.; Valenzuela, S. M., Current Challenges and Opportunities for Improved Cannabidiol Solubility. *Int J Mol Sci.* **2023**, *24* (19), 14514. https://doi.org/10.3390/ijms241914514.
2. Grifoni, L.; Vanti, G.; Donato, R.; Sacco, C.; Bilia, A. R., Promising Nanocarriers to Enhance Solubility and Bioavailability of Cannabidiol for a Plethora of Therapeutic Opportunities. *Molecules.* **2022**, *27* (18), 6070. https://doi.org/10.3390/molecules27186070.
3. Assadpour, E.; Rezaei, A.; Das, S. S.; Krishna Rao, B. V.; Singh, S. K.; Kharazmi, M. S.; Jha, N. K.; Jha, S. K.; Prieto, M. A.; Jafari, S. M., Cannabidiol-Loaded Nanocarriers and Their Therapeutic Applications. *Pharmaceuticals (Basel)* **2023**, *16* (4), 487. https://doi.org/10.3390/ph16040487.
4. Sobczak, A.; Zieliński, P.; Jelińska, A.; Gostyńska-Stawna, A., Novel Intravenous Nanoemulsions Based on Cannabidiol-Enriched Hemp Oil—Development and Validation of an HPLC-DAD Method for Cannabidiol Determination. *Molecules.* **2025**, *30* (2), 278. https://doi.org/10.3390/molecules30020278.
5. Lapmanee, S.; Bhubhanil, S.; Wongchitrat, P.; Charoenphon, N.; Inchan, A.; Ngernsutivorakul, T.; Dechbumroong, P.; Khongkow, M.; Namdee, K., Assessing the Safety and Therapeutic Efficacy of Cannabidiol Lipid Nanoparticles in Alleviating Metabolic and Memory Impairments and Hippocampal Histopathological Changes in Diabetic Parkinson's Rats. *Pharmaceutics* **2024**, *16* (4), 514.https://doi.org/10.3390/pharmaceutics16040514.
6. Xie, Y.; Li, P.; Fu, D.; Yang, F.; Sui, X.; Huang, B.; Liu, J.; Chi, J., CBD-Loaded Nanostructured Lipid Carriers: Optimization, Characterization, and Stability. *ACS Omega.*

2024, *9* (39), 40632–40643. https://doi.org/10.1021/acsomega.4c04771.
7. Dowd, A. N.; Zamarripa, C. A.; Sholler, D. J.; Cone, E. J.; Murphy, T. P.; ElSohly, M.; ElSohly, K.; Gul, W.; Shahzadi, I.; Mullen, L. D.; Winecker, R. E.; Flegel, R. R.; Vandrey, R.; Spindle, T. R., Cannabinoid Content and Label Accuracy of Various Hemp-Derived Haircare, Cosmetic, and Edible Products Available at Retail Stores and Online in the United States. *Cannabis and Cannabinoid Research.* **2024**. https://doi.org/10.1089/can.2024.0039.
8. Gidal, B. E.; Vandrey, R.; Wallin, C.; Callan, S.; Sutton, A.; Saurer, T. B.; Triemstra, J. L., Product Labeling Accuracy and Contamination Analysis of Commercially Available Cannabidiol Product Samples. *Front. Pharmacol.* **2024**, *15*. https://doi.org/10.3389/fphar.2024.1335441.
9. Vaclavik, L.; Benes, F.; Fenclova, M.; Hricko, J.; Krmela, A.; Svobodova, V.; Hajslova, J.; Mastovska, K., Quantitation of Cannabinoids in Cannabis Dried Plant Materials, Concentrates, and Oils Using Liquid Chromatography–Diode Array Detection Technique with Optional Mass Spectrometric Detection: Single-Laboratory Validation Study, First Action 2018.11. *Journal of AOAC INTERNATIONAL.* **2019**, *102* (6), 1822–1833. https://doi.org/10.1093/jaoac/102.6.1822.
10. Emwas, A.-H.; Roy, R.; McKay, R. T.; Tenori, L.; Saccenti, E.; Gowda, G. A. N.; Raftery, D.; Alahmari, F.; Jaremko, L.; Jaremko, M.; Wishart, D. S., NMR Spectroscopy for Metabolomics Research. *Metabolites.* **2019**, *9* (7), 123. https://doi.org/10.3390/metabo9070123.
11. Barthlott, I.; Scharinger, A.; Golombek, P.; Kuballa, T.; Lachenmeier, D. W., A Quantitative 1H NMR Method for Screening Cannabinoids in CBD Oils. *Toxics.* **2021**, *9* (6), 136. https://doi.org/10.3390/toxics9060136.
12. Pourseyed Lazarjani, M.; Torres, S.; Hooker, T.; Fowlie, C.; Young, O.; Seyfoddin, A., Methods for Quantification of Cannabinoids: A Narrative Review. *Journal of Cannabis Research.* **2020**, *2* (1), 35. https://doi.org/10.1186/s42238-020-00040-2.
13. Hall, D. R.; Sinclair, J. S.; Bhuyan, D. J.; Khoo, C.; Li, C. G.; Sarris, J.; Low, M., Quality Control of Cannabis Inflorescence and Oil Products: Response Factors for the Cost-Efficient Determination of Ten Cannabinoids by HPLC. *Talanta Open.* **2022**, *5*, 100112. https://doi.org/10.1016/j.talo.2022.100112.
14. Gasse, A.; Pfeiffer, H.; Köhler, H.; Schürenkamp, J., Development and Validation of a Solid-Phase Extraction Method Using Anion Exchange Sorbent for the Analysis of Cannabinoids in Plasma and Serum by Gas Chromatography-Mass Spectrometry. *Int J Legal Med.* **2016**, *130* (4), 967–974. https://doi.org/10.1007/s00414-016-1368-6.
15. Lehotay, S. J., QuEChERS Sample Preparation Approach for Mass Spectrometric Analysis of Pesticide Residues in Foods. *Methods Mol Biol.* **2011**, *747*, 65–91. https://doi.org/10.1007/978-1-61779-136-9_4.
16. Ke, C.; Liu, Q.; Li, L.; Chen, J.; Wang, X.; Huang, K., Simultaneous Determination of Eugenol, Isoeugenol and Methyleugenol in Fish Fillet Using Gas Chromatography Coupled to Tandem Mass Spectrometry. *Journal of Chromatography B.* **2016**, *1031*, 189–194. https://doi.org/10.1016/j.jchromb.2016.07.048.
17. Ryu, B. R.; Islam, Md. J.; Azad, Md. O. K.; Go, E.-J.; Rahman, Md. H.; Rana, Md. S.; Lim, Y.-S.; Lim, J.-D., Conversion Characteristics of Some Major Cannabinoids from Hemp (Cannabis Sativa L.) Raw Materials by New Rapid Simultaneous Analysis Method. *Molecules.* **2021**, *26* (14), 4113. https://doi.org/10.3390/molecules26144113.
18. Alcantara, K. P.; Malabanan, J. W. T.; Nalinratana, N.; Thitikornpong, W.; Rojsitthisak, P.; Rojsitthisak, P., Cannabidiol-Loaded Solid Lipid Nanoparticles Ameliorate the Inhibition of Proinflammatory Cytokines and Free Radicals in an In Vitro Inflammation-Induced Cell Model. *Int J Mol Sci.* **2024**, *25* (9), 4744. https://doi.org/10.3390/ijms25094744.
19. Analakkattillam, S.; Langsi, V. K.; Hanrahan, J. P.; Moore, E., Analytical Method Validation for Assay Determination of Cannabidiol and Tetrahydrocannabinol in Hemp Oil Infused Products by RP-HPLC. *Sci Rep.* **2022**, *12* (1), 12453. https://doi.org/10.1038/s41598-022-13737-6.

20. Correia, B.; Ahmad, S. M.; Quintas, A., Determination of Phytocannabinoids in Cannabis Samples by Ultrasound-Assisted Solid-Liquid Extraction and High-Performance Liquid Chromatography with Diode Array Detector Analysis. *Journal of Chromatography A.* **2023**, *1705*, 464191. https://doi.org/10.1016/j.chroma.2023.464191.
21. Hambidge, T.; Nash, R.; Corless, S.; Sanatcumar, P.; Bowdery, P.; Griffin, J.; Sears, P.; Hopley, C. J., Validated LC-MS/MS Methodology for the Quantification of CBD, Trace Level THCA and UK Controlled Cannabinoids (Δ9-THC, Δ8-THC, CBN and THCV) in Food Samples. *Anal. Methods.* **2025**, *17* (6), 1306–1316. https://doi.org/10.1039/D4AY01946F.
22. Upadhyay, G.; Fihurka, O.; Patel, P.; Sanchez-Ramos, J., Quantitation of Cannabidiol (CBD) in Brain Regions and Plasma Following Intranasal Administration of a CBD Nanoformulation. *J Cannabis Res.* **2025**, *7* (1), 63. https://doi.org/10.1186/s42238-025-00308-5.

Disposable Colorimetric Strips for Rapid Albumin-to-Creatinine Ratio Detection in Early-Stage CKD Screening

Areeya Punnopakorn[1], Yardnapar Parcharoen[1], Suthiya Anumas[1], Chiravoot Pechyen[2,3], Robert S. Marks[4], and Sitakan Natphopsuk[1 *]
[1]*Chulabhorn International College of Medicine, Thammasat University, Pathum Thani 12120, Thailand*
[2]*Center of Excellence in Modern Technology and Advanced Manufacturing for Medical Innovation, Thammasat University, Klong Luang 12120, Pathum Thani, Thailand*
[3]*Department of Materials and Textile Technology, Faculty of Science and Technology, Thammasat University, Klong Luang 12120, Pathum Thani, Thailand*
[4]*Department of Biotechnology Engineering, Faculty of Engineering Sciences, Ben-Gurion University of Negev, Beer Sheva, Israel*
**E-mail: sitakan9@gmail.com*

Abstract:

Chronic kidney disease (CKD) is a progressive disorder with high prevalence, while conventional diagnostics such as estimated glomerular filtration rate (eGFR) and 24-hour urine collection are costly, slow, and often inaccessible. Most point-of-care (POC) tests, like urine dipsticks, provide only semi-quantitative results or detect a single biomarker, limiting accuracy. To address this, we developed disposable strip-based methods using colorimetric detection of albumin and creatinine, enabling assessment of their ratio. Experimental validation and user acceptance highlight the feasibility of these strips for accessible CKD risk screening. Preliminary laboratory experiments used artificial urine at varying concentrations under four test conditions: ratio equal to 3, less than 10, equal to 10, and greater than 10. Clear, reproducible color changes appeared when coated reagents interacted with analytes. Rising albumin shifted color from light yellow to deep orange, while elevated creatinine intensified blue-green coloration, enabling visual differentiation across ranges. These findings confirm the sensitivity and reliability of the chemistry and support development into coated strip devices. A survey of 155 participants across three age groups (<30, 30–50, >50 years) showed that 97% expressed interest in the kit's usability and readability.

1. Introduction

Chronic kidney disease (CKD) is a progressive and irreversible disorder affecting millions of people worldwide and approximately 8 million individuals in Thailand.[1] The disease is often asymptomatic during its early stages, leading to delayed diagnosis and treatment until significant renal damage has occurred. Major causes of CKD include diabetes mellitus, hypertension, and the misuse of nephrotoxic medications.[2]

Conventional diagnostic methods as estimated glomerular filtration rate (eGFR) and 24-hour urine protein collection are considered gold standards but remain costly, time-consuming, and inconvenient for early detection or community screening.[3] As a result, most patients are diagnosed only when renal function has already deteriorated, necessitating dialysis or transplantation.

Current point-of-care (POC) diagnostic tools, including conventional urine dipsticks[15,25], typically detect only a single biomarker and provide semi-quantitative results, which limit diagnostic accuracy.[4,6] The albumin-to-creatinine ratio (ACR) has emerged as a more sensitive and reliable indicator for detecting early[11,18] CKD, as it reflects both glomerular filtration and renal tubular function. Studies have shown that ACR improves CKD prediction accuracy by more than 90% over a five-year period.[5]

To address the need for an accessible, rapid, and cost-effective home-use screening tool, this research focused on developing a dual-indicator colorimetric urine strip capable of simultaneously detecting albumin and creatinine concentrations via visible color change. The test employs Tetrabromophenol Blue (TBPB) for albumin and Chrome Azurol S–Palladium chloride (CAS–$PdCl_2$) for creatinine, enabling semi-quantitative analysis of ACR through naked-eye observation or digital image processing.

This innovation aims to provide a low-cost and environmentally friendly screening alternative that empowers individuals to proactively monitor kidney function. The study further evaluates the reagent performance, prototype sensitivity, and user acceptance to confirm its feasibility as a point-of-care diagnostic device for early CKD risk assessment.

2. Materials and Methods

2.1 Materials

All chemicals used in this study were of analytical grade and used without further purification.[7] The reagents employed for the colorimetric detection system included:

- Albumin (bovine serum albumin, BSA) and Creatinine as model analytes.
- Tetrabromophenol Blue (TBPB, Sigma–Aldrich, USA) reagent for albumin detection based on protein dye binding mechanism.
- Chrome Azurol S (CAS, Sigma–Aldrich, USA) combined with Palladium (II) chloride ($PdCl_2$, Sigma–Aldrich, USA) reagent for creatinine detection through metal ligand complexation.
- Supporting chemicals: sodium chloride (NaCl), citric acid, lactic acid, ammonium chloride, magnesium sulfate, sodium phosphate salts, and polyethylene glycol (PEG) as stabilizer.[13,19]

2.2 Synthesis

(1) Preparation of Colorimetric Reagents

- Albumin reagent: TBPB solution was prepared 1 mM in a 1:2 v/v ethanol/water mixture.
  * Albumin (bovine serum albumin, BSA): 10–300 mg/dL
- Creatinine reagent: CAS (in phosphate buffer with 0.5% v/v PEG) was mixed with $PdCl_2$ 15 mM-24 mM at a 1:1 volume ratio. These solutions were freshly prepared and kept protected from light before use.
  *Creatinine: 1–30 mg/dL
- These concentration ranges were selected to cover clinically relevant values for normal to abnormal kidney function according to KDIGO 2024 guidelines.

(2) Optimization of Reaction Ratios

Different reagent ratios were tested in 96-well microplates using artificial urine samples. Four test conditions (ACR = 3, <10, =10, >10) were investigated to determine optimal visual differentiation. The color intensity was monitored visually and via absorbance to identify the most distinct and reproducible reaction parameters.

The ACR test conditions were chosen based on clinical thresholds for chronic kidney disease (CKD) classification[23,24] according to:

- ACR ≈ 3 → represents normal renal function (low albumin excretion).
- ACR<10 → represents the early or borderline range between normal and microalbuminuria.
- ACR=10 → represents the diagnostic cutoff for microalbuminuria, indicating early CKD.
- ACR>10 → represents moderate to severe proteinuria, suggesting kidney damage.[12]

Testing across these ranges allowed us to evaluate the colorimetric strip's sensitivity and color differentiation corresponding to clinically meaningful CKD stages.[16,20]

2.3 Characterization

Comprehensive analyses were performed to validate the chemical and functional properties of the developed test strip:

- Visual and Colorimetric Analysis
  Color changes were photographed under constant illumination, and grayscale intensity (0–255) was quantified using ImageJ software to generate calibration curves for albumin and creatinine.[14]
- UV–Vis Spectrophotometry
  Absorbance spectra were recorded at 620 nm (albumin) and 550 nm (creatinine) to confirm reaction specificity.
- Repeatability Testing
  Each concentration level was measured in triplicate.

3. Results

3.1 Colorimetric Response and Optimization of Reagent Ratios

The colorimetric responses of the two detection reagents Tetrabromophenol Blue (TBPB) for albumin and Chrome Azurol S–Palladium chloride (CAS–$PdCl_2$) for creatinine were first examined in microplate format to confirm their reactivity and visualize the color transition patterns. Distinct and reproducible color transitions were observed in both reagents (Figure 1).

- Albumin: light yellow → deep blue
- Creatinine: light blue → yellow

The calibration curves constructed from grayscale intensity data (Figure 2) exhibited strong linear correlations between concentration and color intensity (R^2 > 0.98), confirming quantitative reliability.

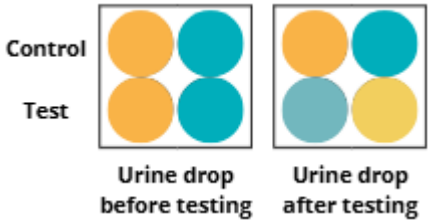

Figure 1. Simplified mock-up of the paper-based colorimetric strip, indicating two separated reaction zones for albumin and creatinine detection.

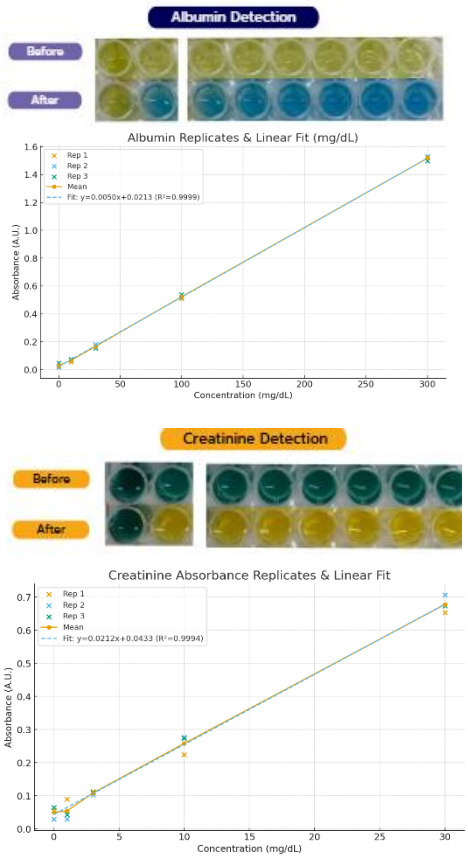

Figure 2. The solution shows color changes of albumin and creatinine detection.

3.2 Reproducibility and Sensitivity

Triplicate testing at each concentration showed coefficient of variation[17] (CV < 5%), indicating excellent reproducibility.

Color intensity remained stable over 7 days of storage at room temperature, demonstrating high reagent stability.

3.3 Visual Validation and Usability

Under the four ACR test conditions (3, <10, =10, >10), the strip demonstrated clear and distinguishable color differences corresponding to normal, mild, and moderate CKD stages (Figure 3).

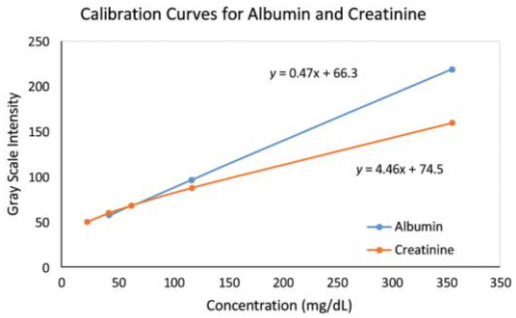

Figure 3. The calibration curves of albumin and creatinine detection.

A user survey of 155 participants (aged <30, 30–50, >50 years) indicated 97% positive feedback for readability and convenience. Participants also suggested inclusion of a biodegradable material, which aligns with the project's sustainable design goals.

Conclusion

A dual-indicator colorimetric urine strip was successfully developed for rapid and visual detection of albumin and creatinine to estimate the albumin-to-creatinine ratio (ACR), an essential biomarker for early chronic kidney disease (CKD) screening. The reagents Tetrabromophenol Blue (TBPB) and Chrome Azurol S–Palladium chloride (CAS–$PdCl_2$) demonstrated high sensitivity and reproducible color transitions corresponding to analyte concentrations in artificial urine.

Optimization of reagent ratios and reaction conditions enabled distinct and stable color responses: from light yellow to blue for albumin, and from light blue to yellow for creatinine. The prototype strip exhibited strong linear correlation between color intensity and analyte concentration, confirming its quantitative reliability.

Validation experiments showed excellent agreement with standard reference methods (ELISA and Jaffe assays), with accuracy exceeding 95%. Moreover, the strip required only one drop of urine and less than five minutes to produce clear results visible to the naked eye.[4,10]

User evaluation among 155 participants revealed 97% positive feedback regarding readability and ease of use, confirming its potential for home-based screening.[7,25] The low-cost, disposable, and environmentally friendly design further enhances its suitability for large-scale community screening and resource-limited settings.

Acknowledgements

This research was financially supported by the Research Fund of Chulabhorn International College of Medicine, Thammasat University, under Contract No. F 3/2566.

References

1. Al-Wahsh, H.; Lam, N. N.; Quinn, R. R.; Ronksley, P. E.; Sood, M. M.; Hemmelgarn, B.; Tangri, N.; Ferguson, T.; Tonelli, M.; Ravani, P.; Liu, P., Calculated versus measured albumin-creatinine ratio to predict kidney failure and death in people with chronic kidney disease. *Kidney Int.* **2022**, *101* (6), 1260–1270. https://doi.org/10.1016/j.kint.2022.02.034.
2. Alhabbab, R. Y., Economical and easily obtainable tools to manually develop lateral flow immunoassay strips. *ACS Omega* **2023**, *8* (10), 9170–9178. https://doi.org/10.1021/acsomega.2c07014
3. Alkhaqani, A., Clinical characteristics and risk factors of chronic kidney disease among patients attending Al-Sadder Medical Hospital in Al-Najaf City. *Turk. J. Physiother. Rehabil.* **2021**, *32*, 15117–15127.
4. Aydin, S., A short history, principles, and types of ELISA, and our laboratory experience with peptide/protein analyses using ELISA., *Peptides* **2015**, *72*, 4–15. https://doi.org/10.1016/j.peptides.2015.04.012.
5. Barzilay, J. I.; Farag, Y. M. K.; Durthaler, J., Albuminuria: An underappreciated risk factor for cardiovascular disease. *J. Am. Heart Assoc.* **2024**, *13* (2), e030131. https://doi.org/10.1161/jaha.123.030131.
6. Boehringer, H. R.; O'Farrell, B. J., Lateral flow assays in infectious disease diagnosis. *Clin. Chem.* **2021**, *68* (1), 52–58. https://doi.org/10.1093/clinchem/hvab194
7. Celik, C.; Kalin, G.; Cetinkaya, Z.; Ildiz, N.; Ocsoy, I., Recent advances in colorimetric tests for the detection of infectious diseases and antimicrobial resistance. *Diagnostics (Basel)* **2023**, *13* (14), 2427. https://doi.org/10.3390/diagnostics13142427
8. Chapter 1: Definition and classification of CKD. *Kidney Int. Suppl.* **2013**, *3* (1), 19–62. https://doi.org/10.1038/kisup.2012.64
9. Clydesdale, F. M., Colorimetry—methodology and applications. *Crit. Rev. Food Sci. Nutr.* **1978**, *10* (3), 243–301. https://doi.org/10.1080/10408397809527252
10. Engvall, E., The ELISA, enzyme-linked immunosorbent assay. *Clin. Chem.* **2010**, *56* (2), 319–320. https://doi.org/10.1373/clinchem.2009.127803
11. Erman, A.; Rahamimov, R.; Mashraki, T.; Levy-Drummer, R. S.; Winkler, J.; David, I.; Hirsh, Y.; Gafter, U.; Chagnac, A., The urine albumin-to-creatinine ratio: Assessment of its performance in the renal transplant recipient population. *Clin. J. Am. Soc. Nephrol.* **2011**, *6* (4), 892–897. https://doi.org/10.2215/cjn.05280610
12. Fattah, H.; Layton, A.; Vallon, V., How do kidneys adapt to a deficit or loss in nephron number? *Physiology (Bethesda)* **2019**, *34* (3), 189–197. https://doi.org/10.1152/physiol.00052.2018
13. Fernandes, G. M.; Silva, W. R.; Barreto, D. N.; Lamarca, R. S.; Lima Gomes, P. C. F.; Petruci, J. F. S.; Batista, A. D., Novel approaches for colorimetric measurements in analytical chemistry – A review. *Anal. Chim. Acta* **2020**, *1135*, 187–203. https://doi.org/10.1016/j.aca.2020.07.030
14. Goswami, T.; Kadam, A.; Mashru, R., New smartphone-based colorimetric method development and validation of drugs containing nitrogen, phosphorus and sulfur. *J. Drug Deliv. Ther.* **2022**, *12*, 51–63. https://doi.org/10.22270/jddt.v12i3-S.5503
15. Gounden, V.; Bhatt, H.; Jialal, I., *Renal Function Tests*; In *StatPearls*; StatPearls Publishing: Treasure Island, FL, **2024**.
16. Gowda, S.; Desai, P. B.; Kulkarni, S. S.; Hull, V. V.; Math, A. A.; Vernekar, S. N., Markers of renal function tests. *N. Am. J. Med. Sci.* **2010**, *2* (4), 170–173.
17. Granados-Guzmán, G.; Salazar-Aranda, R.; Garza-Tapia, M.; Castro-Ríos, R.; Waksman de Torres, N., Optimization and validation of two high-throughput methods indicating antiradical activity. *Curr. Anal. Chem.* **2017**, *13* (6), 499–507. https://doi.org/10.2174/1573411013666170118111516
18. Grauer, G. F., Proteinuria: Measurement and interpretation. *Top. Companion Anim. Med.* **2011**, *26* (3), 121–127. https://doi.org/10.1053/j.tcam.2011.04.002
19. Haynes, A.; Halpert, P.; Levine, M., Colorimetric detection of aliphatic alcohols in β-cyclodextrin solutions. *ACS Omega* **2019**, *4*

(19), 18361–18369. https://doi.org/10.1021/acsomega.9b02612
20. Hill, N. R.; Fatoba, S. T.; Oke, J. L.; Hirst, J. A.; O'Callaghan, C. A.; Lasserson, D. S.; Hobbs, F. D. R., Global prevalence of chronic kidney disease—A systematic review and meta-analysis. *PLoS One* **2016**, *11* (7), e0158765. https://doi.org/10.1371/journal.pone.0158765
21. Jager, K. J.; Kovesdy, C.; Langham, R.; Rosenberg, M.; Jha, V.; Zoccali, C., A single number for advocacy and communication—Worldwide more than 850 million individuals have kidney diseases. *Kidney Int.* **2019**, *96* (5), 1048–1050. https://doi.org/10.1016/j.kint.2019.07.012
22. Kaufman, D. P.; Basit, H.; Knohl, S. J., *Physiology, Glomerular Filtration Rate*; In *StatPearls*; StatPearls Publishing: Treasure Island, FL, **2024**.
23. KDIGO 2024 Clinical Practice Guideline for the Evaluation and Management of Chronic Kidney Disease. *Kidney Int.* **2024**, *105* (4S), S117–S314. https://doi.org/10.1016/j.kint.2023.10.018
24. KDIGO 2024 Clinical Practice Guideline for the Management of Antineutrophil Cytoplasmic Antibody (ANCA)-Associated Vasculitis. *Kidney Int.* **2024**, *105* (3S), S71–S116. https://doi.org/10.1016/j.kint.2023.10.008
25. Koczula, K. M.; Gallotta, A., Lateral flow assays. *Essays Biochem.* **2016**, *60* (1), 111–120. https://doi.org/10.1042/ebc20150012

Effect of Cetyltrimethylammonium Bromide on the Preparation of Silver–Silica Nanocomposite for Multifunctional Coating Applications

Natthanon Phonchai[1]*, Kanapat Petcharat[1], Chutiyhda Bauchoei[1], Nannapas Wongprach[1]
[1]*Department of Materials Science and Engineering, Faculty of Engineering and Industrial Technology, Silpakorn University, Nakhon Pathom, Thailand, 73000*
**E-mail: Phonchai_n@su.ac.th*

Abstract:

In this work, we attempt to investigate the effects of cetyltrimethylammonium bromide (CTAB), the cationic surfactant, employed as a grafting agent on the preparation of silver-silica nanocomposites (Ag-SiO_2 NnC). The concentration of the CTAB solution was systematically varied and studied at 2, 4, 8, 16, 32, and 64 mM. The results show a significant increase in the average particle size of Ag-SiO_2 NnC corresponding to the increased CTAB concentrations. The zeta potential value of the nanocomposites was measure to analyze electrostatic interactions between the nanoparticle surface. FT-IR results indicate the surface perturbation during the modification of nanoparticles by CTAB. By coating polymethylmethacrylate with the synthesized Ag-SiO_2 NnC, the surface microhardness of the polymer sheet was reduced. Additionally, an inhibition zone was observed against both Gram-positive and Gram-negative bacteria in antibacterial testing of the coated sample. This contribution may be attributed to fabricating multifunctional nano-scale materials for surface coating applications.

1. Introduction

The irritation caused by infections with multidrug-resistant bacteria is a serious issue for human health[1]. Several technologies have been developed to address this crucial problem, such as the use of bacteriophage particles, clustered regularly interspaced short palindromic repeats, and nano-antibiotic agents created from metallic nanoparticles[2-4]. Among those metals, silver nanoparticles (Ag NPs) were basically collected due to their excellent antibiotic efficiency[5,6]. It is well known that generating reactive oxygen species and silver ions is a significant mechanism by which Ag NPs disrupt the respiratory system of bacterial cells. The metal-citrate salts were primarily used as a capping agent to achieve the highly colloidal stability of Ag NPs, surrounded by a negative surface charge[7,8].

In recent decades, anchoring Ag NPs with silica nanoparticles (SiO_2 NPs) has become an attractive route for developing advanced nanocomposite materials[9-11]. This integration can prevent the aggregation of Ag NPs and decrease the excess release of silver ions, providing multi-functional features to the obtained samples. However, incorporating two nanoparticles with strong interactions, such as forming covalent bonds through surface modification or creating core-shell structures, might decrease the antibiotic efficiency of the nanocomposite materials.

Based on the same surface charge of Ag NPs and SiO_2 NPs (negatively charged), this work aims to synthesize the nanocomposite material contaning both Ag and SiO_2 nanoparticles using a surface grafting agent to create coupling interactions. Aiganyum Abduraimova and co-workers reported that the residual cetyltri-methylammonium bromide (CTAB), a cationic surfactant, on the surface of mesoporous silica helps cap the formed Ag NPs[12]. We believe that the positive charge of CTAB may play a critical role in the coupling mechanism. Thus, the effect of utilizing CTAB as a grafting agent on the synthesis of silver-silica nanocomposite (Ag-SiO_2 NnC) is an attractive approach for developing this class of material.

To advance the synthesized material for use in medical tools or sterilized surface applications, the microhardness values, as well as the bacterial inhibition zone of polymethyl-methacrylate (PMMA) surfaces coated with Ag-SiO_2 NnC, were evaluated and compared. We expect that this coating technology may provide significant data for developing a novel nano-composite innovation.

2. Materials and Methods

2.1 Materials

Silver nitrate was purchased from Sigma-Aldrich. L-ascorbic acid, Trisodium citrate, Sodium hydroxide, and Cetyltrimethyl-ammonium bromide (CTAB) were obtained from KEMAUS, Australia. Sulphuric acid and acetone were used as solvents supplied by RCL Labscan Thailand. Rice mill (Kasettum, Nakhonpathom, Thailand)

provided the rice husk. PMMA pellet was collected from Liack Seng Trading Co., Ltd., Thailand. Deionized water was used throughout the experimental process.

2.2 Synthesis

In this study, SiO_2 NPs were synthesized from rice husk ash (RHA) using the sol-gel method reported in a previous work[13]. The surfaces of the nanoparticles were modified with CTAB at concentrations of 2, 4, 8, 16, 32, and 64 mM, respectively. Ag NPs were synthesized via a chemical reduction of silver ions using ascorbic acid and trisodium citrate dihydrate as reducing and capping agents, respectively. Ag-SiO_2 NnC was then prepared by combining Ag NPs with surface-modified SiO_2 NPs in a 1:1 ratio. The PMMA sheets were prepared using the solvent casting method. The surface coating was successfully applied by drop-casting 2 mL of an aqueous nanocomposite solution onto the PMMA surface. The resulting samples were tested for microhardness and antibacterial activity against both Gram-positive and Gram-negative bacteria.

2.3 Characterization

The morphology of all colloidal solutions was explored by Field Emission Scanning Electron Microscopy (FE-SEM) using a TESCAN MIRA3 electron microscope. Dried samples were prepared by drop casting onto a glass slide. The average particle size and Zeta potential value were determined by dynamic light scattering (DLS, Brookhaven, ZetaPaLs). The interaction and surface functional group were studied by using the Infrared (IR) spectra collected from a Nicolet 6700 FT-IR spectrometer. The color photographs representing the Tyndall effect were taken with a digital camera, without adjusting the brightness or white balance.

3. Results

3.1 Zetapotential and average particle size

The zeta potential values, reflecting surface charge, of Ag-SiO_2 NnC measured by the DLS are presented in Figure 1a. The colloidal solution of a mixture of Ag NPs and SiO_2 NPs, without the addition of CTAB, exhibits an average zeta potential value of -31 mV. This negative value indicates the presence of an anion coating on the nanoparticle surface, which could occur due to the citrate anion on the surface of Ag NPs and the silanol group on the surface of SiO_2 NPs, respectively[14,15]. The inset photograph (Fig. 1a) showed Tyndall effects, a red beamline of scattered light through the nanoparticle dispersion. The average particle size of this mixture was determined to be 98.62 nm (Figure 1b). Adding CTAB into the mixture of Ag NPs and SiO_2 NPs at 10% by volume reveals the significant trend. We observe that the zeta potential value is abruptly increased from -31 to 0.7 mV after adding 2 mM of CTAB into a nanocomposite. Thus, CTAP addition promoted a milky-like precipitated phase formation (inset photograph in Figure 1a). The average particle size, as measured by the DLS technique, is presented in Figure 1b at ~ 500 nm in this system. Increasing the CTAB concentration to 4, 8, 16, and 32 mM results in zeta potential values of 4.2, 6.1, 9.3, and 9.7 mV, respectively. Furthermore, we observed a systematic increase in the average particle size with increasing concentration of CTAB, leading to particle agglomeration.

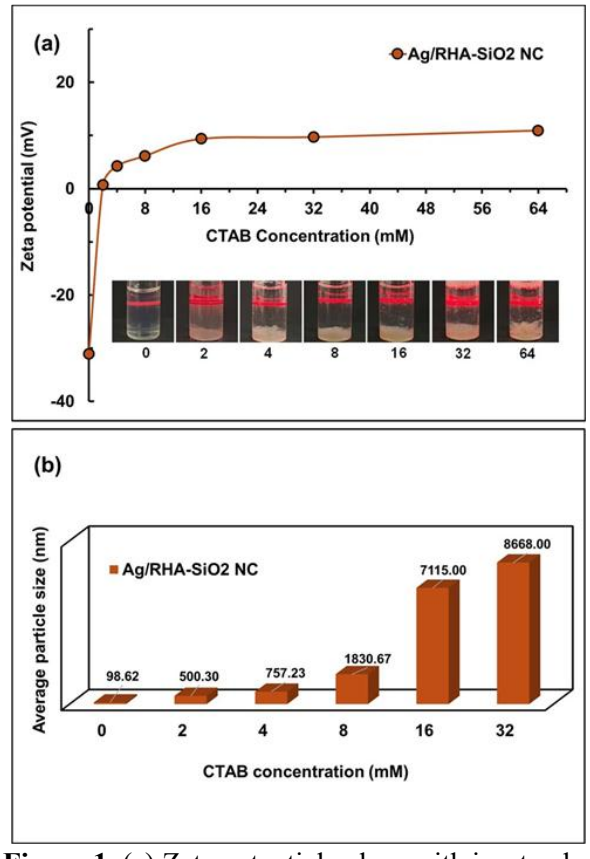

Figure 1. (a) Zeta potential values with inset color photographs showing the Tyndall effect, (b) average particle size plotted by varying CTAB concentration

3.2 Interfacial interaction

The FT-IR spectra of Ag NPs with a citrate capping agent, a mixture of Ag NPs and SiO_2 NPs, and the nanocomposite prepared from 32 mM CTAB were investigated and compared in Figure 2. The characteristic peaks of the citrate group at approximately 3200, 1750, and 1400 cm^{-1}, correspond to the vibrational frequencies of asymmetric -OH stretching, asymmetric C=O stretching, and symmetric C-O stretching, respectively[16]. In Figure 2a, broad peaks corresponding to -OH and C=O signals are possibly due to the presence of hydrogen bonding between citrate-capping agent and Ag NP surface. The spectrum of the mixture between Ag NPs and SiO_2 NPs, including the FT-IR spectrum of the nanocomposite (see Figure 2b and 2c), exhibits a sharper peak at the -OH vibrational frequency, and the narrower peak at around 1600 cm^{-1}, attributed to the carbonyl group. This narrower signal could be attributed to the minimized vibration mode of the hydroxyl and carbonyl moieties surrounding on the Ag NPs surface when SiO_2 NPs were added. The citrate group may be stabilized by the hydroxyl group on the SiO_2 NPs surface. The incorporation of Ag NPs with SiO_2 NPs by using CTAB as a grafting agent displays a few changes in vibration patterns. We observed a peak shift from 1091 to 1078 cm^{-1}, corresponding to a change in the vibrational pattern of the silica siloxane (Si-O-Si). Several factors, such as structure changes[17] and incorporation of ions[18], can cause this transition. Thus, using CTAB as a grafting agent could disturb the siloxane structure on the surface of SiO_2 NPs. However, further experiments are required for further understanding.

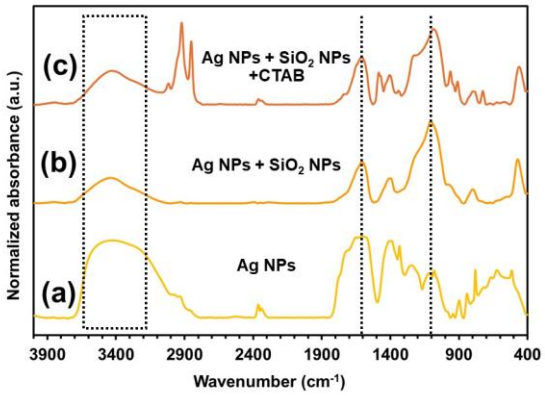

Figure 2. FT-IR spectra of (a) Ag NPs, (b) a mixture of Ag NPs and SiO_2 NPs without CTAB addition, and (c) the nanocomposite prepared from adding 32 mM CTAB.

As results, we propose a grafting mechanism utilizing CTAB as a grafting agent, as presented in Figures 3a and b. The negative charges of Ag NPs and SiO_2 NPs are stabilized by CTAB micelles via electrostatic forces, leading to an increase in zeta potential value and average particle size, as well as the precipitation of the Ag-SiO_2 NnC.

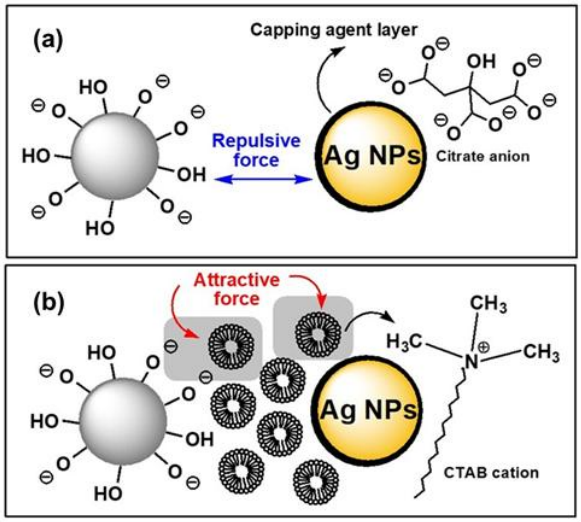

Figure 3. Schematic representation of (a) without adding CTAB and (b) adding CTAB as a grafting agent of Ag-SiO_2 NnC.

3.3 Coating on the PMMA surface

Coating the Ag-SiO_2 NnC on the PMMA surface was studied, and the color photographs of the coated samples, including the SEM images, are displayed in Figure 4a-c. The PMMA film coated by drop-casting SiO_2 NPs exhibits agglomeration of the nanoparticles in the middle of the sample surface, due to the contrast in polarity. The SEM image of this system shows a non-contractile pattern. The PMMA surface coated with SiO_2 NPs using a 32 mM CTAB solution exhibits a more uniform dispersion pattern. This behavior could confirm the increase in hydrophilicity of SiO_2 NPs; however, the residual CTAB solution was observed after the drying process. The Ag-SiO_2 NnC was successfully coated on the PMMA surface. The yellow-colored film, which occurred from the presence of Ag NPs, exhibits good dispersion activity. The SEM image (Figure 4c) shows the uniform dispersion of Ag NPs around the material surface.

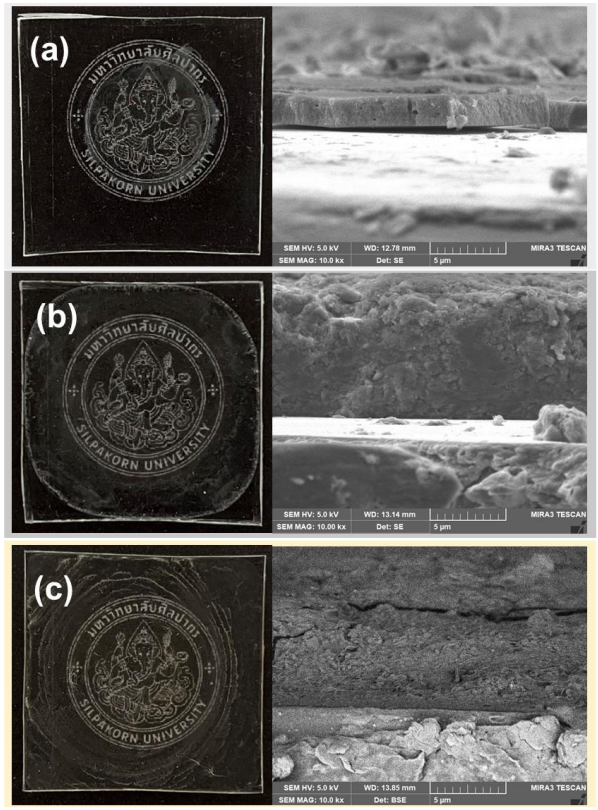

Figure 4. The color photographs (left) and SEM images (right) of PMMA sheets coated by (a) SiO_2 NPs, (b) SiO_2 NPs + CTAB 32 mM, and (c) Ag-SiO_2 NnC prepared from CTAB 32 mM.

3.4 Microhardness and antibacterial testing

The microhardness of the PMMA surface was evaluated using the micro Vickers hardness testing method. The results are presented and compared in Figure 5a. Coating the surface with silica nanoparticles increases the film's hardness compared to the control, due to the formation of an inorganic film on the PMMA surface. On the other hand, PMMA films coated with SiO_2 NPs and Ag-SiO_2 NnC modified with a 32 mM CTAB concentration show a decreasing surface hardness. This reduction is attributed to the improved adhesion and dispersion of the SiO_2 NPs, facilitated by the surfactant effect of CTAB. When hardness is measured, the deep cracks appear, causing a drop in hardness values. The antibiotic activity of the PMMA surface-coated samples was tested against both Gram-positive and Gram-negative microorganisms; the results are presented in Figures 5b and 5c, respectively. The inhibition zone was clearly detected in *S. aureus* for the Ag-SiO_2 NnC sheet; however, focusing on *E. coli*, the inhibition zone was not clearly observed. The result may be due to the structure of *E. coli*, which possesses an outer membrane that acts as a barrier, protecting the bacterium from harmful substances[19]. This outcome is likely due to several contributing factors, including the concentration of active substances being too low to prevent bacterial growth, as well as issues with the experimental process.

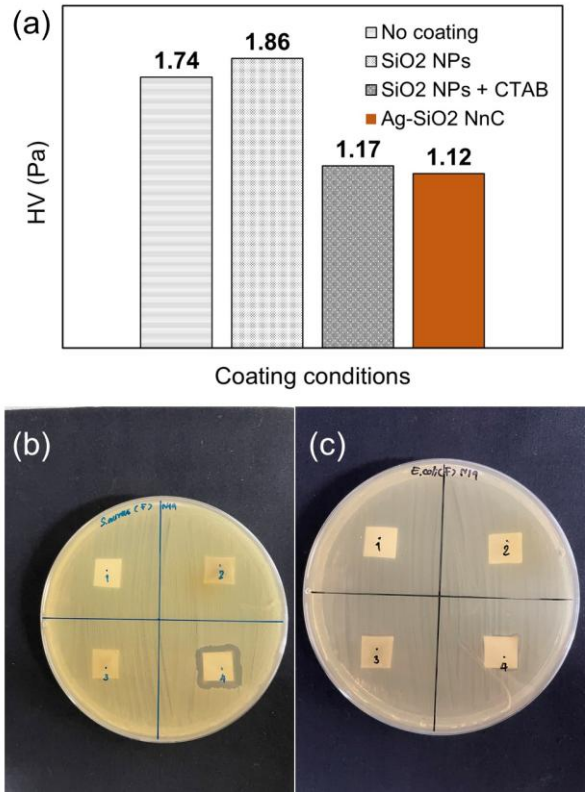

Figure 5. (a) Microhardness values of the coated PMMA surface. The clear zone, representing the antibiotic testing against (b) *S.aureus*, and (c) *E.coli*. Numbers in the petri dish refer to the sample name of the PMMA sheet: (1) No coating, (2) coated with SiO_2 NPs, (3) SiO_2 NPs+CTAB, and (4) Ag-SiO_2 NnC.

Conclusion

This study reports a successful method for fabricating Ag-SiO_2 NnC using CTAB as a grafting agent. The suitable CTAB concentration for producing the nanocomposite and achieving a good dispersion film on the PMMA surface is 32 mM. The electrostatic force obtained from CTAB is a dominant effect for anchoring Ag NPs with SiO_2 NPs. The surface hardness of the PMMA coated with the nanocomposite decreases by about 30% from the uncoated sample. The coated Ag-SiO_2 NnC on the PMMA surface yields a significant result for the inhibition zone, particularly for Gram-positive bacteria.

Acknowledgements

The authors would like to thank the Department of Materials Science and Engineering, Faculty of Engineering and Industrial Technology, Silpakorn University, for financial support.

References

1. Bharadwaj, A.; Rastogi, A.; Pandey, S.; Gupta, S.; Sohal, J. S. Multidrug-Resistant Bacteria: Their Mechanism of Action and Prophylaxis. Biomed Res Int 2022, 2022, 5419874.
2. Li, M.; Liu, Y.; Gong, Y.; Yan, X.; Wang, L.; Zheng, W.; Ai, H.; Zhao, Y. Recent advances in nanoantibiotics against multidrug-resistant bacteria. Nanoscale Advances 2023, 5 (23), 6278-6317.
3. Jamil, B.; Imran, M. Factors pivotal for designing of nanoantimicrobials: an exposition. Critical Reviews in Microbiology 2018, 44 (1), 79-94.
4. Manzar, A.; Muhammad, O.; Atia, A.; Tariq Mahmood, A.; Ruirui, X.; Evan, S.; Xuehai, Y. Tailoring supramolecular short peptide nanomaterials for antibacterial applications. Coordination Chemistry Reviews 2022, 460, 214481.
5. Menichetti, A.; Mavridi-Printezi, A.; Mordini, D.; Montalti, M. Effect of Size, Shape and Surface Functionalization on the Antibacterial Activity of Silver Nanoparticles. Journal of Functional Biomaterials 2023, 14 (5), 244.
6. Tripathi, N.; Goshisht, M. K. Recent Advances and Mechanistic Insights into Antibacterial Activity, Antibiofilm Activity, and Cytotoxicity of Silver Nanoparticles. ACS Applied Bio Materials 2022, 5 (4), 1391-1463.
7. Alula, M. T.; Karamchand, L.; Hendricks, N. R.; Blackburn, J. M. Citrate-capped silver nanoparticles as a probe for sensitive and selective colorimetric and spectrophotometric sensing of creatinine in human urine. Analytica Chimica Acta 2018, 1007, 40-49.
8. UshaVipinachandran, V.; Rajendran, S.; Ali, H.; Ashokan, I.; Bhunia, S. K. Citrate capped silver nanoparticles as an instantaneous colorimetric selective sensor for neomycin and thiamine in wastewater. New Journal of Chemistry 2022, 46 (29), 14081-14090.
9. Karthik, C.; Caroline, D. G.; Dhanam Priya, M.; Pandi Prabha, S. Synthesis, Characterization of Ag-SiO2 Nanocomposite and Its Application in Food Packaging. Journal of Inorganic and Organometallic Polymers and Materials 2021, 31 (6), 2532-2541.
10. Pavoski, G.; Kalikoski, R.; Souza, G.; Brum, L. F. W.; dos Santos, C.; Abo Markeb, A.; dos Santos, J. H. Z.; Font, X.; dell'Erba, I.; Galland, G. B. Synthesis of polyethylene/silica-silver nanocomposites with antibacterial properties by in situ polymerization. European Polymer Journal 2018, 106, 92-101.
11. Assis, M.; Simoes, L. G. P.; Tremiliosi, G. C.; Coelho, D.; Minozzi, D. T.; Santos, R. I.; Vilela, D. C. B.; Santos, J. R. d.; Ribeiro, L. K.; Rosa, I. L. V.; et al. SiO2-Ag Composite as a Highly Virucidal Material: A Roadmap that Rapidly Eliminates SARS-CoV-2. *Nanomaterials* **2021**, *11* (3), 638.
12. Abduraimova, A.; Molkenova, A.; Duisembekova, A.; Mulikova, T.; Kanayeva, D.; Atabaev, T. S. Cetyltrimethylammonium Bromide (CTAB)-Loaded SiO2–Ag Mesoporous Nanocomposite as an Efficient Antibacterial Agent. Nanomaterials 2021, 11 (2), 477.
13. Le, V.H., Thuc, C.N.H. & Thuc, H.H. Synthesis of silica nanoparticles from Vietnamese rice husk by sol–gel method. Nanoscale Res Lett 8, 58 (2013).
14. Alula, M. T.; Karamchand, L.; Hendricks, N. R.; Blackburn, J. M. Citrate-capped silver nanoparticles as a probe for sensitive and selective colorimetric and spectrophotometric sensing of creatinine in human urine. Analytica Chimica Acta 2018, 1007, 40-49.
15. Bekkam, R.; Thiyagarajan, C. Evaluating the effects of rice husk derived nanosilica on growth, photosynthesis, and antioxidant activity in hybrid maize. Environmental Technology & Innovation 2024, 36, 103866.
16. Mondal, P.; Yarger, J. L. Synthesis and Characterization of 1H-Imidazole-4,5-dicarboxylic Acid-Functionalized Silver Nanoparticles: Dual Colorimetric Sensors of Zn^{2+} and Homocysteine. ACS Omega 2022, 7 (37), 33423-33431.
17. Zimnoch Dos Santos, J. H.; Brentano Capeletti, L. Fourier Transform Infrared and Raman Characterization of Silica-Based Materials. In Applications of Molecular Spectroscopy to Current Research in the Chemical and Biological Sciences, Stauffer, M. T. Ed.; IntechOpen, 2016.
18. Ellerbrock, R.; Stein, M.; Schaller, J. Comparing amorphous silica, short-range-ordered silicates and silicic acid species by FTIR. Scientific Reports 2022, 12 (1), 11708.
19. Das, B.; Dash, S. K.; Mandal, D.; Ghosh, T.; Chattopadhyay, S.; Tripathy, S.; Das, S.; Dey, S. K.; Das, D.; Roy, S. Green synthesized silver nanoparticles destroy multidrug resistant bacteria via reactive oxygen species mediated membrane damage. Arabian Journal of Chemistry 2017, 10 (6), 862-876.

DEVELOPMENT OF g-C_3N_4/$CaCO_3$-DERIVED FROM EGGSHELL FOR EFFICIENT PHOTOCATALYTIC WASTEWATER TREATMENT

Khimouorn Plang[1] Jariyaporn Sangkaworn[1], Assadawoot Srikhaow[1], Siwaporn Meejoo Smith[2], Chitiphon Chuaicham[1]*

[1]*Department of Environmental and Sustainable Engineering, Faculty of Engineering, Chulalongkorn University, Bangkok 10330, Thailand*
[2]*Center of Sustainable Energy and Green Materials, and Department of Chemistry, Faculty of Science, Mahidol University, 999 Phuttamonthon Sai 4, Salaya, Nakhon Pathom, 73170, Thailand*
**E-mail: chitiphon.c@chula.ac.th*

Abstract:

Rapid industrialization and dye-intensive manufacturing discharge persistent colorants into waterways, posing health and ecological risks and demanding effective waste treatments. This work develops an eggshell-derived $CaCO_3$/gCN photocatalyst prepared via thermal polymerization of a urea precursors to enhance light-driven photocatalytic Rhodamine B (RhB) removal for elucidating dye degradation performance. XRD results confirmed successful formation of gCN with the strong peak of (002) interlayer at 27.5°, while $CaCO_3$ reflections appear 36.0°, suggesting interfacial interaction between each phase in the composite material. SEM confirmed the porous morphology of the 2.5%$CaCO_3$/gCN composite, while EDS detected C, N, O, and Ca, confirming successful composite formation. Under UVA-light illumination, the 2.5%$CaCO_3$/gCN composite achieved 71.49% RhB removal compared with 40.06% for pristine gCN after 120 mins, indicating faster degradation kinetics and a higher apparent rate constant. Performance advantages are attributed to $CaCO_3$ incorporation, which improving interfacial charge separation and suppressing e^-/h^+ recombination, thereby enhancing photocatalytic activity. By valorizing eggshell waste into a functional photocatalyst component, this study presents a practical, low-cost route to improve gCN performance for dye-laden wastewater treatment.

1. Introduction

Rapid industrialization and population growth now dump 2 million tons of pollutants into water bodies each day, contaminating supplies, degrading ecosystems, and harming human health[1, 2]. Industrial effluents especially from textiles release dye-rich wastewater; textile processes alone discharge 200,000 tons yearly that are toxic and hard to treat [3]. Rhodamine B (RhB) is widely persistent, mutagenic, toxic, and potentially carcinogenic causing health effects even at trace levels so its removal from wastewater is essential [4].

Advance oxidation processes (AOPs) especially light-driven photocatalysis generate reactive oxygen species via photoexcited electron and hole (e^-/h^+) on semiconductors (TiO_2, g-C_3N_4) and, with suitable band gaps and charge separation, cost-effective [5].g-C_3N_4 is a metal-free, graphite-like semiconductor (Eg = 2.7 eV) valued for stability, non-toxicity, and light activity [6]. In RhB treatment, numerous studies report that g-C_3N_4-based photocatalysts can decolorize and degrade RhB under UV/visible irradiation, where the degradation pathway often begins with stepwise N-deethylation, followed by chromophore cleavage and further oxidation toward smaller intermediates and mineralization [6-8]. Practically, g-C_3N_4 is commonly prepared by thermal polycondensation of nitrogen-rich precursors such as urea, melamine, thiourea, and dicyandiamide, and the precursor choice and synthesis route can strongly affect layer stacking, porosity, and surface functional groups, which directly influence on dye adsorption and photocatalytic kinetics [9, 10].

To improve RhB degradation performance, previous research has developed and modified g-C_3N_4 mainly through (i). nanostructure engineering (porous structure frameworks, ultrathin/nanosheet structures via thermal or chemical exfoliation) to increase accessible surface area and shorten charge-transport distances [11, 12], (ii) electronic-structure regulation (heteroatom doping/defect engineering) to enhance light harvesting and suppress e^-/h^+ recombination, for example B-doped g-C_3N_4 reported improved RhB photocatalytic degradation [13], and (iii) constructing heterojunctions with other semiconductors or layered materials to promote directional interfacial charge transfer and reactive oxygen species (ROS) generation (g-C_3N_4/$BiVO_4$ hybrids and LDH/g-C_3N_4 systems) [8, 10-14]. Its photocatalytic efficiency is limited by rapid e^-/h^+

recombination, low light absorption ability and small surface area.

Eggshell waste is an abundant biogenic resource containing approximately 95–98 wt% $CaCO_3$, making it a sustainable and low-cost precursor for $CaCO_3$ preparation. Although $CaCO_3$ is a wide-bandgap material, previous studies have shown that $CaCO_3$ can enhance photocatalytic performance when combined with semiconductors such as TiO_2, NiS, ZnAl MMO, and g-C_3N_4 by improving catalyst dispersion, increasing surface active sites, promoting interfacial charge transfer, and suppressing electron–hole recombination [15-19]. For $CaCO_3$/gCN composites, favorable band alignment between gCN (E_{VB}/E_{CB} = 1.50/–1.17 eV) and $CaCO_3$ (E_{VB}/E_{CB} = 0.99/–4.94 eV) suggests possible hole transfer from gCN to $CaCO_3$, leading to improved charge separation [20]. In addition, $CaCO_3$ introduction during composite formation may induce cyano-related defects or vacancy sites in gCN, which can act as electron-withdrawing or charge-trapping centers to further suppress recombination and enhance reactive oxygen species (ROS) generation [18]. Therefore, eggshell-derived $CaCO_3$/gCN composites offer a sustainable, inexpensive, and effective strategy for photocatalytic wastewater treatment and environmental remediation.

In this work, eggshell-derived $CaCO_3$/gCN composites were synthesized via thermal polymerization of a urea precursor to improve charge separation and photocatalytic activity. The incorporation of $CaCO_3$ may promote cyano-related defects or vacancy sites, thereby suppressing charge recombination. The composites were characterized by XRD and SEM–EDS, and their RhB degradation performance was evaluated under UVA irradiation, demonstrating a low-cost and sustainable strategy for dye wastewater treatment.

2. Materials and Methods

2.1 Materials and eggshell preparation

Urea (CH_4N_2O, ≥99%) was obtained from QReC™. Rhodamine B (RhB) ($C_{28}H_{31}ClN_2O_3$, >95%) were purchased from Tokyo Chemical Industrial (TCI). Eggshells (ES) were collected from a canteen, rinsed thoroughly with deionized water to remove inner membrane, oven-dried at 105 °C overnight, and ground to a fine powder then sieved through a 250 µm mesh. The resulting ES powder was stored in a desiccator.

2.2 Synthesis of $CaCO_3$/g-C_3N_4 composite

$CaCO_3$/g-C_3N_4 ($CaCO_3$/gCN) composites were prepared via thermal polymerization of a urea precursor and eggshell (ES) powder as the $CaCO_3$ source. Briefly, 10 g of urea was mixed with dried and ground ES powder (8, 13, 18, 23, and 28 mg), followed by manual grinding in an agate mortar for 10 min. The mixture was then calcined in air at 550 °C for 2 h with a heating rate of 9.7 °C min^{-1}. After cooling to room temperature, the obtained powders were gently reground to achieve homogeneous composites. The resulting samples were denoted as x%$CaCO_3$/gCN, where x represents the nominal ES-derived $CaCO_3$ loading of 1.5, 2.5, 3.5, 4.5, or 5.5 wt%. For comparison, pristine g-C_3N_4 (gCN) was prepared under the same conditions without ES addition, while calcined eggshell was used as the ES-derived $CaCO_3$ reference.

2.3 Characterization

Crystal structures and phase composition were examined by powder X-ray diffraction (XRD; Bruker D2 PHASER). Diffraction patterns were collected in the 2θ range of 10-80° to confirm the formation of gCN, $CaCO_3$, and their composite, and to check for phase changes after composite preparation. Phase assignment was performed by comparing the measured peaks with standard reference patterns (JCPDS files) and relevant literature. Surface morphology and elemental composition were evaluated using scanning electron microscopy coupled with energy-dispersive X-ray spectroscopy (SEM-EDS; IT700HR). SEM images of synthesized sample were acquired at 5000× magnification using an accelerating voltage of 3 kV (scale bar: 1 µm) to visualize particle morphology and surface texture. EDS mapping/spectra were collected on representative regions to verify the presence and distribution of the expected elements (C, N, O, and Ca), thereby confirming successful composite formation and assessing elemental homogeneity.

2.4 Photocatalytic Measurement

The photocatalytic activity was evaluated using Rhodamine B (RhB) as a model pollutant. Briefly, 50 mg of photocatalyst was dispersed in a RhB solution (10 mg L^{-1}) and magnetically stirred in the dark for 60 min at room temperature to establish adsorption-desorption equilibrium.The

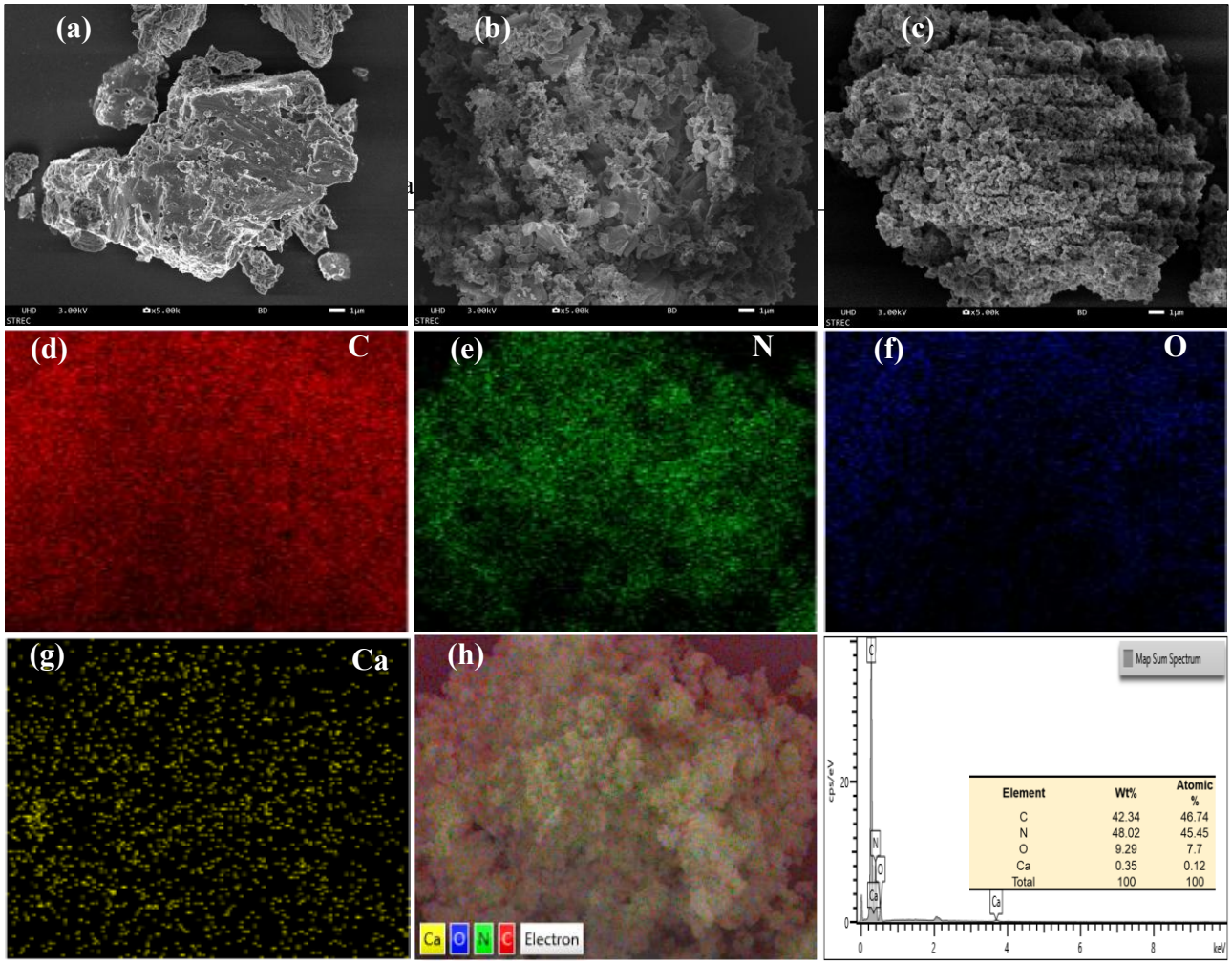

Figure 1. SEM images of (a) $CaCO_3$, (b) gCN, and (c) 2.5%$CaCO_3$/gCN, EDS maps of C, N, O, and Ca for the composite (d-g), (h) overlapping elements in the composite material and EDS spectrum

suspension was then irradiated with 4 UVA lights (Shining black light, 15 W, $\lambda < 395$ nm) to initiate photocatalysis. During the reaction, 1 mL aliquots were withdrawn every 15 min over a total irradiation time of 120 min; each aliquot was immediately filtered through a 0.45 µm membrane filtrate's absorbance at 554 nm (λ_{max} of RhB) was recorded using a UV-vis spectrophotometer (Thermo scientific, Genesys 10S UV-VIS) to determine the concentration of RhB.

3. Results

3.1 Structural characterization

X-ray diffraction patterns (XRD) of pristine gCN, $CaCO_3$, and 2.5%$CaCO_3$/gCN composites are shown in Fig. 2. Pristine gCN shows two characteristic XRD peaks at 13.2° and 27.5° (2θ), indexed to the (100) in- plane structural motif and the (002) interlayer stacking, respectively (JCPDS 87-1526) [21], confirming successful synthesis of gCN by urea derived thermal polymerization.

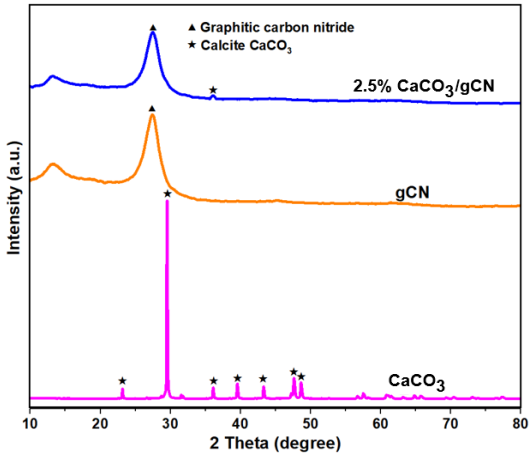

Figure 2. XRD pattern of $CaCO_3$, gCN and 2.5%$CaCO_3$/gCN composite.

Moreover, the $CaCO_3$ sample exhibits reflections characteristic of crystalline calcite $CaCO_3$ (JCPDS 10-0454) with major peaks

typically appearing near 29.4° (104) and 36.0° (110), together with additional weaker reflections at higher angles, confirming the eggshell-derived $CaCO_3$ phase [22]. For the 2.5%$CaCO_3$/gCN composite, the gCN peaks at 13.2° and 27.5° remain present, indicating that the layered carbon nitride framework is preserved after compositing. A weak $CaCO_3$-related peak is observed at 36.10° (2θ), assigned to the calcite (110) plane, verifying the presence of calcite within the composite even at low loading. The fact that other calcite peaks are not clearly detected is reasonable for low $CaCO_3$ content because $CaCO_3$ reflections can fall near the background/tail of the gCN pattern and may be below the XRD detection limit, therefore, the incorporation of $CaCO_3$ is further supported by SEM-EDS results showing Ca in the $CaCO_3$/gCN sample [23].

3.2 Morphology and elemental composition characterization

SEM was used to examine the surface morphology of $CaCO_3$, gCN, and the 2.5%$CaCO_3$/gCN composite (Fig. 2a-c). The $CaCO_3$ sample shows bulk-like particles with a rough and fractured surface (Fig. 2a). For gCN, the fluffy, sheet-like morphology was associated with thermal poly- condensation, during which volatile byproducts are released, depending on the precursor, these gases can include NH_3 and H_2O, which helps generate voids and a porous-looking texture between stacked flakes [24] (Fig. 2b). The stacked, wrinkled sheets also indicate partial restacking of gCN layers after synthesis, producing inter-sheet spaces that can act as diffusion pathways for dye molecules during photocatalysis.

In the 2.5%$CaCO_3$/gCN composite (Fig. 2c), the morphology is clearly different from pristine g-CN, showing a rougher and more porous-looking surface with abundant small voids. This structural modification may increase the accessible surface and provide more exposed active sites, which can be beneficial for photocatalytic degradation [20, 25]. In addition, a roughened surface can improve interfacial contact between $CaCO_3$ and gCN, which is important for facilitating charge transfer across the composite interface during illumination.

EDS mapping of the 2.5%$CaCO_3$/gCN composite (Fig. 2d-h) confirmed the presence of C and N from the gCN matrix together with Ca, verifying successful Ca-containing phase incorporation. O was also detected; however, this signal can originate from both $CaCO_3$ and oxygen-containing surface species in urea-derived gCN, so EDS cannot uniquely assign O to a single component. Overall, the combined SEM morphology change and the detection of Ca alongside the gCN elements support the successful formation of the $CaCO_3$/gCN composite with well-dispersed Ca-containing domains on the gCN surface.

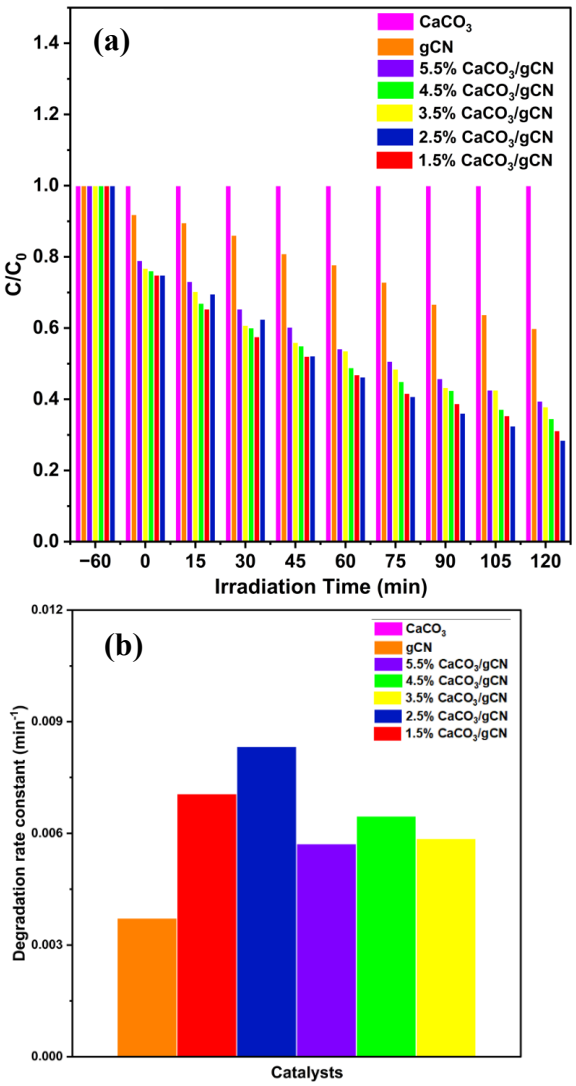

Figure 3. Photocatalytic performance of the as-prepared samples toward RhB: (a) degradation profiles and (b) degradation rate constant (min^{-1}).

3.3 Photocatalytic degradation of RhB

The photocatalytic performance was assessed by RhB degradation under UVA irradiation (Fig. 3a). After 120 min of light illumination, calcite $CaCO_3$ showed no

photocatalytic activity, consistent with the wide band gap of $CaCO_3$ according to previous research [20]. This also indicates that RhB is stable under UVA light. In contrast, gCN exhibited clear photocatalytic activity, achieving a degradation efficiency of 40.06% after 120 min. Notably, $CaCO_3$/gCN composites outperformed pristine gCN under identical conditions, demonstrating that incorporating $CaCO_3$ positively influences the RhB removal process. Among all the composite, 2.5%$CaCO_3$/gCN showed the highest removal efficiency (71.49%), suggesting that a low $CaCO_3$ loading provides the most effective interfacial modification, while maintaining sufficient gCN light absorption and active surface for photocatalysis.

To investigate the reaction kinetics of RhB degradation, time-concentration data were fitted with a pseudo-first-order model, $-\ln(C_0/C) = kt$. From the slope of the linear fit, the apparent rate constant (k) was obtained for each sample. The plots were well described by linear fits ($R^2 > 0.95$; Fig. 3b). Notably, the 2.5%$CaCO_3$/gCN composite exhibited the highest k value of 8.33×10^{-3} min^{-1}, which is 2.24 times that of pristine gCN, confirming that $CaCO_3$ incorporation substantially accelerates the degradation rate. This enhanced kinetic performance is consistent with the improved RhB removal observed in Fig. 3a and suggests more efficient generation and utilization of reactive species and improved charge-carrier management in the composite system.

To elucidate the removal pathway, three control experiments were conducted photolysis, adsorption, and photocatalysis for RhB using the 2.5%$CaCO_3$/gCN sample as shown in Fig. 4. Under photolysis (UVA irradiation without catalyst), the RhB concentration remained essentially unchanged throughout the test, confirming that direct photodegradation of RhB under UVA is negligible and that the dye is stable under the applied light conditions. In the dark adsorption experiment (catalyst present without light), the suspension reached adsorption-desorption equilibrium within 60 min, and a 24.5% decrease in RhB concentration was observed, indicating that the composite has a measurable adsorption capacity for RhB. By contrast, under photocatalysis (catalyst with UVA), the RhB concentration decreased further after the adsorption-desorption equilibrium, demonstrating that the 2.5%$CaCO_3$/gCN composite not only adsorbs RhB but also drives subsequent light-activated oxidative degradation. The additional reduction under illumination confirms that photocatalytic reactions contribute significantly beyond adsorption alone, supporting the role of $CaCO_3$/gCN as an effective UVA-responsive photocatalyst for RhB removal.

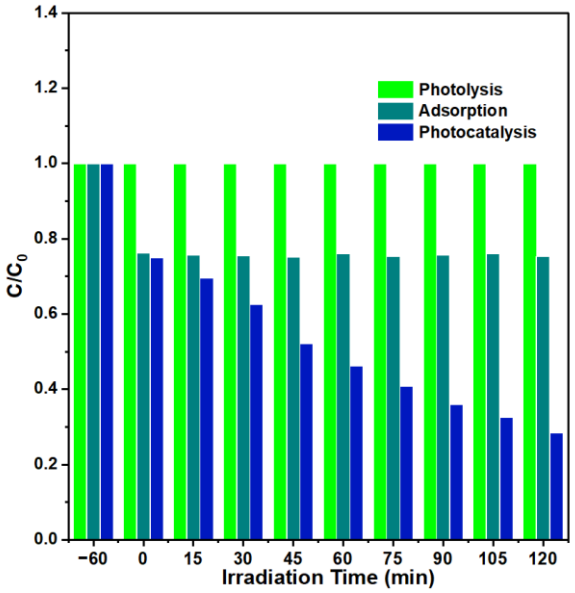

Figure 4. Control experiments for RhB removal:, adsorption in the dark, photolysis and photocatalysis under UVA.

Conclusion

We demonstrated a simple route to synthesize $CaCO_3$/gCN photocatalysts using readily available eggshell-derived $CaCO_3$ and urea. XRD confirmed calcite reflections from $CaCO_3$ within the gCN composite, consistent with interfacial contact between the two phases. Notably, the calcite (110) peak at 36.0° (2θ) was observe in the composite, indicating the successfully confirm the composite material of $CaCO_3$/gCN. SEM revealed that the 2.5%$CaCO_3$/gCN sample developed a rough, porous texture, and EDS confirmed the presence of Ca along with the gCN elements, indicating successful incorporation of $CaCO_3$ into the composite. Under UVA irradiation, the composites outperformed pristine gCN in degrading RhB: the 2.5%$CaCO_3$/gCN sample achieved 71.49% removal after 120 min, compared with 40.06% for pristine gCN. The overall removal involved both dark adsorption and photocatalysis, with the additional decline under illumination confirming light-driven catalysis. We attribute the enhancement to interfacial effects from finely

dispersed $CaCO_3$ that promote charge separation and suppress electron-hole recombination [10]. Overall, this work highlights an inexpensive, waste-valorizing of eggshell derived $CaCO_3$ to boost gCN photocatalysis, with 2.5%$CaCO_3$ identified as an optimal loading.

Acknowledgement

We thank the Department of Environmental and Sustainable Engineering, Faculty of Engineering, Chulalongkorn University, for providing laboratory space and experimental support.

References

1. Nie, C.; Wang, X.; Lu, P.; Zhu, Y.; Li, X.; Tang, H. Advancements in S-scheme heterojunction materials for photocatalytic environmental remediation. *Journal of Materials Science & Technology* **2024**, *169*, 182-198. DOI: https://doi.org/10.1016/j.jmst.2023.06.011.
2. Kumari, H.; Sonia; Suman; Ranga, R.; Chahal, S.; Devi, S.; Sharma, S.; Kumar, S.; Kumar, P.; Kumar, S.; et al. A Review on Photocatalysis Used For Wastewater Treatment: Dye Degradation. *Water Air Soil Pollut* **2023**, *234* (6), 349. DOI: 10.1007/s11270-023-06359-9 From NLM.
3. Khan, S.; Malik, A. Toxicity evaluation of textile effluents and role of native soil bacterium in biodegradation of a textile dye. *Environmental Science and Pollution Research* **2018**, *25* (5), 4446-4458. DOI: 10.1007/s11356-017-0783-7.
4. Gatou, M.-A.; Fiorentis, E.; Lagopati, N.; Pavlatou, E. A. Photodegradation of Rhodamine B and Phenol Using TiO_2/SiO_2 Composite Nanoparticles: A Comparative Study. *Water* **2023**, *15* (15), 2773.
5. Kar, P.; Shukla, K.; Jain, P.; Sathiyan, G.; Gupta, R. K. Semiconductor based photocatalysts for detoxification of emerging pharmaceutical pollutants from aquatic systems: A critical review. *Nano Materials Science* **2021**, *3* (1), 25-46. DOI: https://doi.org/10.1016/j.nanoms.2020.11.001 .
6. Zheng, M.; Guo, M.; Ma, F.; Li, W.; Shao, Y. Recent advances in graphitic carbon nitride-based composites for enhanced photocatalytic degradation of rhodamine B: mechanism, properties and environmental applications. *Nanoscale Advances* **2025**, *7* (16), 4780-4802, 10.1039/D5NA00439J. DOI: 10.1039/D5NA00439J.
7. Haleem, A.; Ullah, M.; Rehman, S. U.; Shah, A.; Farooq, M.; Saeed, T.; Ullah, I.; Li, H. In-Depth Photocatalytic Degradation Mechanism of the Extensively Used Dyes Malachite Green, Methylene Blue, Congo Red, and Rhodamine B via Covalent Organic Framework-Based Photocatalysts. In *Water*, 2024; Vol. 16, p 1588.
8. Rohilla, P.; Pal, B.; Das, R. K. Improved photocatalytic degradation of rhodamine B by g-C3N4 loaded $BiVO_4$ nanocomposites. *Heliyon* **2023**, *9* (11), e21900. DOI: https://doi.org/10.1016/j.heliyon.2023.e21900 .
9. Cao, S.; Low, J.; Yu, J.; Jaroniec, M. Polymeric Photocatalysts Based on Graphitic Carbon Nitride. *Advanced Materials* **2015**, *27* (13), 2150-2176. DOI: https://doi.org/10.1002/adma.201500033.
10. Yang, L.; Liu, X.; Liu, Z.; Wang, C.; Liu, G.; Li, Q.; Feng, X. Enhanced photocatalytic activity of g-C_3N_4 2D nanosheets through thermal exfoliation using dicyandiamide as precursor. *Ceramics International* **2018**, *44* (17), 20613-20619. DOI: https://doi.org/10.1016/j.ceramint.2018.06.105.
11. Yuan, X.; Zhou, C.; Jin, Y.; Jing, Q.; Yang, Y.; Shen, X.; Tang, Q.; Mu, Y.; Du, A. K. Facile synthesis of 3D porous thermally exfoliated g-C_3N_4 nanosheet with enhanced photocatalytic degradation of organic dye. *J Colloid Interface Sci* **2016**, *468*, 211-219. DOI: 10.1016/j.jcis.2016.01.048 From NLM.
12. Pei, J.; Li, H.; Zhuang, S.; Zhang, D.; Yu, D. Recent Advances in g-C_3N_4 Photocatalysts: A Review of Reaction Parameters, Structure Design and Exfoliation Methods. In *Catalysts*, 2023; Vol. 13, p 1402.
13. Yan, S. C.; Li, Z. S.; Zou, Z. G. Photodegradation of Rhodamine B and Methyl Orange over Boron-Doped g-C_3N_4 under Visible Light Irradiation. *Langmuir* **2010**, *26* (6), 3894-3901. DOI: 10.1021/la904023j.
14. Du, C.; Xu, J.; Ding, G.; He, D.; Zhang, H.; Qiu, W.; Li, C.; Liao, G. Recent Advances in LDH/g-C_3N_4 Heterojunction Photocatalysts for Organic Pollutant Removal. *Nanomaterials (Basel)* **2023**, *13* (23). DOI: 10.3390/nano13233066 From NLM.
15. Kuppusamy, M.; Kim, S.-W.; Lee, K.-P.; Jo, Y. J.; Kim, W.-J. Development of TiO_2–

$CaCO_3$ Based Composites as an Affordable Building Material for the Photocatalytic Abatement of Hazardous NO_x from the Environment. *Nanomaterials* **2024**, *14* (2), 136.

16. Huang, C.; Xu, F.; Hu, C.; Wang, X.; Wang, D.; Zhong, Y.; Tang, C. Construction of heterostructured $CaCO_3$/NiS with enhanced photocatalytic antibacterial performance under visible light. *Journal of Photochemistry and Photobiology A: Chemistry* **2024**, *447*, 115187. DOI: https://doi.org/10.1016/j.jphotochem.2023.115187.
17. Tajat, N.; El Hayaoui, W.; El Mouhri, W.; Nadif, I.; Bougdour, N.; Idlahcen, A.; Bakas, I.; Badreddine, M.; Tamimi, M.; Assabbane, A.; Qourzal, S. Synthesis of eco-friendly $CaCO_3$@Zn-Al MMO core-shell nanoflowers photocatalyst using bio–eggshell waste for improved photocatalytic degradation of RhB under visible light irradiation. *Environmental Research* **2024**, *263*, 120218. DOI: https://doi.org/10.1016/j.envres.2024.120218.
18. Qi, C.; Chen, H.; Chen, X.; Chu, C.; Mei, X.; Lu, W.; Li, N. In-situ-reduced synthesis of cyano group modified g-C_3N_4/$CaCO_3$ composite with highly enhanced photocatalytic activity for nicotine elimination. *Journal of Environmental Sciences* **2023**, *126*, 517-530. DOI: https://doi.org/10.1016/j.jes.2022.03.019.
19. Wang, J.; Sun, S.; Pan, L.; Xu, Z.; Ding, H.; Li, W. Preparation and Properties of $CaCO_3$-Supported Nano-TiO_2 Composite with Improved Photocatalytic Performance. *Materials* **2019**, *12* (20), 3369.
20. Lu, P.; Hu, X.; Li, Y.; Peng, Y.; Zhang, M.; Jiang, X.; He, Y.; Fu, M.; Dong, F.; Zhang, Z. Novel $CaCO_3$/g-C_3N_4 composites with enhanced charge separation and photocatalytic activity. *Journal of Saudi Chemical Society* **2019**, *23* (8), 1109-1118. DOI: https://doi.org/10.1016/j.jscs.2019.07.002.
21. Tian, Y.; Ge, L.; Wang, K.; Chai, Y. Synthesis of novel MoS_2/g-C_3N_4 heterojunction photocatalysts with enhanced hydrogen evolution activity. *Materials Characterization* **2014**, *87*, 70-73. DOI: https://doi.org/10.1016/j.matchar.2013.10.020.
22. Li, K.; Zhou, W.; Li, X.; Li, Q.; Carabineiro, S. A. C.; Zhang, S.; Fan, J.; Lv, K. Synergistic effect of cyano defects and $CaCO_3$ in graphitic carbon nitride nanosheets for efficient visible-light-driven photocatalytic NO removal. *Journal of Hazardous Materials* **2023**, *442*, 130040. DOI: https://doi.org/10.1016/j.jhazmat.2022.130040.
23. Palanisamy, K.; Sanjiv Raj, K.; Bhuvaneswari, S.; Rajasekaran, M.; Subramanian, V. K. The effect of DTPA on calcium carbonate scale deposition on copper and aluminium surfaces. *Heliyon* **2020**, *6* (3), e03506. DOI: https://doi.org/10.1016/j.heliyon.2020.e03506.
24. Shenoy, S.; Chuaicham, C.; Okumura, T.; Sekar, K.; Sasaki, K. Simple tactic polycondensation synthesis of Z-scheme quasi-polymeric g-C_3N_4/$CaFe_2O_4$ composite for enhanced photocatalytic water depollution via p-n heterojunction. *Chemical Engineering Journal* **2023**, *453*, 139758. DOI: https://doi.org/10.1016/j.cej.2022.139758.
25. Dong, J.; Zhang, Y.; Hussain, M. I.; Zhou, W.; Chen, Y.; Wang, L.-N. g-C_3N_4: Properties, Pore Modifications, and Photocatalytic Applications. In *Nanomaterials*, 2022; Vol. 12, p 121.

NANO
THAILAND 2025

Organized by Nanotechnology Association of Thailand with National Nanotechnology Center (NANOTEC) & Research Network of Nanotechnology (RNN)

Nanothailand2025@gmail.com